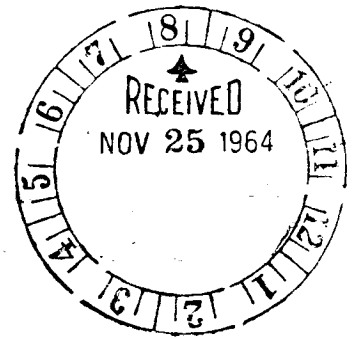PHASE II

ANALYSIS OF THERMAL ENVIRONMENT

PROBLEMS AND THE CREATION OF

ANALYTICAL TOOLS FOR SELECTED

SITUATIONS ON SATURN VEHICLES

HEAT
TECHNOLOGY
LABORATORY
INC.

HTL-TR-20, PHASE II

4308 Governors Drive – Huntsville, Alabama – 35805

October 15, 1964

PHASE II

ANALYSIS OF THERMAL ENVIRONMENT

PROBLEMS AND THE CREATION OF

ANALYTICAL TOOLS FOR SELECTED

SITUATIONS ON SATURN VEHICLES

Final Report

HTL-TR-20, PHASE II

October 15, 1964

for

National Aeronautics and Space Administration

George C. Marshall Space Flight Center

Huntsville, Alabama

The final report describing work performed under Contract

11558, Phase II, Control Number CPB 16-13-64.

Heat Technology Laboratory, Inc.

Huntsville, Alabama

TABLE OF CONTENTS

SUMMARY

15143

Work performed under Phase II consisted of aerothermo-
dynamic and instrumentation studies. The aerothermodynamic
work included the creation of analytical tools for semi-
classical problems, solutions to particular heat transfer
problems in the SATURN Program, and development of ideas
and techniques for experimentally investigating aerothermo-
dynamic phenomena. The instrumentation work consisted of
the analysis of heat flux transducers flown on SATURN
vehicles and a literature survey of instrumentation for
fluid flow studies.

Author

2.1 STUDY OF FREE MOLECULE FLOW THROUGH CIRCULAR DUCTS

2.1.1 Summary

A theoretical investigation was made of free-molecule flow through a duct of circular cross section. The molecular flux to the duct wall and exit plane was calculated along with the total flow rate through the duct. The density field was calculated at the duct exit and along the center-line for various duct wall temperature and thermal accommodation coefficients. It was concluded that an experimental determination of the thermal accommodation coefficient can be made by measuring the effect of the duct wall temperature on the density field.

2.1.2 Nomenclature

$(F_{IW})_{x/L}$	Form factor for flux from duct entrance to a point on wall at a dimensionless distance x/L from entrance.
$(F_{WW})_{\|(x/L)-(\ell/L)\|}\delta\ell$	Form factor for flux from a ring element $\delta\ell$ wide of duct wall to a point on the wall at a dimensionless distance $\|(x/L)-(\ell/L)\|$.
$(F_{IE})_{r/R}$	Form factor for flux from entrance to a point r/R on exit.
$(F_{WE})_{x/L,r/R}\ \delta\ell$	Form factor for flux from a ring element $\delta\ell$ wide of duct wall a dimensionless distance x/L from entrance to a point r/R on exit.
L	Duct Length.
M	Molecular Weight.

Symbol	Definition
n	Number of collisions.
q_o	Molecular flux from reservoir to entrance plane.
$(q_E/q_o)_{r/R,n}$	Dimensionless molecular flux to exit plane at r/R for molecules reaching exit after n collisons.
$(q_E/q_o)_{r/R}$	Total Dimensionless molecular flux to exit plane at r/R.
$(q_W/q_o)_{x/L,n}$	Dimensionless molecular flux to duct wall at x/L for molecules reaching point on wall after n collisions.
$(q_W/q_o)_{x/L}$	Total dimensionless molecular flux to duct wall at x/L.
Q_E	Total flow rate.
r	Radial Distance.
R	Duct radius.
$\mathcal{R}$	Universal gas constant.
T_o	Reservoir gas temperature.
T_s	Duct wall temperature.
T_n	Gas temperature after n collisions.
$\bar{v}$	Mean molecular velocity.
$\bar{v}_o$	Reservoir mean molecular velocity.
x	Axial distance from duct entrance.
α	Thermal accommodation coefficient.
ρ_o	Reservoir number volume density of gas molecules.
$(\rho/\rho_o)_{r/R,n}$	Dimensionless number volume density at r/R on exit for molecules reaching exit after n collisions.
$(\rho/\rho_o)_{r/R}$	Total dimensionless number volume density at r/R on exit.

$(\rho/\rho_o)_{x/L,n}$ — Dimensionless number volume density at x/L on center line for molecules reaching exit after n collisions.

$(\rho/\rho_o)_{x/L}$ — Total dimensionless number volume density at x/L on center line.

2.1.3 Introduction

Recent requirements for space environment simulation facilities have resulted in increased effort toward understanding and predicting the behavior of low density gas flow. Many of these studies have been directed toward the prediction of flow rates through complicated duct systems, the development of cryopanel shapes for optimum pumping speeds in high vacuum systems, and the prediction of the properties of the flow field surrounding bodies in high velocity flight in the upper atmosphere.

Free-molecule flow rates through tubes were first investigated theoretically and experimentally by Knudsen (Ref. 2.1-1). These studies were made for flow in long capillary tubes (the tube length being much longer than its radius) for which end effects may be neglected. Clausing (Ref. 2.1-2) later extended the flow rate theory to the case of short tubes and ducts. The same mathematical problem was solved independently and almost simultaneously by Hottel and Keller (Ref. 2.1-3) for the case of thermal radiation through furnace openings. Hottel and Keller's results are nearly identical with Clausing's. The accuracy of Clausing's solution was verified nearly 20 years later

by Demarcus and Hopper (Ref. 2.1-4).

Other investigators (Ref. 2.1-5,-6,-7,-8,-9,-10,-11) have studied molecular flux and flow rates for various conditions of free-molecule flow.

The calculation of density fields for free-molecule flow was made by Bird (Ref. 2.1-12) for the field about moving bodies of various geometries, Touryan (Ref. 2.1-12) for the flow over a circular plate, and Howard (Ref. 2.1-14) and Gustafson and Kiel (Ref. 2.1-15) for flow through orifices.

Sparrow and Hji-Sheikh (Ref. 2.1-16) investigated, among other parameters, the density field through circular ducts for the case of perfect thermal accommodation of the molecules at the duct wall (a thermal accomodation coefficient of the duct wall material of unity).

The purpose of this study is to determine theoretically the flow rate and density field through a circular duct at various duct wall temperatures and thermal accommodation coefficients.

2.1.4 Analysis and Discussion of Results

Consider the following illustrated circular duct:
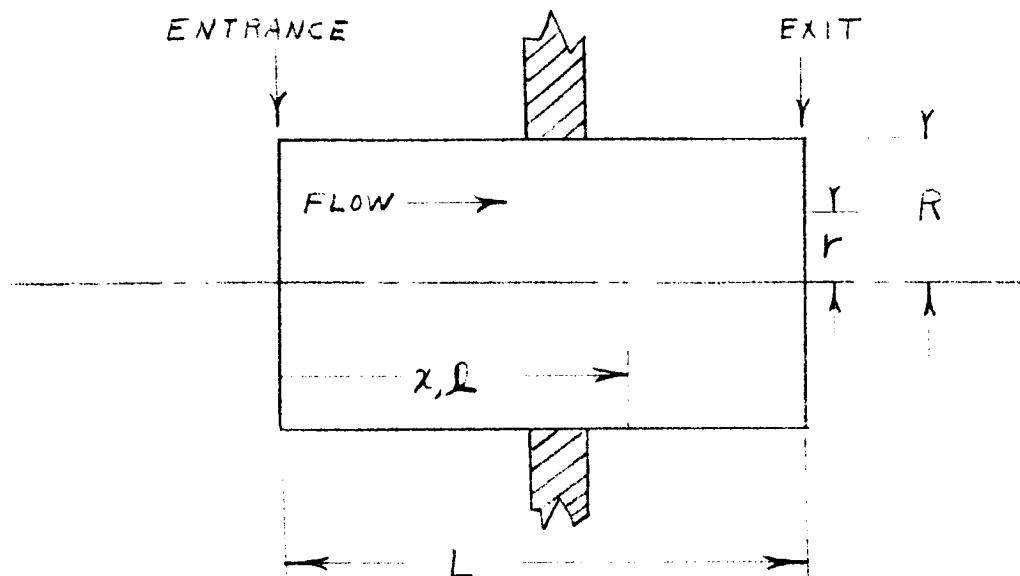
The entrance is exposed to an infinitely large reservoir of rarefied Maxwellian gases at density, ρ_o, and temperature, T_o, while the exit is exposed to a vacuum. The dimensions of the duct are small in comparison to the mean free path of the gas molecules so that the flow of molecules in the duct may be considered "free-molecular"; i.e., intermolecular collisions may be neglected in comparison to the collisions of molecules with the duct wall. Diffuse (cosine law) scattering of the molecules by the wall will be assumed (experiments by Knudsen (Ref 2.1-17) and others on the reflection of molecular beams from glass and polished metal surfaces indicate nearly 100 percent diffuse reflection). Moreover, it is assumed that the system is in equilibrium and that all molecules incident on a surface are reflected without adsorption, outgassing, or surface reactions.

The molecular flux for molecules leaving the re-

servoir at the duct entrance is (Ref. 2.1-21):

$$z_o = \rho_o \left(Q T_o / 2 \pi M \right)^{1/2}. \qquad (2.1-1)$$

Some of these molecules pass through the duct without any collisions. Those molecules that collide with the wall may, after one or more collisions, finally leave the duct through the exit or be scattered back into the reservoir.

With each collision, the molecule will gain or lose some of its energy, the amount of gain or loss depending on the duct wall temperature and the thermal accommodation coefficient. Although this gain or loss of energy does not influence the probability of eventual passage through the duct (and, hence, the equilibrium flow rate), it does influence the density field.

It has been shown (Ref. 2.1-1,-2,-3) that it is not necessary to consider each collision in computing molecular flux and flow rates. Since each collision affects the density field, however, the present author found it convenient to calculate the contribution to the molecular flux of each collision with its resulting contribution to the density field.

Molecular Flux and Flow Rates

There are two distinct methods now in use for computing molecular flux and flow rates under highly rarefied

conditions. The first method, known as the Monte Carlo technique, is particularly well suited to complicated geometrical shapes. This method traces many individual particles through randomly chosen paths. A sufficient number of these random paths is traced to statistically determine the most probable distribution of particles over the geometrical shape. This method was used by Ballance, Roberts, and Tarbell (Ref. 2.1-18) to study molecular fluxes for various cryoarray configurations in a high vacuum cryopumping system. It was also used by Davis (Ref. 2.1-19), to calculate the flow rate through ducts of various shapes.

The second method, designated the "molecular kinetics" method by Link (Ref. 21.-20), is based on the analogy between radiant energy transfer and free-molecule kinetics (Ref.2.1-20,-21). The procedure utilized in this method is to subdivide the geometry into discrete elements for which a radiation "form factor" may be calculated. This method, particularly useful for simple geometries for which published values of form factors exist, will be utilized in the present study.

Molecular Flux to Duct Wall

Based on radiation analogy principles, the molecular flux to the wall of the previously illustrated duct due to a collisionless passage from the reservoir is:

$$\left(q_w/q_c\right)_{x/L,c} = \left(F_{IW}\right)_{x/L} \qquad (2.1\text{-}2)$$

where (Ref. 2.1-22):

$$\left(F_{IW}\right)_{x/L} = (1/2)\left[\frac{(L/R)^2(x/L)^2 + 2}{\left[(L/R)^2(x/L)^2 + 4\right]^{1/2}} - (L/R)(x/L)\right]. \quad (2.1\text{-}3)$$

The molecular flux on the duct wall for molecules reaching the wall after n collisions is:

$$\left(q/q_o\right)_{x/L, n} = \int_0^1 \left(F_{WW}\right)_{|(x/L) - (\lambda/L)|} \left(q_W/q_o\right)_{\lambda/L, n-1} d(\lambda/L) \quad (2.1\text{-}4)$$

where (Ref. 2.1-3):

$$\left(F_{WW}\right)_{|(x/L) - (\lambda/L)|} = (1/2)(L/R)\left[1 - (L/R)|(x/L) - (x/L)|\right.$$

$$\left.\frac{(L/R)^2\left[(x/L) - (\lambda/L)\right]^2 + 6}{\left[(L/R)^2\left[(x/L) - (\lambda/L)\right]^2 + 4\right]^{3/2}}\right]. \quad (2.1\text{-}5)$$

The total molecular flux on the duct wall is obtained by summing the fluxes for each collision as follows:

$$\left(q_W/q_o\right)_{x/L} = \sum_{n=0}^{\infty} \left(q_W/q_o\right)_{x/L, n} \quad (2.1\text{-}6)$$

The total molecular flux at the duct wall surface was calculated from equation (2.1-2), (-4), and (-6) for a duct of dimensions, L/R = 2.0. Equation (2.1-4) was integrated numerically by the procedure described in Appendix 2.1-A. The summation in equation (2.1-6) was carried out

to 20 collisions. The results are presented in (Fig. 2.1-1) along with the contributions of the first few collisions. It is seen that the contributions rapidly become insignificant after a few collisions. It is also noted that the total flux distribution is remarkably linear. Hottle (Ref. 2.1-3) made the same observation in his radiation analysis and suggested that a simple solution of the problem could be made by assuming a linear total wall flux distribution and then solving for the exit flux.

Molecular Flux at Exit Plane

The exit molecular flux at radial position r/R for a collisionless passage from the reservoir through the duct is:

$$\left(q_E / q_o \right)_{r/R, c} = \left(F_{IE} \right)_{r/R} \qquad (2.1-7)$$

where (Ref. 2.1-22):

$$\left(F_{IE} \right)_{r/R} = (1/2) \left[1 - \frac{(L/R)^2 + (r/R)^2 - 1}{\left[\left[(L/R)^2 + (r/R)^2 + 1 \right]^2 - 4 (r/R)^2 \right]^{1/2}} \right] \qquad (2.1-8)$$

The molecular flux for molecules reaching the exit after n collisions is:

$$\left(q_E / q_o \right)_{r/R, n} = \int_0^1 \left(F_{NE} \right)_{x/L, r/R} \left(q_w / q_o \right)_{x/L, n-1} d(x/L) \qquad (2.1-9)$$

where:

$$\left(\overline{F_{NE}}\right)_{x/L,\,n}$$

$$= 2(L/R)^2(1 - x/L)\frac{(L/R)^2(1-x/L)^2 - (\nu/R)^2 + 1}{\left\{\left[(L/R)^2(1-x/L)^2 + (\nu/R)^2 + 1\right]^2 - 4(\nu/R)^2\right\}^{3/2}} \quad (2.1\text{-}10)$$

Equation (2.1-10) is derived in Appendix 2.1-B.

As in the case of the flux to the duct wall, the total flux to a point on the exit is obtained by summing the contributions for each collision:

$$\left(q_E/q_o\right)_{x/R} = \sum_{n=0}^{\infty} \left(q_E/q_o\right)_{x/R,\,n} \quad (2.1\text{-}11)$$

The contribution to the center exit flux for each collision is presented in Fig. 2.1-2 as a function of collision number for a duct with dimensions, L/R = 2.0. (Again, the equations were integrated numerically by the procedure of Appendix 2.1-A and the summation was carried to 20 collisions). As shown previously for the wall flux, the contribution rapidly becomes insignificant with increasing collision number.

The total flux distribution over the exit is shown in Fig. 2.1-3 along with the contributions of the first few collisions. An interesting characteristic of the distribution curves is their "boundary-layer" like decrease in magnitude at the edge of the duct. This curvature is displayed by all contributions involving one or more collisions.

Total Flow Rate

The total flow rate through the duct is obtained by integrating the total molecular flux distribution over the exit:

$$Q_E/q_0 = (q_E/q_0)_{r/R} \, dA = 2\pi R^2 \int_0^1 (q_E/q_0)_{r/R} (r/R) \, d(r/R) \cdot \quad (2.1\text{-}12)$$

The flow rate through ducts of several L/R ratios was calculated numerically from equation (2.1-12) by the procedure of Appendix 2.1-C and is presented in Fig. 2.1-4 compared with Clausing's (Ref. 2.1-2) calculations. For an L/R ratio of 2.0 a difference of 0.1 percent is noted for the present calculations when compared with Clausing's .

Density Fields

The number volume density ρ of molecules at a point due to the flux from an element of area dA at a distance d from the point is determined by (Ref. 2.1-1) :

$$d\rho = q \cos\theta \, dA / \bar{v} \, \pi d^2 = (q/\bar{v})(d\omega/\pi) \quad (2.1\text{-}13)$$

where $d\omega = \cos\theta dA/d^2$, q is the flux from the surface element dA, θ is the angle between the normal to dA and the line d, and $\bar{v}$ is the mean velocity of the molecules.

The reservoir flux (the flux from the reservoir to the duct entrance) q_0, can be expressed in terms of the far upstream reservoir density and mean molecular velocity as

follows (Ref. 2.1-21):

$$q_o = (1/4) \rho_c \, \overline{V}_o \, .$$

$$(2.1-14)$$

Combining equations (2.1-13) and (-14) yields:

$$d\rho/\rho_c = (1/4)[(q/q_o)/(\overline{V}/\overline{V}_o)](d\omega/\pi) \, .$$

$$(2.1-15)$$

For the density due to the flux directly from the reservoir, the flux and mean velocity ratios become unity and the density is found from:

$$(\rho/\rho_c)_{\sim/R,c} = (1/4) \int d\omega/\pi \, .$$

$$(2.1-16)$$

where the integration is over the solid angle enclosed by the duct entrance.

Density at Exit Plane

The center exit density due to a collisionless passage from the reservoir is found from equation (2.1-16) to be (Appendix 2.1-D):

$$(\rho/\rho_c)_{c,o} = (1/2)\left[1 - \frac{(L/R)}{[(L/R)^2 + 1]^{1/2}} \right] \, . \quad (2.1-17)$$

For positions on the exit other than center, equation (2.1-16) is integrated numerically by the procedure described in Appendix 2.1-D.

The equation for the density at r/R for molecules reaching the exit after n collisions is obtained from equation (2.1-15) and is as follows:

$$(\rho/\rho_c)_{r/R, n} = \frac{1}{4(T_m/T_c)^{1/2}} \int (q_w/q_c)_{x/L, n-1} \, (d\omega/\pi) \qquad (2.1\text{-}18)$$

where (Appendix 2.1-E):

$$T_m/T_c = (1-\alpha)^n + \alpha(T_s/T_c) \sum_{i=0}^{n-1} (1-\alpha)^i \qquad (2.1\text{-}19)$$

and the integration is performed numerically over the solid angle enclosed by the duct wall by the procedure described in Appendix 2.1-D . The mean velocity ratio is equal to the square root of the temperature ratio because of the assumption of a Maxwellian velocity distribution at all times (Ref. 2.1-12).

The contribution to the center exit density is presented in Fig. 2.1-5 and -6 as a function of collisions number for a duct of dimensions L/R = 2.0, and various duct temperatures and thermal accommodation coefficients. As with the molecular flux, the contributions rapidly become insignificant with increasing collision number.

The total density at a point on the exit is found by summing the contributions for each collision:

$$(\rho/\rho_c)_{r/R} = \sum_{n=0}^{\infty} (\rho/\rho_c)_{r/R, n} \, . \qquad (2.1\text{-}20)$$

As with the total flux calculations, the summation was carried out to 20 collisions for the results reported herein.

The total exit density distribution is shown in Fig. 2.1-7 along with the contributions of the first few collisions for a duct of dimensions $L/R = 2.0$ with a duct to reservoir temperature ratio T_s/T_o of unity. The variation of the total exit density distribution with duct temperature is shown in Fig. 8 for a duct of the same dimensions with a thermal accommodation coefficient of unity. As with the flux distribution, a sharp "boundary-layer" like decrease in magnitude at the edge is noted. It is also observed that the exit density decreases with increasing duct temperature.

The variation of exit density disbribution with thermal accommodation coefficient for two duct temperatures is shown in' Fig. 2.1-9 . It is seen that for a duct to reservoir temperature ratio T_s/T_o, greater than unity, the density ratio ρ/ρ_o increases with decreasing thermal accommodation coefficient α; while for T_s/T_o less than unity, ρ/ρ_o decreases with decreasing α. In both cases ρ/ρ_o approaches the condition for T_s/T_o equal to unity as α approaches zero. From equation (2.1-19) it is seen that T_s/T_o equal to unity with any α yields the same results as T_s/T_o not equal to unity with an α equal to zero.

In Fig. 2.1-10 and -11 is shown the variation of the center exit density with duct temperature and thermal ac-

-14-

commodation coefficient for ducts of dimensions $L/R = 2.0$
and $L/R = 4.0$. Comparing the two figures shows that the
density has decreased considerably by increasing L/R. Note
that the curves intersect at $T_s/T_o = 1.0$ and spread as
T_s/T_o approaches zero or infinity. The amount of density
variation shown in these figures indicates the feasibility
of an experimental determination of the thermal accommoda-
tion coefficient by measuring the effect of the duct wall
temperature on the density field.

Density on Center Line

The center line density distribution is found by
integrating equations (2.1-15) and (-16) from a point on
the center line. The resulting equations are:

$$(\rho/\rho_0)_{x/L,0} = (1/2)\left[1 - \frac{(L/R)\,(x/L)}{\left[(L/R)^2(x/L)^2 + 1\right]^{1/2}}\right] \qquad (2.1\text{-}21)$$

for zero collisions, and:

$$(\rho/\rho_0)_{x/L,n} = \frac{1}{4\,(T_w/T_o)^{1/2}}\int (q_w/q_o)_{x/L,n-1}\,(d\omega/\pi) \qquad (2.1\text{-}22)$$

for n collisions. Equation (2.1-22) is integrated numeri-
cally over the solid angle enclosed by the duct wall in a
manner similar to the integration of equation (2.1-18).
The derivation of equation (2.1-21) and the procedure for
integrating Equation (2.1-22) is described in Appendix

2.1-D. The total density is obtained by summing the con-
tributions for collision.

The total center line density distribution is pre-
sented in Fig. 2.1-12 along with the contributions of
the first few collisions for a duct of dimensions L/R =
2.0 and a duct to reservoir temperature ratio T_s/T_o of
unity. The variation of the center line density distri-
bution with duct temperature is shown in Fig. 2.1-13
for a duct with the same dimensions as in Fig. 2.1-12
and with a thermal accommodation coefficient of unity.
It is seen that the total density ratio ρ/ρ_o approaches
unity far upstream of the duct and zero far downstream.
The variation in density with duct temperature appears
to be most pronounced in the second quarter segment down-
stream of the duct entrance.

The variation of center line density distribution
with thermal accommodation coefficient is shown in (Fig.
2.1-14 for two duct temperatures. The variation here
follows the same pattern as in Fig. 2.1-9 .

Accuracy of Results

It was mentioned in the discussion of flow rates
that for an L/R ratio of 2.0 the present calculations of
flow rates are within 0.1 percent of the results of Clausing
(Ref. 2.1-2). Demarcus (Ref. 2.1-4) showed that Clausing's
flow rate calculation for a duct of those dimensions are

correct to within 0.12 percent. Since the present calcula-
tions of density are computed essentially in the same manner
as the present calculations of molecular flux and flow rates,
it is inferred that the density results are correct to within
at most one or two percent.

Computer Program

The calculations described herein were performed
on an IBM 7090 Computer. The computer program was writ-
ten in Fortran IV language and is presented in Appendix
2.1-F.

2.1.5 Possible Experimental Verification

Most available publications dealing with density
measurements in rarefied gas flow describe techniques
utilizing scattering and attenuation of various beams
such as electron beams (Ref. 2.1-23,-24) and gamma radi-
ation (Ref. 2.1-25). It is recommended that the electron
beam scattering technique described in Ref. 2.1-23,-24
be investigated as the most promising approach to exper-
imental verification of the results reported herein.

2.1.6 Conclusions

1. Nearly all of the molecules which pass through a duct
of dimensions L/R = 2.0 under conditions of free molecule
flow have fewer than 10 internal collisions during passage
through the duct.

2. The molecular flux to the duct wall is a nearly linear function of axial distance for a duct of dimensions L/R = 2.0.

3. The molecular flux and volume density are nearly uniformly distributed over the duct exit with the exception of a sharp - "boundary-layer" like decrease in magnitude at the edge.

4. For a duct of dimensions L/R = 2.0 with a thermal accommodation coefficient of unity, an increase by a factor of two in the duct temperature from the ambient gas temperature results in a decrease in exit density of approximately 30 percent.

5. An experimental determination of the thermal accommodation coefficient by measuring the effect of the duct wall temperature on the density field appears feasible.

2.1.7 References

2.1-1. Knudsen, M., Ann Physik, $\underline{28}$, 75,999 (1909); $\underline{35}$, 389 (1911).

  -2. Clausing, P., Ann Physik, $\underline{12}$, 961 (1932).

  -3. Hottel, H. C. and Keller, J. D., Trans, ASME, $\underline{IS-55-6}$, 39 (1933).

  -4. Demarcus, W. E. and Hopper, E. H., J. Chem. Phys, $\underline{23}$, 1344 (1955).

  -5. Pollard, W. G., and Present, R. D., Phys, Rev. $\underline{73}$, 762 (1963).

  -6. Lozgachev, V. I., Soviet Physics-Technical Physics $\underline{7}$, 745, 827 (1963).

  -7. German, O., Soviet Physics-Technical Physics, $\underline{7}$, 834 (1963).

-8. Carlson, K. D., Gillis, P. W., and Thorn, R. J., J. Chem Phys, $\underline{38}$, 2064 (1963).

-9. Ivanov, B. S., Troitskii, V. S., Soviet Physics-Technical Physics $\underline{8}$, 365 (1963).

-10. Troitskii, V. S., Soviet Physics-Technical Physics $\underline{7}$, 353 (1962).

-11. Demarcus, W. C., Oak Ridge Gaseous Diffusion Plant Rept. K-1302, Parts I-VI (1956-7).

-12. Bird, G. A., Rarefied Gas Dynamics, edited by L. Talbot (Pergamon Press, Inc., New York, 1960) pp 245-60.

-13. Touryan, K. J., AIAA Jour., $\underline{2}$, 559 (1964).

-14. Howard, W. M., Phys. Fluids, $\underline{4}$, 521 (1961).

-15. Gustafson, W. A. and Kiel, R. E., Phys. Fluids, $\underline{7}$ 472 (1964).

-16. Sparrow, E. M., and Haji-Sheikh, A., Phys. Fluids $\underline{7}$, 1256 (1964).

-17. Knudsen, M., The Kinetic Theory of Gases, John Wiley & Sons, Inc. New York, 1950.

-18. Ballance, J. O., Roberts, W. K., and Tarbell, D. W., "A Study of Cryopump Configurations in Free-Molecular Flow Regions", Advances in Cryogenic Engineering, Vol. 8, p. 57- Plenum Press, New York, 1963.

-19. Davis, D. H., J. Appl. Phys., $\underline{31}$, 1169 (1960).

-20. Link, C. H., "Molecular Kinetics Studies" AEDC-TDR-63-120, Arnold Engineering Development Center, Tenn., 1963.

-21. Kennard, E. H., Kinetic Theory of Gases, McGraw Hill Book Company, New York, 1938, Chapt. 3.

-22. Hamilton, D. C., and Morgan, W. R., "Radiant-Inter-change Configuration Factors", NACA TN 2836, National Advisory Committee for Aeronautics, 1952.

-23. Hurlbut, F. C., J. Appl. Phys. $\underline{30}$, 273-9 (1959).

-24. Marton, L., Schubert, D. C., and Mielczarek, S. R., "Electron Optical Studies of Low-Pressure Gases", National Bureau of Standards Monograph 66 (1963).

-25. Shephard, J. E. and Dick, J. B., "A Technique for Measuring a Local Gas Density Using Scattered Gamma Radiation", AEDC-TDR-63-87, Arnold Engineering Development Center, Tenn., 1963.

-26. Hartnett, J. P., Rarefied Gas Dynamics, Edited by L. Talbot (Pergamon Press, Inc., New York, 1960) p. 1.

APPENDIX 2.1-A

PROCEDURE FOR NUMERICAL INTEGRATION OF FLUX EQUATIONS

The numerical integrations of equations (2.1-4) and (-9) were accomplished by dividing the duct into 50 identical circular elements as illustrated below:
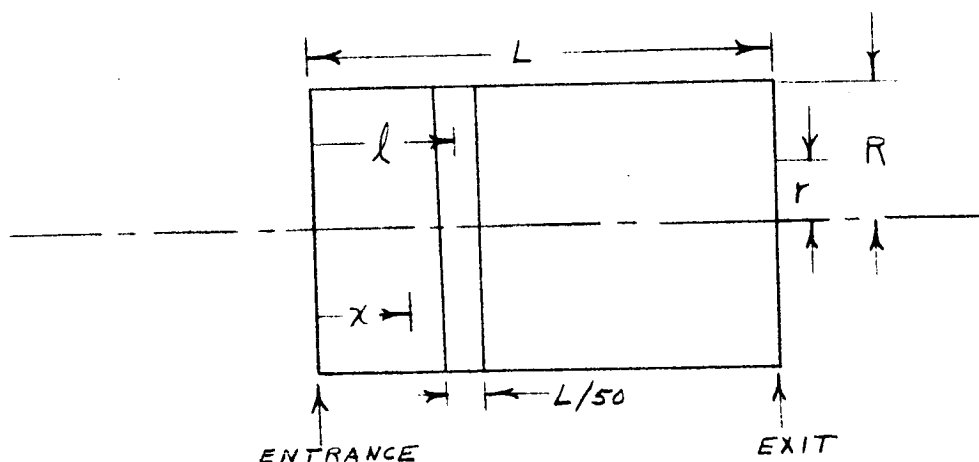
The average value of (q_W/q_o) and F_{WW} over a ring element are taken to be those calculated at the circle halving the element. Equation (2.1-4) then becomes:

$$\left(q_W/q_o\right)_{x/L,\, n} = (1/50) \sum_{i=1}^{50} \left[(F_{WW}) | (x/L) - (i-1/2)/50 | \right]$$

(2.1-A-1)

$$\left(q_W/q_o\right)_{(i-1/2)/50,\, n-1}.$$

Equation (2.1-9) becomes:

$$\left(q_E/q_o\right)_{x/L,\, n} = (1/50) \sum_{i=1}^{50} \left[(F_{WE})_{(i-1/2)/50,\, r/R} \right]$$

$$\left(q_W/q_o\right)_{(i-1/2)/50,\, n-1}.$$

(2.1-A-2)

-21-

APPENDIX 2.1-B

DERIVATION OF WALL TO EXIT FORM FACTOR

The form factor given by equation (2.1-10) is derived by the method of Ref. 2.1-3 utilizing the following illustration:
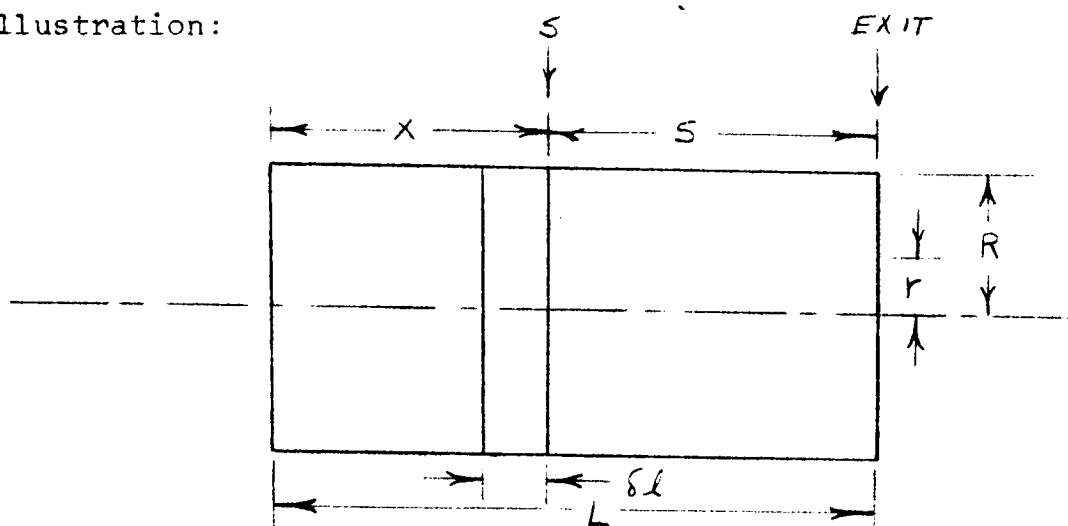
The molecular flux at r on the exit due to collisionless traversing of molecules from a disc S enclosed by a cylinder at a distance ℓ from the exit is:

$$q_E = F(\ell)q \tag{2.1-B-1}$$

where q is the flux across the disc S.

The flux from a disc at $\ell + \delta\ell$ from the exit is:

$$q_E + \delta q_E = F(\ell)q + F'(\ell)\delta\ell q \cdot \tag{2.1-B-2}$$

The quantity $\delta q_E = F'(\ell)\delta\ell$ is actually negative due to decreasing $F(\ell)$ with increasing ℓ and may be considered due to the flux q from the wall strip enclosed by $\delta\ell$.

Therefore, the form factor for flux from a wall element $\delta\ell$ wide is $-F'(\ell)\delta\ell$.

The form factor, F, for flux from the disc S in the preceding illustration is (Ref. 2.1-22):

$$F = (1/2)\left[1 - \frac{(r/R)^2 + (L/R)^2(\ell/L)^2 - 1}{\left\{\left[(r/R)^2 + (L/R)^2(\ell/L)^2 + 1\right]^2 - 4(r/R)^2\right\}^{1/2}}\right]. \qquad (2.1\text{-}B\text{-}3)$$

The form factor given by equation (2.1-10) is obtained from equation (2.1-B-3) by:

$$(F_{WE})_{x/L,\, r/R} = -F'(x)$$

$$= 2(L/R)^2(x/L)\left[\frac{(L/R)^2(1-x/L)^2 - (r/R)^2 + 1}{\left\{\left[(L/R)^2(x/L)^2 + (r/R)^2 + 1\right]^2 - 4(r/R)^2\right\}^{3/2}}\right] \qquad (2.1\text{-}B\text{-}4)$$

or

$$(F_{WE})_{x/L,\, r/R} = 2(L/R)^2(1-x/L)\left[\frac{(L/R)^2(1-x/L)^2 - (r/R)^2 + 1}{\left\{\left[(L/R)^2(1-x/L)^2 + (r/R)^2 + 1\right]^2 - 4(r/R)^2\right\}^{3/2}}\right]. \qquad (2.1\text{-}B\text{-}5)$$

APPENDIX 2.1-C

INTEGRATION PROCEDURE FOR TOTAL FLOW RATE

The numerical procedure for integrating equation (2.1-12) is similar to the procedure described in Appendix 2.1-A. In this case, however, the trapezoidal rule was utilized as follows:

$$Q_E / \pi R^2 q_0 = 2 \int_0^1 (q_E/q_0)_{r/R} \, (r/R) \, d(r/R)$$

$$= (1/1250) \sum_{i=1}^{49} i (q_E/q_0)_{i/50} + (1/50)(q_E/q_0)_{1.0} \qquad (2.1\text{-}C\text{-}1)$$

where i is an integer from one to **49** and the radius R is divided into 50 equal elements, R/50.

APPENDIX 2.1-D

DERIVATION OF DENSITY EQUATIONS

Exit Density

Zero Collisions

The center exit density for zero collisions is
obtained by integrating equation (2.1-16) over the solid
angle enclosed by the entrance as illustrated:
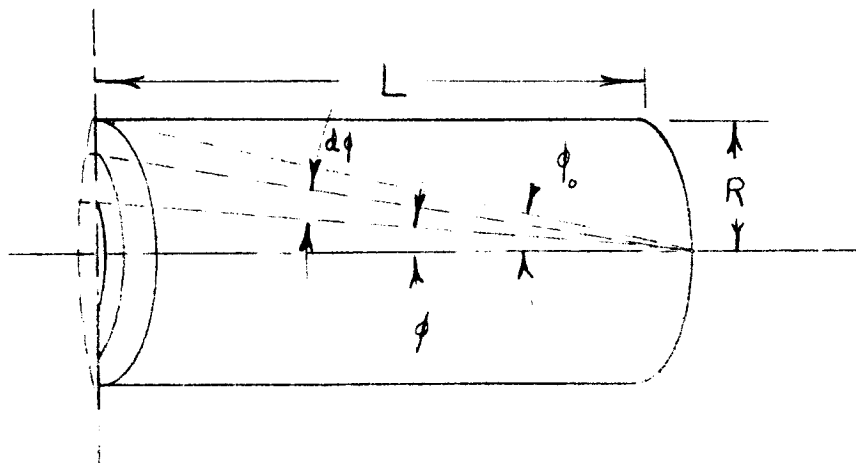
$$(\rho/\rho_c)_{0,0} = (1/4) \int d\omega / \pi$$

$$= (1/2) \int_0^{\phi_0} \sin \phi \, d\phi$$

$$= (1/2) \left[1 - \frac{(L/R)}{\left[(L/R)^2 + 1 \right]^{1/2}} \right].$$

(2.1-D-1)

For positions on the exit other than center a numerical integration is performed as illustrated:
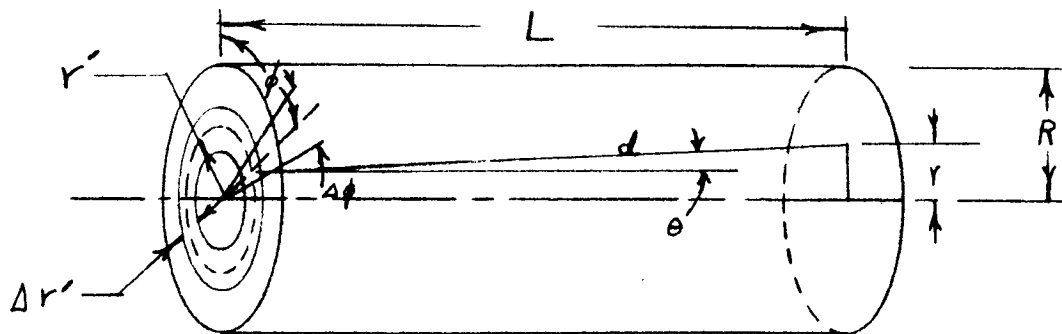
The element of solid angle $\Delta\omega$ enclosed by the element of area defined by $\Delta\phi$ and $\Delta r'$ is Equation (2.1-13):

$$\Delta\omega = \lim_{\substack{\Delta\phi \to 0 \\ \Delta r \to 0}} r'\Delta\phi\, \Delta r' \cos\theta/d^2 \qquad (2.1\text{-}D\text{-}2)$$

where r´ and ϕ are taken at the midpoint of the element. Now:

$$\cos\theta = L/d \qquad (2.1\text{-}D\text{-}3)$$

and

$$d = \left(L^2 + r^2 + r'^2 - 2rr'\cos\phi\right)^{1/2} . \qquad (2.1\text{-}D\text{-}4)$$

We will choose $\Delta r' = R/20$ and $\Delta\phi = \Pi/20$. Equation (2.1-D-2)

then becomes:

$$\Delta \omega = \left[\frac{(\pi/8000)(L/R)(i-1/2)}{\left\{ (L/R)^2 + (r/R)^2 + \frac{(i-1/2)^2}{400} - \frac{(i-1/2)}{10}(r/R)\cos\left[\frac{(j-1/2)\pi}{20}\right]\right\}^{3/2}} \right]$$

(2.1-D-5)

where i and j are integers from one to twenty.

The integral of equation (2.1-16) over the solid
angle enclosed by the entrance would be twice the summation
of equation (2.1-D-5) for i and j from one to twenty:

$$(\rho/\rho_0)_{r/R,0} = \left[(L/R)/16,000 \right]$$

$$\sum_{j=1}^{20} \sum_{i=1}^{20} \frac{(i-1/2)}{\left\{ (L/R)^2 + (r/R)^2 + \frac{(i-1/2)}{400} - \frac{(i-1/2)}{10}(r/R)\cos\left[\frac{(j-1/2)\pi}{20}\right]\right\}^{3/2}}.$$

(2.1-D-6)

n Collisions

The exit density for n collisions is obtained by
integrating equation (2.1-18) in a manner similar to the
above described integration of equation (2.1-16):

-27-
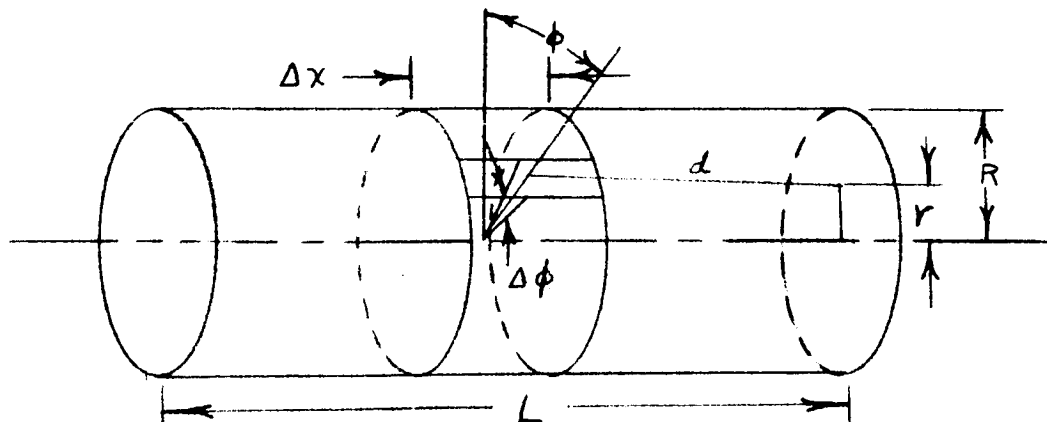
The element of solid angle $\Delta\omega$ enclosed by the element of area defined by $\Delta\phi$ and Δx is (equation 2.1-13):

$$\Delta\omega = \lim_{\substack{\Delta\phi \to 0 \\ \Delta x \to 0}} R\,\Delta\phi\,\Delta x\,(R - r\cos\phi)/d^3 \qquad (2.1\text{-}D\text{-}7)$$

We choose $\Delta x = L/50$ and $\Delta\phi = \pi/20$ so that equation (2.1-D-7) becomes:

$$\Delta\omega = \frac{\pi[(L/R)/1000]\{1 - (r/R)\cos[(j-1/2)\pi/20]\}}{\left\{1 + (L/R)^2\left[1 - \frac{(i-1/2)^2}{50}\right] + (r/R)^2 - 2(r/R)\cos\left[\frac{(j-1/2)\pi}{20}\right]\right\}^{3/2}} \qquad (2.1\text{-}D\text{-}8)$$

where i is an integer from one to fifty and j is an integer from one to twenty. The integral of equation (2.1-18) over the solid angle enclosed by the duct wall would then become:

$$(\rho/\rho_c) = \frac{(L/R)}{2000(T_m/T_o)^{1/2}} \sum_{i=1}^{50} (q_w/q_o)_{(i-1/2)/50,\,r-1}$$

$$\sum_{j=1}^{20} \frac{1 - (r/R)\cos[(j-1/2)\pi/20]}{\left\{1 + (L/R)^2\left[1 - \frac{(i-1/2)^2}{50}\right] + (r/R)^2 - 2(r/R)\cos\left[\frac{(j-1/2)\pi}{20}\right]\right\}^{3/2}} \qquad (2.1\text{-}D\text{-}9)$$

Center-Line Density

Zero Collisions

The derivation of the center-line density equation for zero collisions is very similar to that derived for the
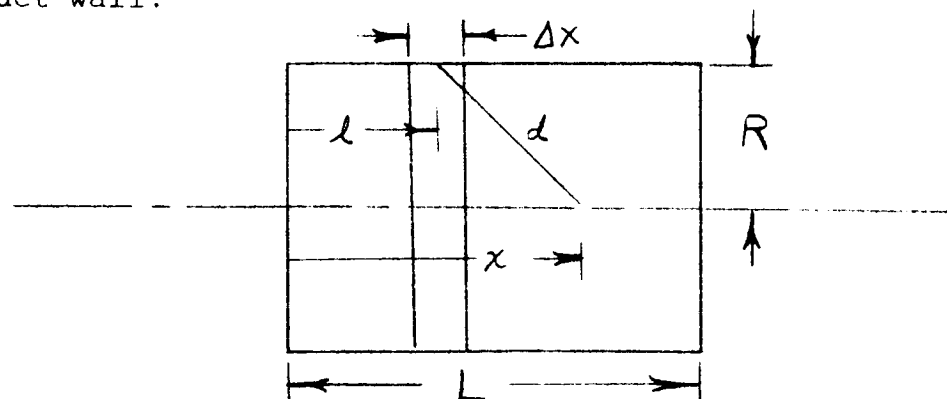
center exit:
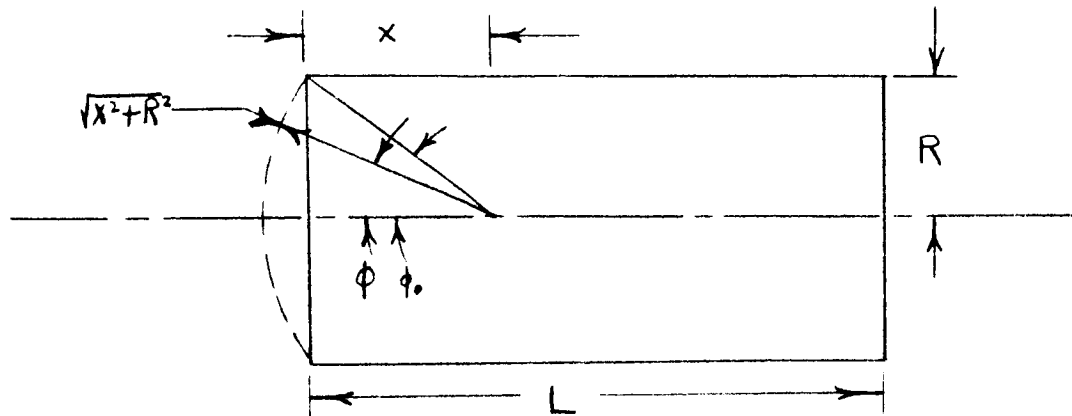
$$(\rho/\rho_0)_{x/L,0} = (1/2)\int_0^{\phi_0} \sin\phi\, d\phi$$

$$= (1/2)\left[1 - \frac{(L/R)(x/L)}{[(L/R)^2(x/L)^2+1]^{1/2}}\right] \cdot \quad (2.1\text{-}D\text{-}10)$$

n Collisions

The center-line density for n collisions is obtained by integrating equation (2.1-22) over the solid angle enclosed by the duct wall:

The element of solid angle $\Delta\omega$ enclosed by the ring element of duct wall Δx is:

$$\Delta\omega = \lim_{\Delta x \to 0} 2\pi R^2 \Delta x / d^3 .$$

(2.1-D-11)

We will choose $\Delta x = L/50$ so that equation (2.1-D-11) becomes:

$$\Delta\omega = \frac{(\pi/25)(L/R)}{\left\{1 + (L/R)^2\left[(x/L) - \frac{(i-1/2)}{50}\right]^2\right\}^{3/2}}$$

(2.1-D-12)

where i is an integer from one to 50.

The average value of $(q_W/q_o)_{x/L, n-1}$ over a ring element was taken to be the value calculated at the circle halving the element. The integral in equation (2.1-22) then becomes:

$$(P/P_o)_{x/L, n}$$

$$= \frac{(L/R)}{100(T_m/T_o)} \sum_{i=1}^{50} \frac{(q_W/q_o)_{(i-1/2)/50, n-1}}{\left\{1 + (L/R)^2\left[(x/L) - \frac{(i-1/2)}{50}\right]^2\right\}^{3/2}} .$$

(2.1-D-13)

APPENDIX 2.1-E

DERIVATION OF GAS TEMPERATURE

AFTER n COLLISIONS

The thermal accommodation coefficient α may be de-
fined by (2.1-26):

$$\alpha = (T_1 - T_0)/(T_s - T_0) \qquad \text{(2.1-E-1)}$$

where T_1 is the energy (temperature) of the gas leaving the
surface after one collision , T_s is the surface temperature,
and T_0 is the gas temperature prior to the first collision.
Rearranging equation (2.1-E-1) yields the expression for the
gas temperature after one collision:

$$T_1/T_0 = (1 - \alpha) + \alpha (T_s/T_0). \qquad \text{(2.1-E-2)}$$

Extending this equation to the nth collisions yields:

$$T_n/T_0 = (1 - \alpha)^n + \alpha \sum_{i=0}^{n-1} (1 - \alpha)^i T_s/T_0 . \qquad \text{(2.1-E-3)}$$

APPENDIX 2.1-F

COMPUTER PROGRAM

The computer program utilized in obtaining the here-
in reported results is given on the following four pages
written in Fortran IV language.

```
$JOB            3S/P ARMSTRONG       ,346821,00,12,1900,
.$EXECUTE        IBJOB
$IBJOB AMSTNG  LOGIC,MAP,FILES
$IBFTC MOLFLO  LIST,REF,M94,XR7,DECK
        DIMENSION SUMJ(50,51)
        DIMENSION  T(51),QE(51,51),DEN(51,51),XDEN(50,51),QW(50,51)
        DIMENSION  FWE(50,51),FWW(50,50),RQE(51),RDEN(51),RXDEN(50)
        DIMENSION  RQW(50),SQW(51)
6742    CONTINUE
        CALL MAVRIK(ERR,5HTSOTO,TSOTO,5HALPHA,ALPHA,4HMAXN,MAXN,
      1  4HXLOR,XLOR)
        IF(ERR.NE.0.) CALL DUMP
        PI=3.1415926
        N=1
        WRITE(6,9876)
9876    FORMAT(1H1,32HFREE MOLECULE FLOW THROUGH DUCTS//)
        WRITE(6,4923)TSOTO,ALPHA,XLOR
4923    FORMAT(1H ,6HTS/TO=1PE15.7,1X,6HALPHA=1PE15.7,1X,4HL/R=1PE15.7//)
        T(N)=1.
        ROR=0.
        DO 35 K=1,51
        QE(K,N)=.5*(1.-(XLOR**2+ROR**2-1.)/SQRT((XLOR**2+ROR**2+1.)**2-
      2  4.*ROR**2))
        IF(K.NE.1) GO TO 58
        DEN(K,N)=.5*(1.-XLOR/SQRT(XLOR**2+1.))
        GO TO 59
  58    DEN(K,N)=0.
        DO 4 J=1,20
        DO 4 I=1,20
        XI=I
        XJ=J
        DEN(K,N)=DEN(K,N)+(XI-.5)/(XLOR**2+ROR**2+(XI-.5)**2/400.-(XI-.5)
      2  *ROR/10.*COS((XJ-.5)*PI/20.))**(3./2.)
  4     CONTINUE
        DEN(K,N)=DEN(K,N)*XLOR/16000.
  59    CONTINUE
        ROR=ROR+.02
  35    CONTINUE
        XOL=0.01
        DO 36 L=1,50
        QW(L,N)=.5*(((XLOR**2*XOL**2+2.)/SQRT(XLOR**2*XOL**2+4.))-
      2  XLOR*XOL)
        XOL=XOL+.02
  36    CONTINUE
        XOL=-1.
        DO 876  L=1,31
        XDEN(L,N)=.5*(1.-XLOR*XOL/SQRT(XLOR**2*XOL**2+1.))
        XOL=XOL+.1
 876    CONTINUE
        XOL=.01
        DO 9 L=1,50
        ROR=0.
        DO 10 K=1,51
        SUMJ(L,K)=0.
        DO 361 J=1,20
        XJ=J
        SUMJ(L,K)=SUMJ(L,K)+(1.-ROR*COS((XJ-.5)/20.*PI))/(1.+XLOR**2*
      X  (1.-XOL)**2+
      2  ROR**2-2.*ROR*COS((XJ-.5)/20.*PI))**(3./2.)
 361    CONTINUE
```

```fortran
      FWE(L,K)=2.*XLOR**2*(1.-XOL)*(XLOR**2*(1.-XOL)**2-ROR**2+1.)/
     2  ((XLOR**2*(1.-XOL)**2+ROR**2+1.)**2-4.*ROR**2)**(3./2.)
      ROR=ROR+.02
10    CONTINUE
      XLOL=.01
      DO 11 M=1,50
      FWW(L,M)=1.-XLOR*ABS(XOL-XLOL)*(XLOR**2*(XOL-XLOL)**2+6.)/
     2  (XLOR**2*(XOL-XLOL)**2+4.)**(3./2.)
      XLOL=XLOL+.02
11    CONTINUE
      XOL=XOL+.02
 9    CONTINUE
      DO 38 N=1,MAXN
      IF(N.EQ.1) GO TO 720
      SUMTS=0.
      NN=N-1
      IF(ALPHA.EQ.1.) GO TO 100
      DO 1 II=1,NN
      I=II-1
      SUMTS=SUMTS+(1.-ALPHA)**I*TSOTO
 1    CONTINUE
      T(N)=(1.-ALPHA)**NN+SUMTS*ALPHA
100   IF(ALPHA.EQ.1.)T(N)=TSOTO
      ROR=0.
      DO 962 K=1,51
      DEN(K,N)=0.
      QE(K,N)=0.
      XOL=0.01
      DO 965 L=1,50
      QE(K,N)=QE(K,N)+FWE(L,K)*QW(L,NN)
      DEN(K,N)=DEN(K,N)+QW(L,NN)*SUMJ(L,K)
      XOL=XOL+.02
965   CONTINUE
      QE(K,N)=QE(K,N)/50.
      DEN(K,N)=DEN(K,N)*XLOR/(2000.*SQRT(T(N)))
      ROR=ROR+.02
962   CONTINUE
      DO 903 L=1,50
      QW(L,N)=0.
      DO 963 M=1,50
      QW(L,N)=QW(L,N)+FWW(L,M)*QW(M,NN)
963   CONTINUE
      QW(L,N)=QW(L,N)*XLOR/100.
903   CONTINUE
      XOL=-1.
      DO 902 L=1,31
      XDEN(L,N)=0.
      DO 901 M=1,50
      XM=M
      XDEN(L,N)=XDEN(L,N)+QW(M,NN)/(1.+XLOR**2*(XOL-(XM-.5)/50.)**2)
     2  **(3./2.)
901   CONTINUE
      XDEN(L,N)=XDEN(L,N)*XLOR/(100.*SQRT(T(N)))
      XOL=XOL+.1
902   CONTINUE
720   CONTINUE
      NN=N-1
      WRITE(6,596)  NN,(QE(K,N),K=1,51),(DEN(K,N),K=1,51),(XDEN(L,N),
     1  L=1,31),(QW(L,N),L=1,50)
596   FORMAT(1H0,26X,I5,10HCOLLISIONS///X,9HQE VALUES,5X,6(2X,1PE15.7)/
```

```
      1. /7(15X,6(2X,1PE15.7)//)15X,3(2X,1PE15.7)//1X,10HDEN VALUES,4X,
      2 6(2X,1PE15.7)//7(15X,6(2X,1PE15.7)//),15X,3(2X,1PE15.7)//1X,
      3 14HC.L.DEN VALUES,6(2X,1PE15.7)//4(15X,6(2X,1PE15.7)//),15X,
      4 1(2X,1PE15.7)//,1X,9HQW VALUES,5X,6(2X,1PE15.7)//7(15X,
      5 6(2X,1PE15.7)//)15X,2(2X,1PE15.7)//)
   38    CONTINUE
         DO   12 K=1,51
         RQE(K)=0.
         RDEN(K)=0.
         DO 12 N=1,MAXN
         RQE(K)=RQE(K)+QE(K,N)
         RDEN(K)=RDEN(K)+DEN(K,N)
   12    CONTINUE
         WRITE(6,592) (RQE(K),K=1,51),(RDEN(K),K=1,51)
  592    FORMAT(1H0,29HTOTAL EXIT FLUX SUM QE VALUES//8(15X,6(2X,1PE15.7)
      1 //)15X,3(2X,1PE15.7)//1X,13HTOTAL DENSITY//8(15X,6(2X,
      2 1PE15.7)//)15X,3(2X,1PE15.7)//)
         DO   69  L=1,50
         RQW(L)=0.
         DO   69 N=1,MAXN
         RQW(L)=RQW(L)+QW(L,N)
   69    CONTINUE
         DO 880  L=1,31
         RXDEN(L)=0.
         DO 880  N=1,MAXN
         RXDEN(L)=RXDEN(L)+XDEN(L,N)
  880    CONTINUE
         WRITE(6,593)(RQW(L),L=1,50),(RXDEN(L),L=1,31)
  593    FORMAT(1H0,29HTOTAL WALL FLUX SUM QW VALUES//8(15X,6(2X,
      1 1PE15.7)//)15X,2(2X,1PE15.7)//1H0,25HTOTAL CENTER LINE DENSITY//
      2 5(15X,6(2X,1PE15.7)//)15X,1(2X,1PE15.7)//)
         QEINT=0.
         DO 964 K=2,50
         XK=K-1
         QEINT=QEINT+RQE(K)*XK
  964    CONTINUE
         QEINT=QEINT/1250.+RQE(51)/50.
         WRITE(6,765) QEINT
  765    FORMAT(1H0,16HTOTAL FLOW RATE=1PE15.7/)
         GO TO 6742
         STOP
         END
$DATA
 ALPHA=1.,TSOTO=.5,XLOR=4.0,MAXN=41,/
```
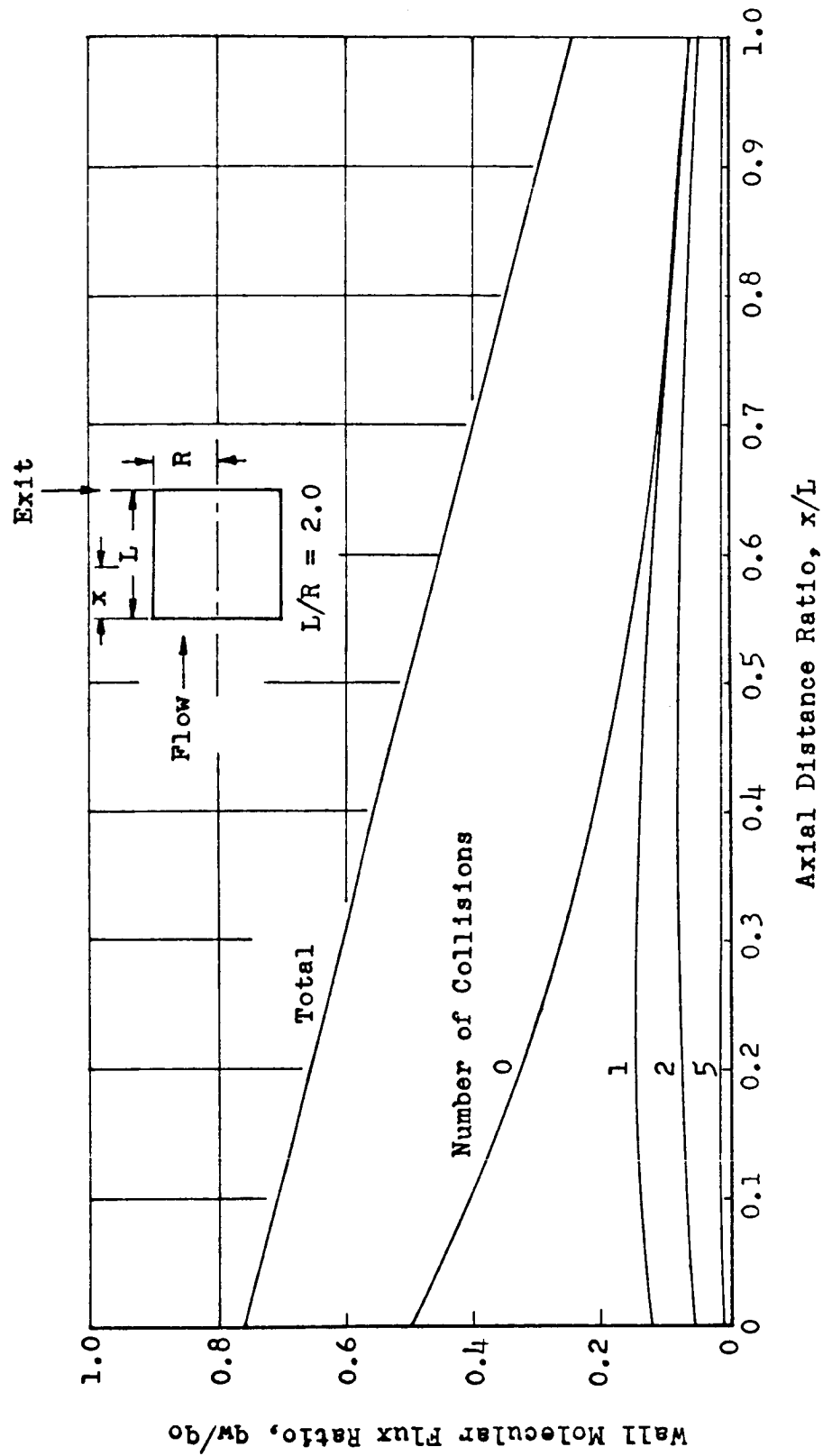
FIG. 2.1-1   WALL MOLECULAR FLUX AS A FUNCTION OF
NUMBER OF COLLISIONS AND POSITION
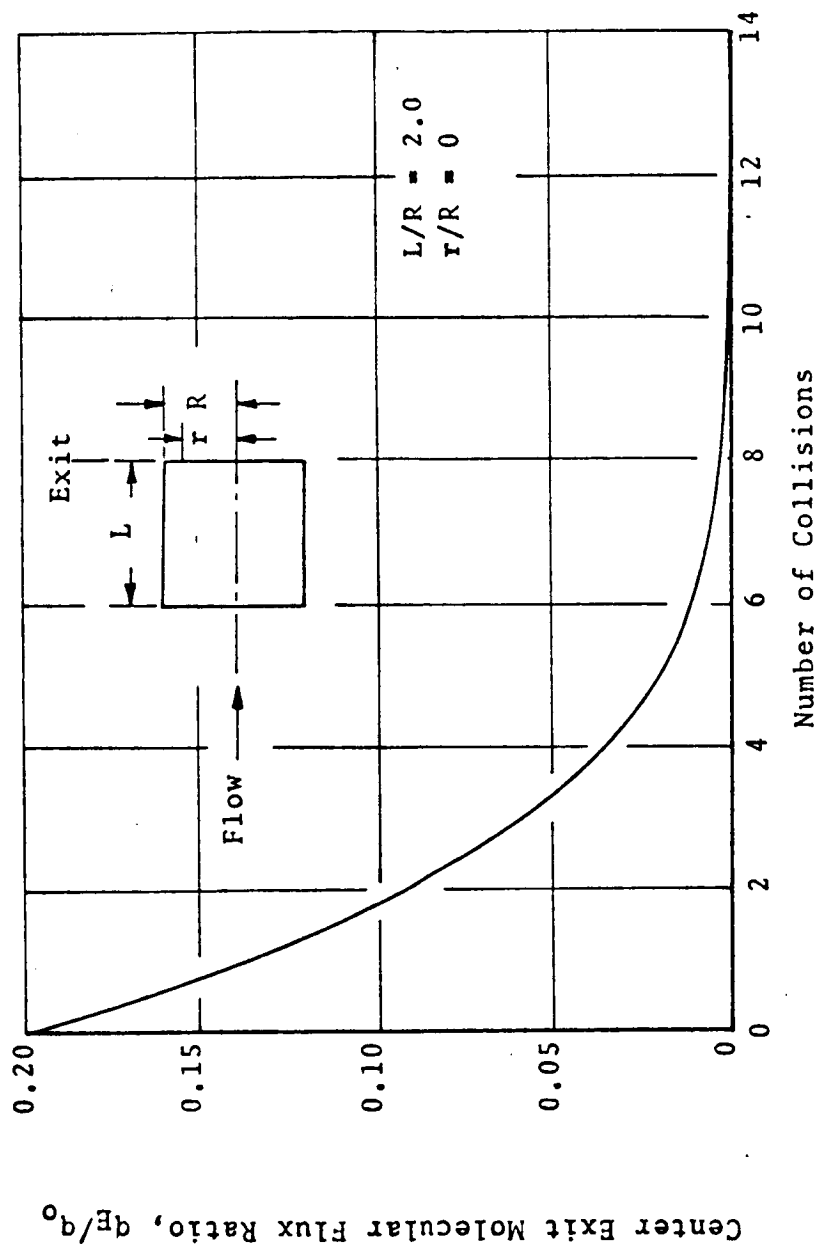
FIG. 2.1-2 CENTER EXIT MOLECULAR FLUX AS A FUNCTION
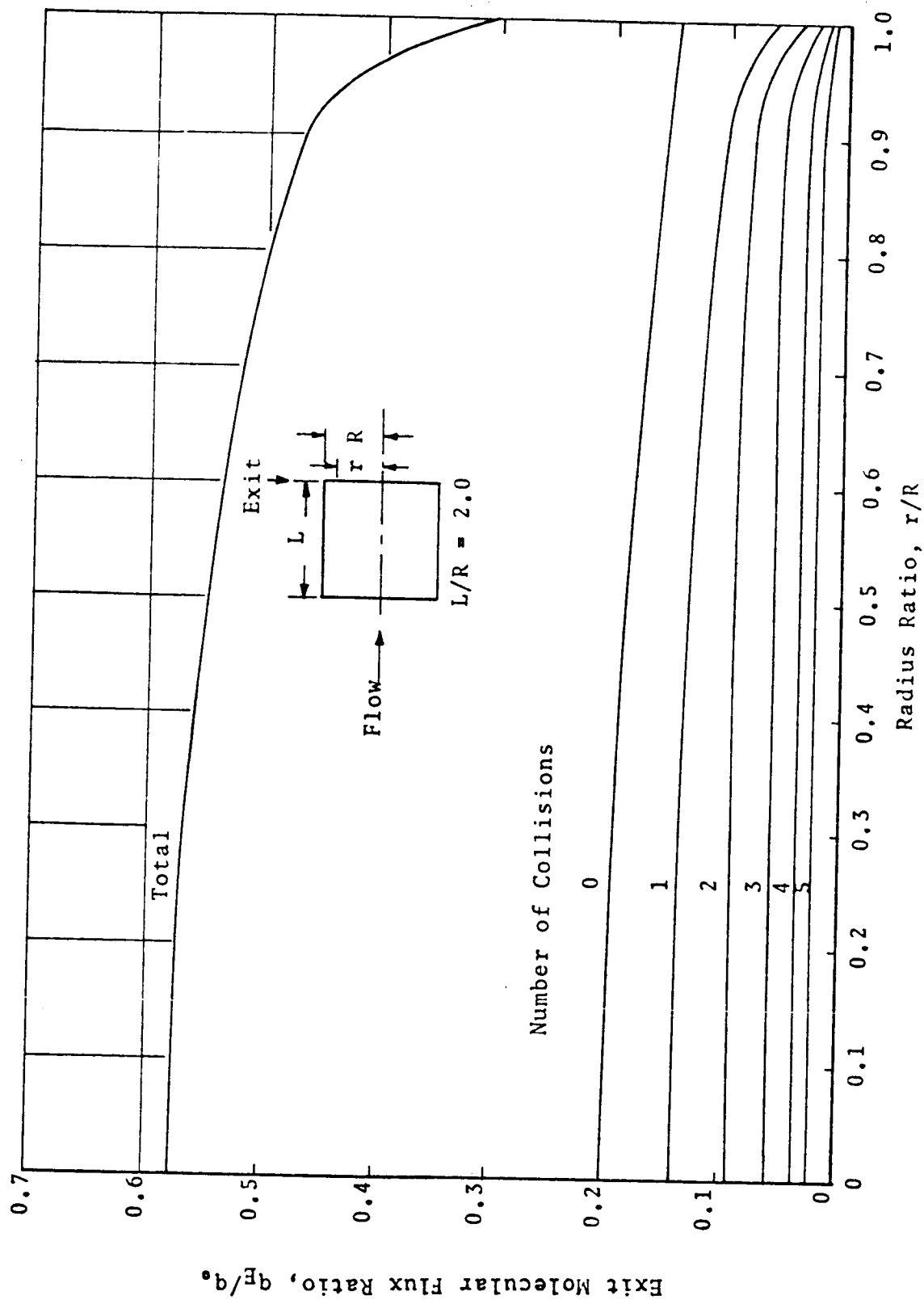OF NUMBER OF COLLISIONS

FIG. 2.1-3 EXIT MOLECULAR FLUX AS A FUNCTION OF
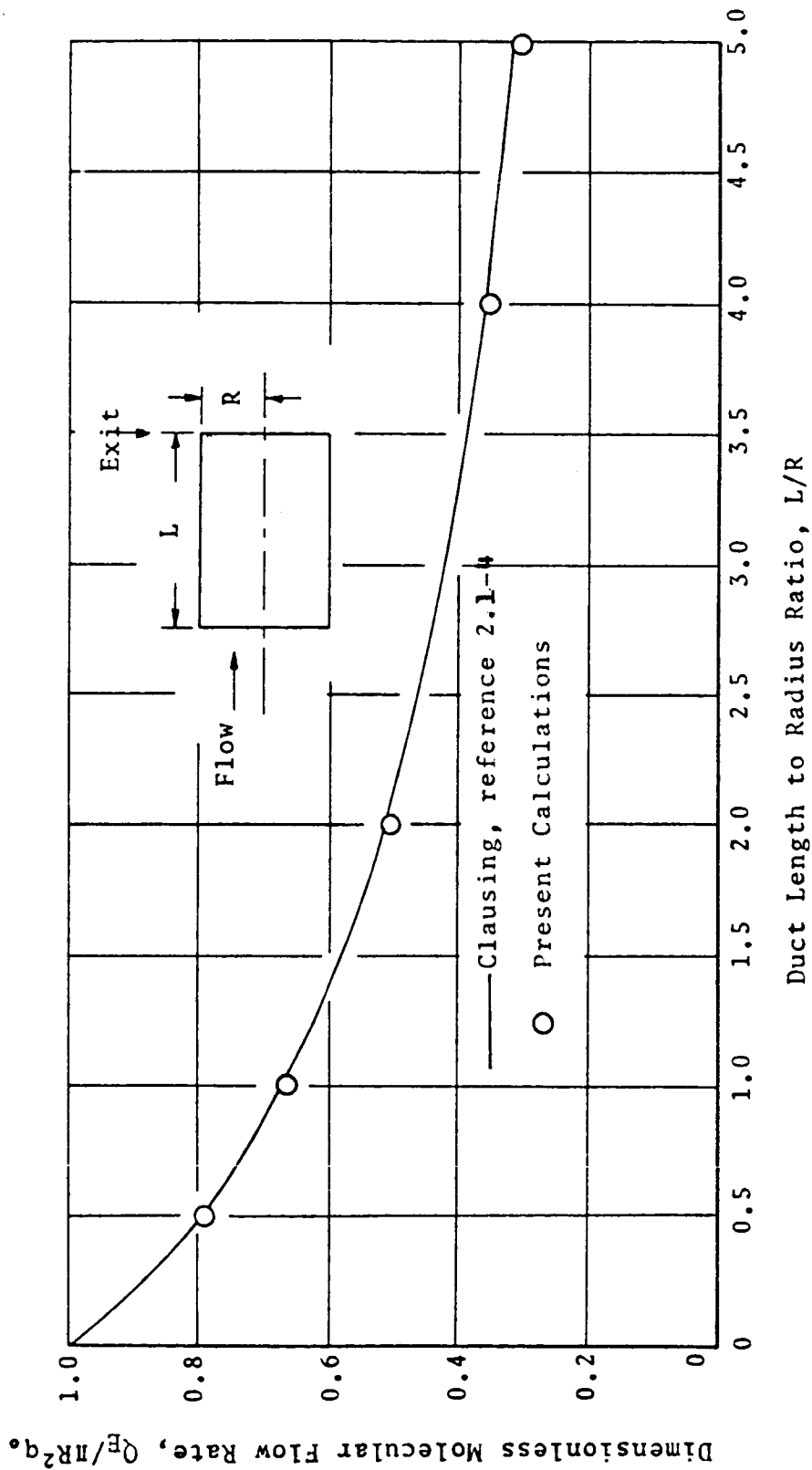NUMBER OF COLLISIONS AND POSITION

FIG. 2.1-4 MOLECULAR FLOW RATE THROUGH DUCT AS A FUNCTION OF DUCT LENGTH TO RADIUS RATIO, L/R
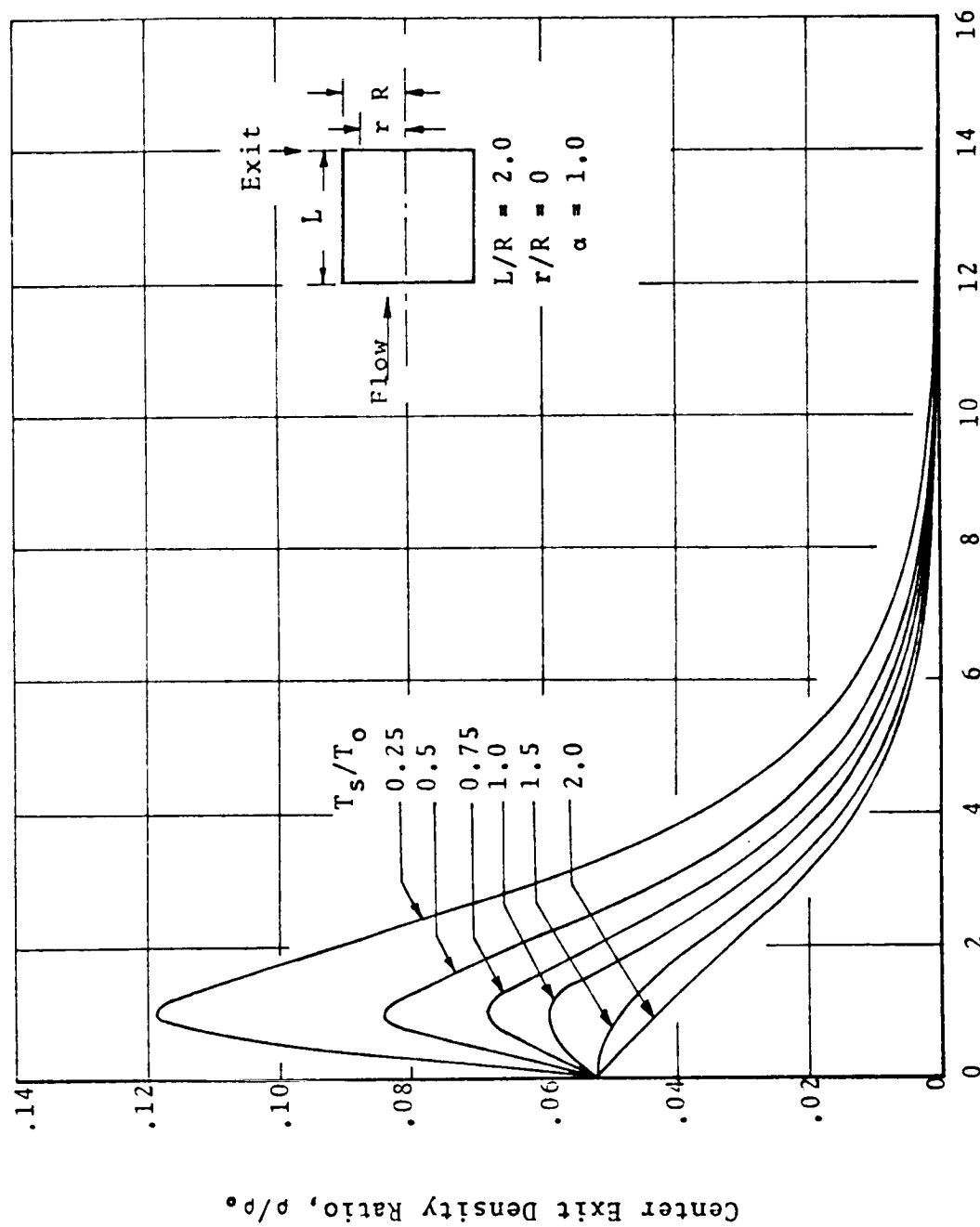
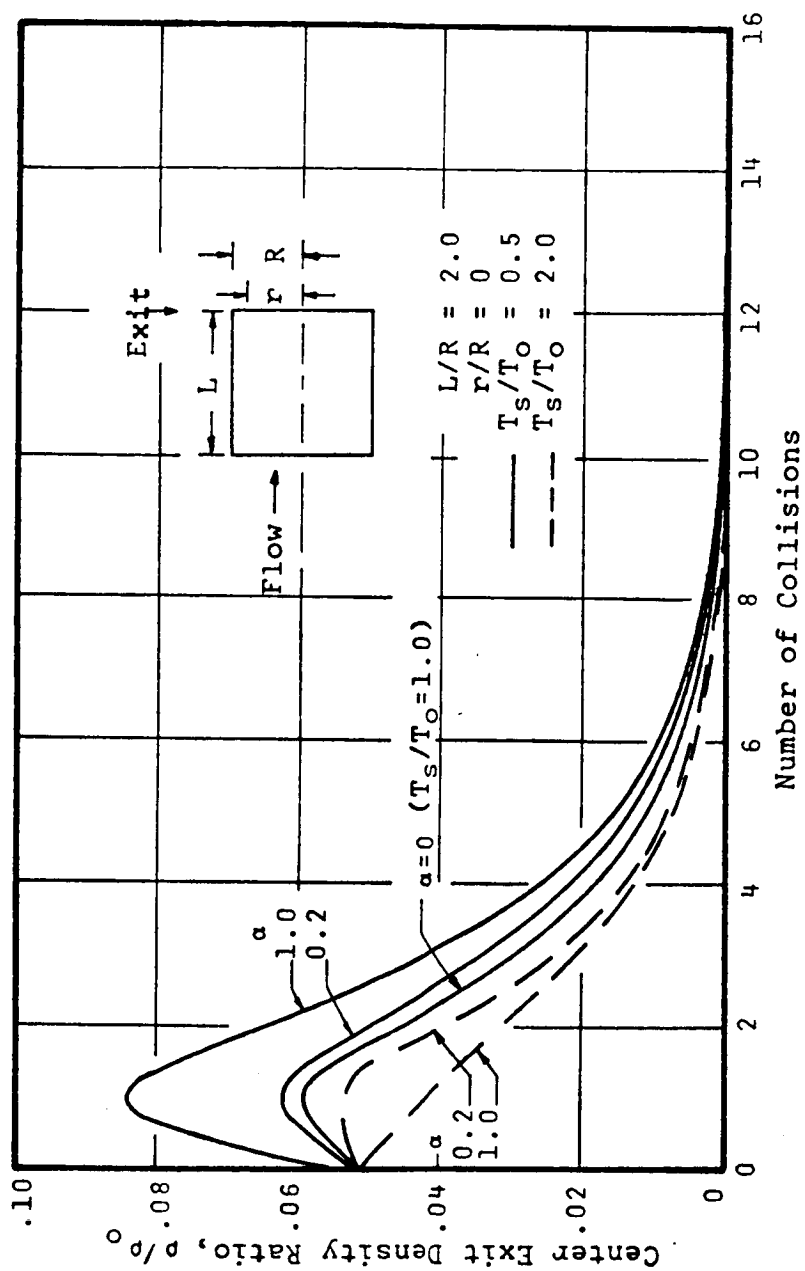FIG. 2.1-5 CENTER EXIT VOLUME DENSITY AS A FUNCTION OF NUMBER OF COLLISIONS AND DUCT TEMPERATURE

FIG. 2.1-6   CENTER EXIT VOLUME DENSITY AS A FUNCTION OF
NUMBER OF COLLISIONS AND THERMAL ACCOMODATION
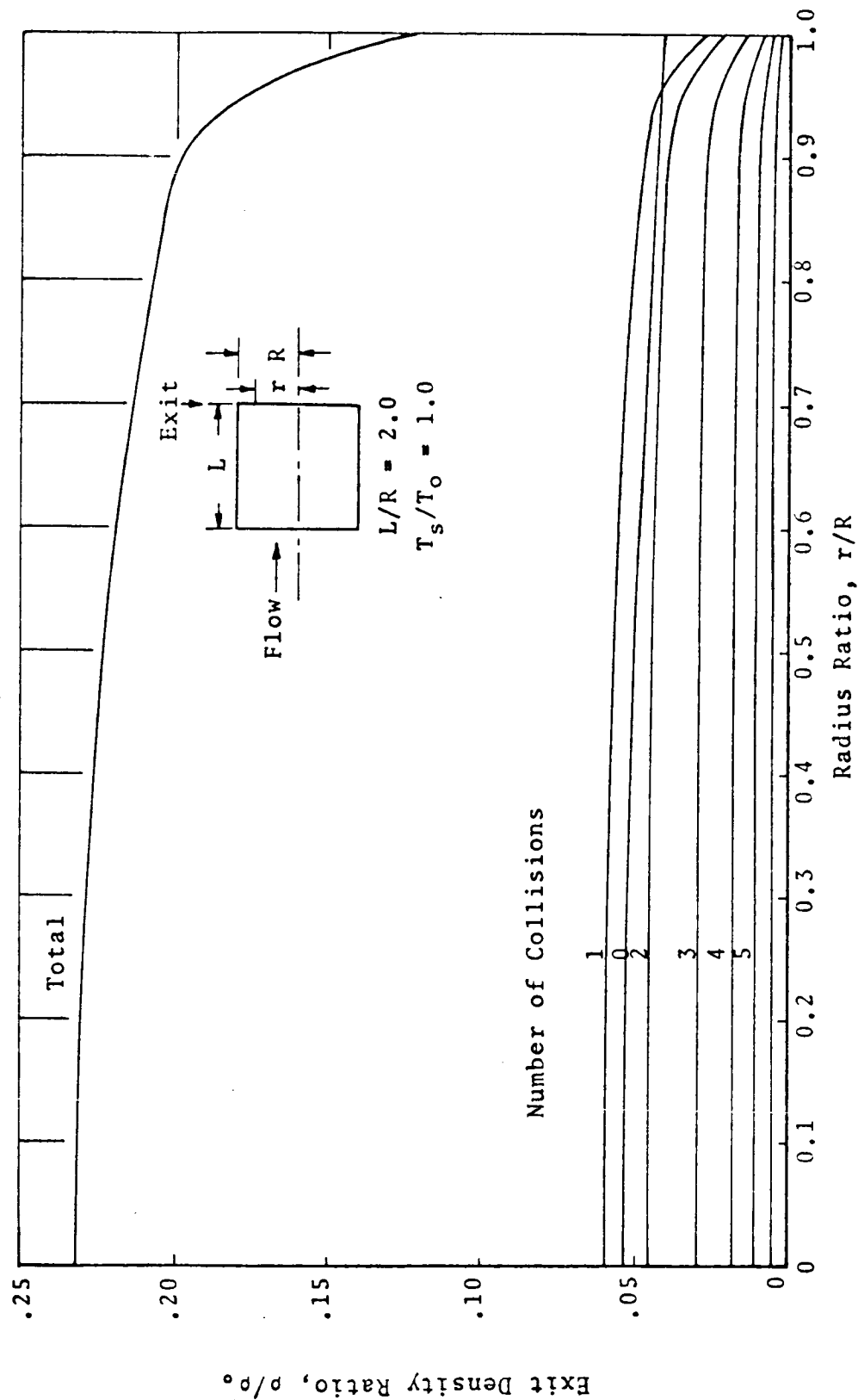
FIG. 2.1-7 EXIT VOLUME DENSITY AS A FUNCTION OF NUMBER OF COLLISIONS AND POSITION
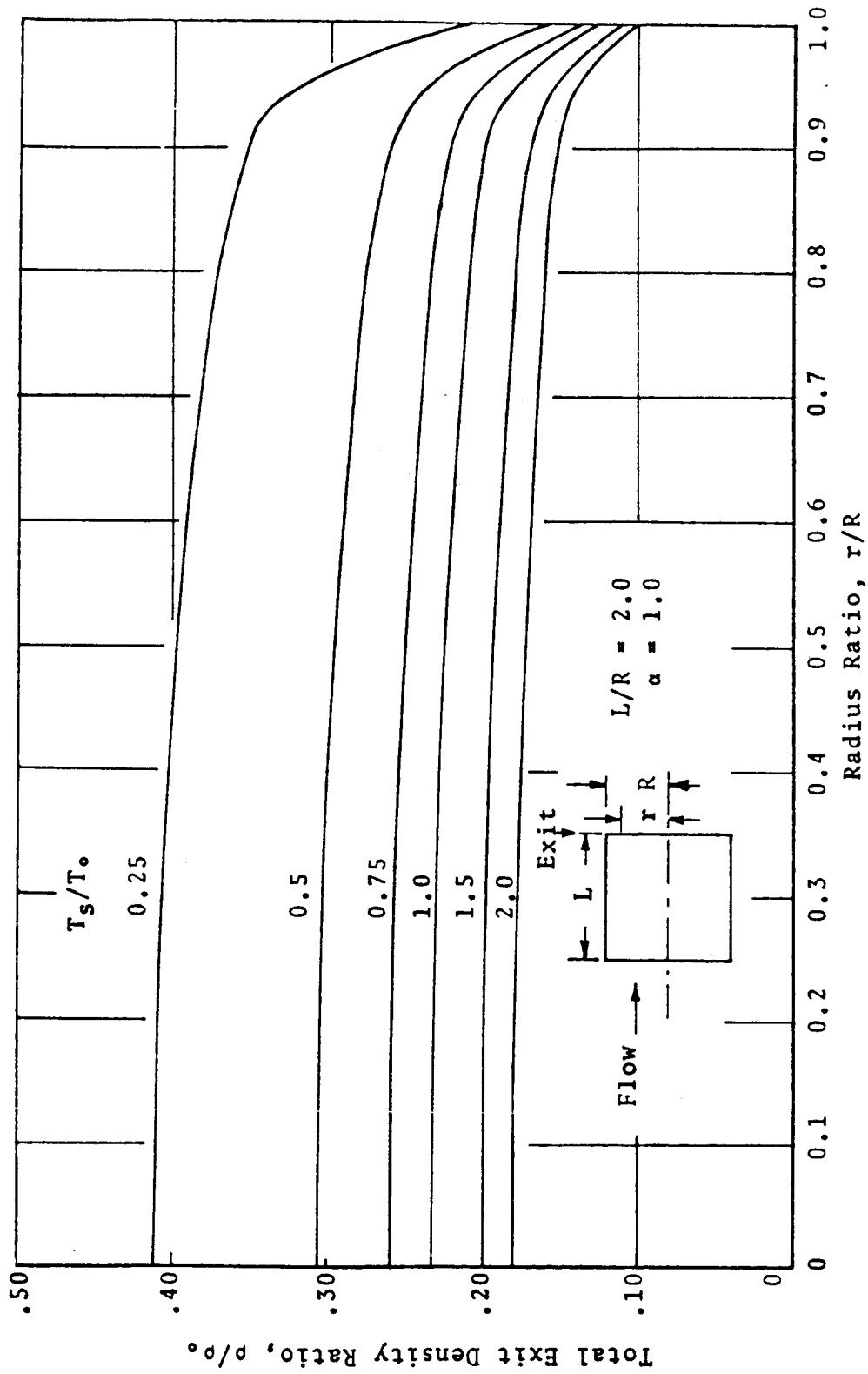
FIG. 2.1-8 TOTAL EXIT DENSITY AS A FUNCTION OF
DUCT TEMPERATURE AND POSITION
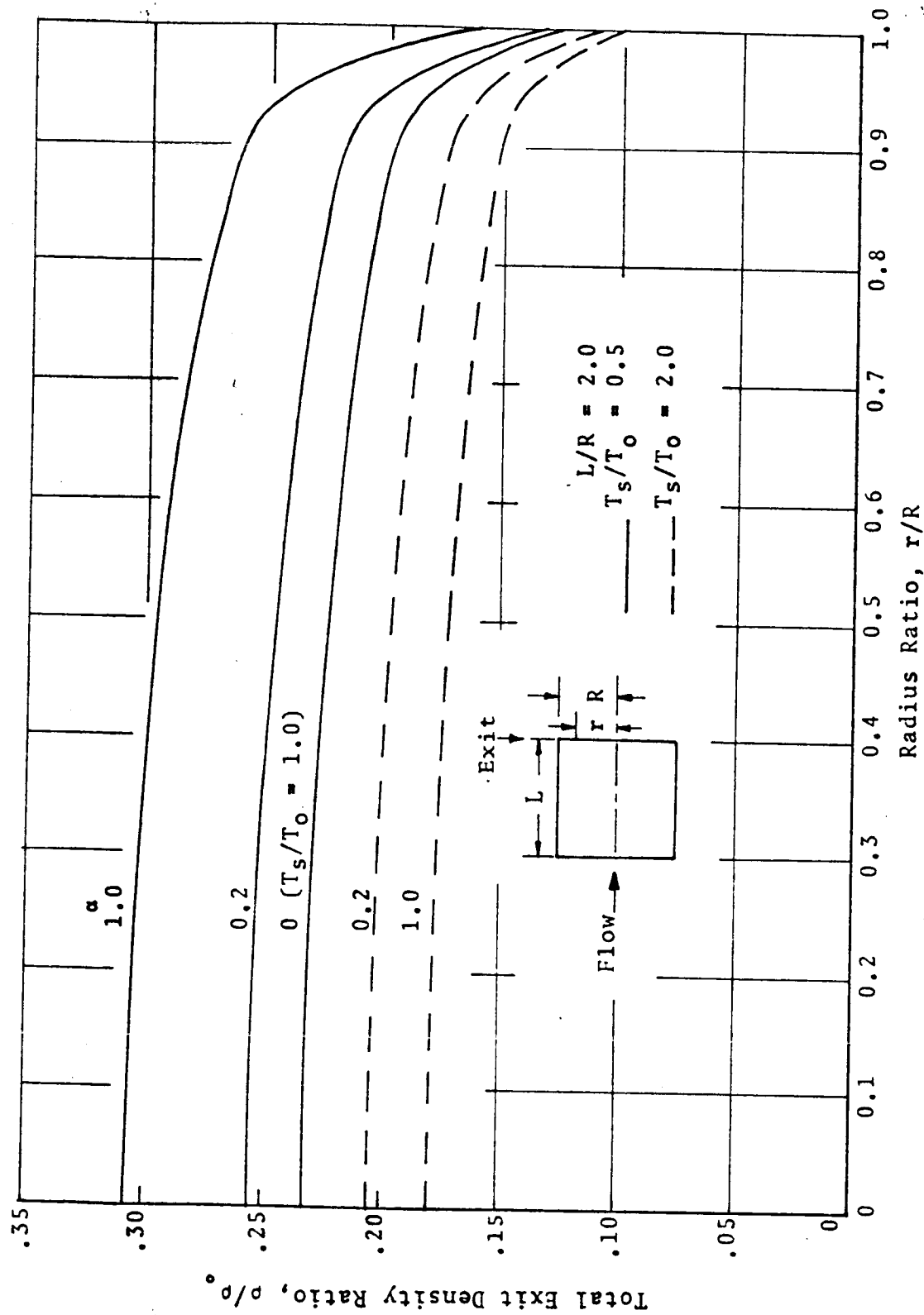
FIG. 2.1-9   VARIATION OF EXIT DENSITY DISTRIBUTION
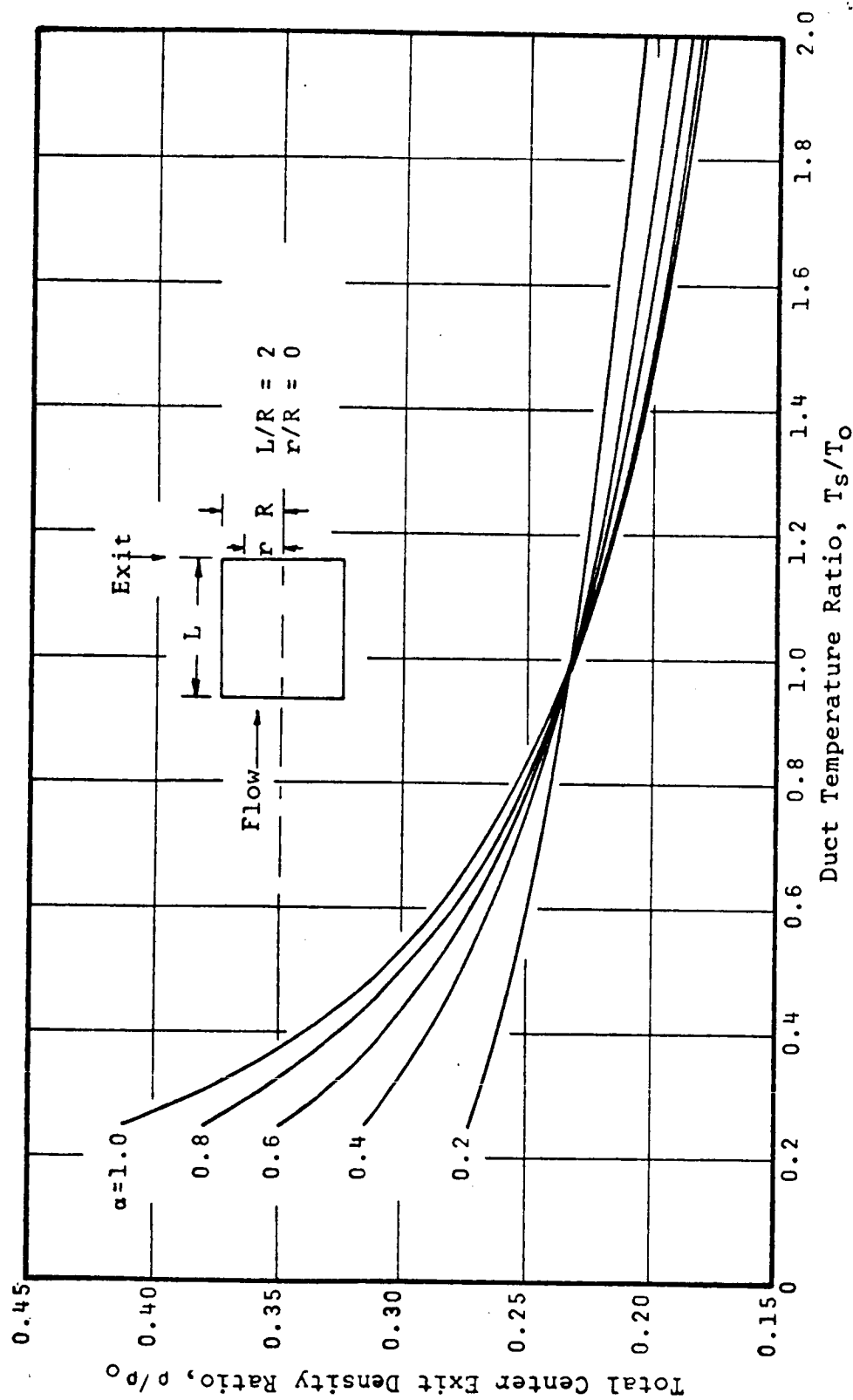WITH THERMAL ACCOMODATION COEFFICIENT

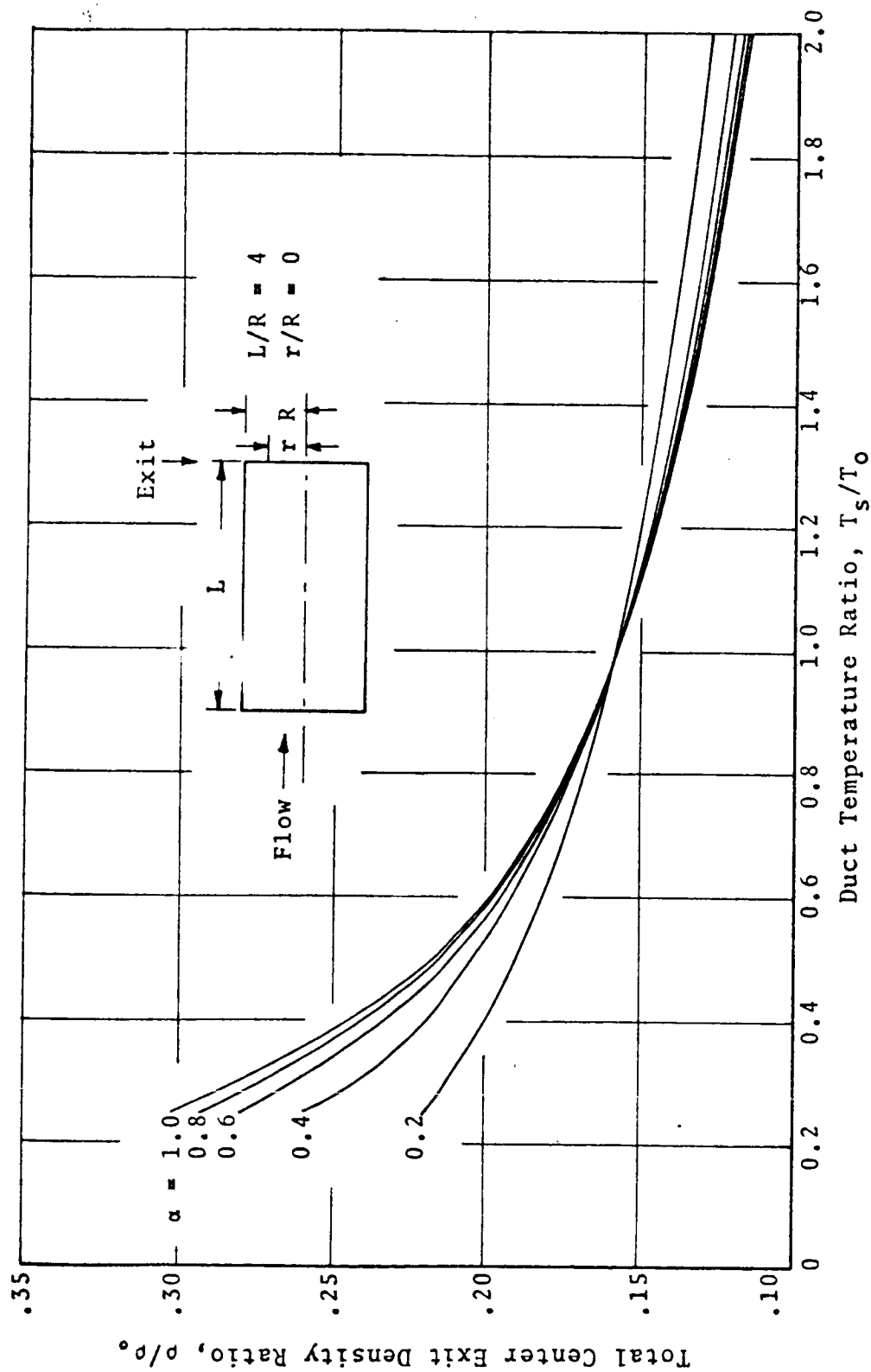FIG. 2.1-10 VARIATION OF CENTER EXIT DENSITY WITH DUCT TEMPERATURE AND THERMAL ACCOMODATION COEFFICIENT

FIG. 2.1-11   VARIATION OF CENTER EXIT DENSITY WITH DUCT TEMPERATURE
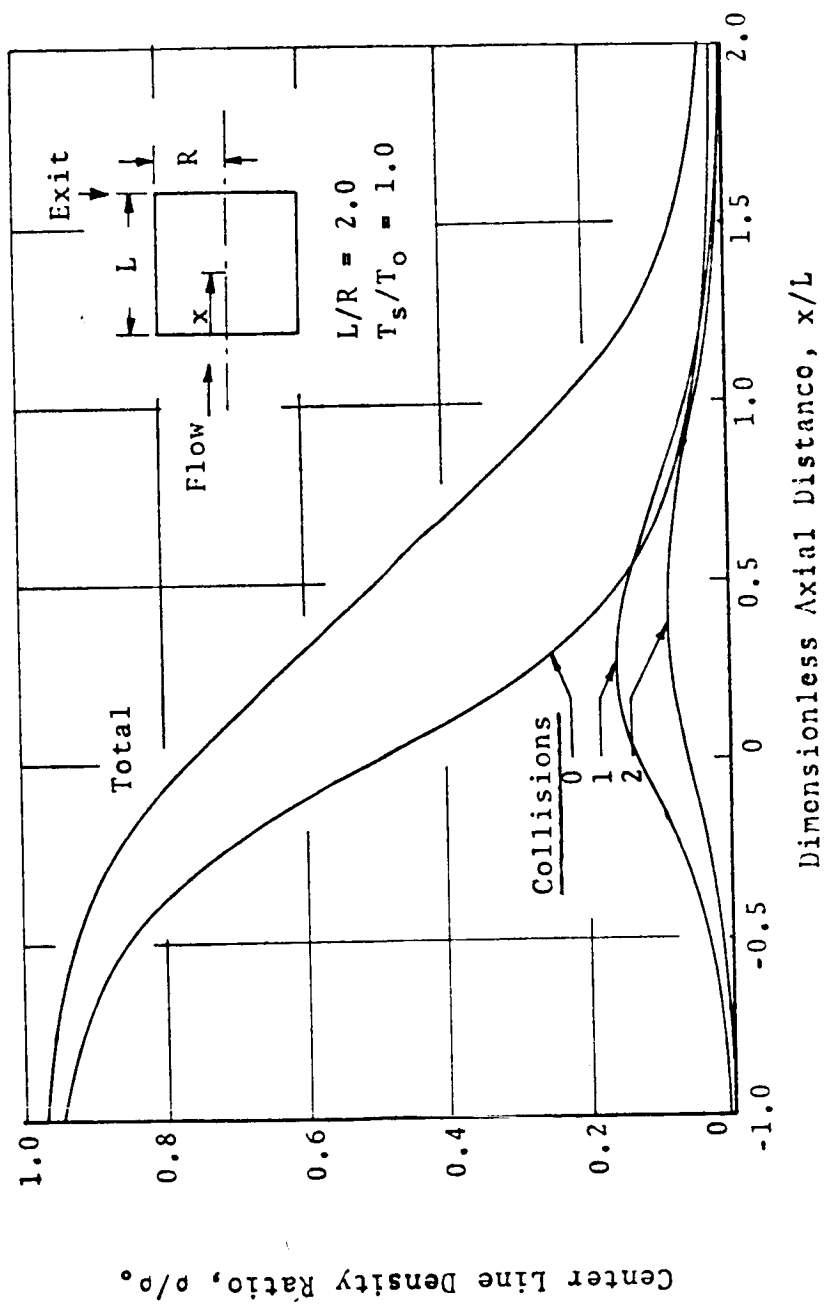AND THERMAL ACCOMODATION COEFFICIENT

Center Line Density Ratio, ρ/ρ_o

Dimensionless Axial Distance, x/L

Total

Collisions
0
1
2

Flow

Exit

R

L

$L/R = 2.0$
$T_s/T_o = 1.0$

FIG. 2.1-12 VARIATION OF CENTER LINE DENSITY DISTRIBUTION WITH NUMBER OF COLLISIONS

Total Center Line Density Ratio, ρ/ρ_o

Dimensionless Axial Distance, x/L

TS/TO
0.25
0.5
0.75
1.0
1.5
2.0
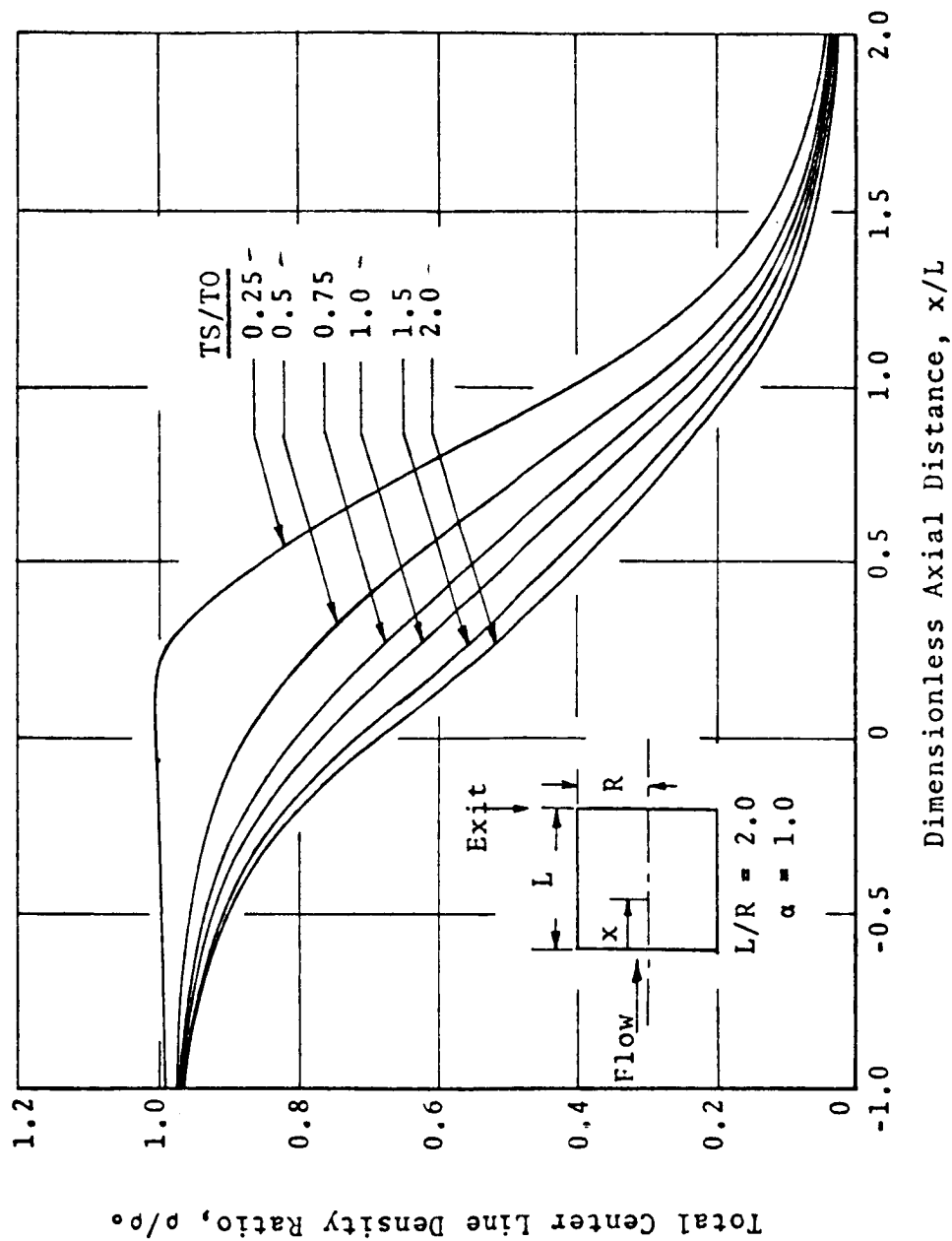
L/R = 2.0
α = 1.0

Flow

Exit

L

R

x

FIG. 2.1-13   VARIATION OF CENTER LINE DENSITY DISTRIBUTION
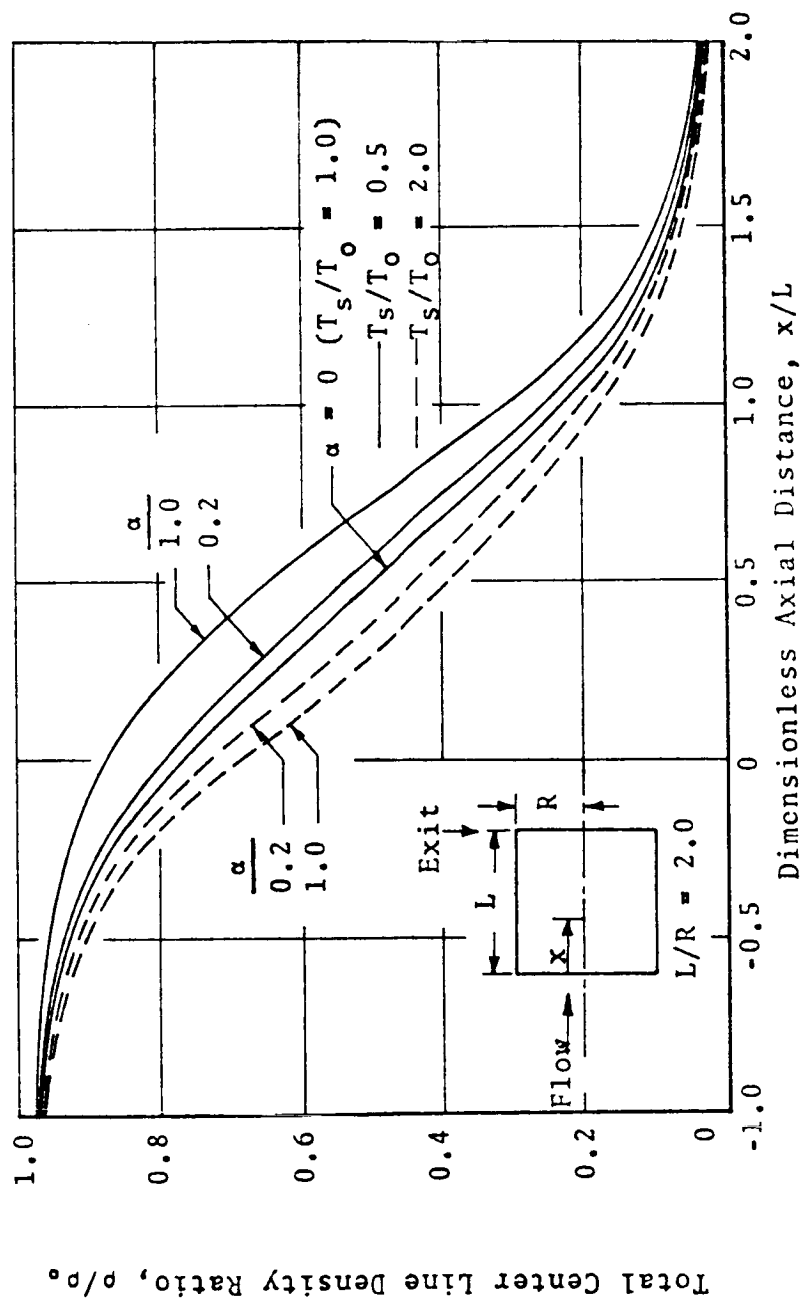WITH DUCT TEMPERATURE

FIG. 2.1-14 VARIATION OF CENTER DENSITY DISTRIBUTION WITH THERMAL ACCOMODATION COEFFICIENT

2.2 STUDY OF A BALLOON RECOVERY TECHNIQUE FOR THE S-IB

2.2.1 Introduction

In recent years the idea of booster recovery has increased in popularity because of the cost of fabricating a large-thrust vehicle. Concepts that could be used for recovery have been under study for an equal length of time and some recovery ideas now appear more feasible than others. Recently, the Boeing Aircraft Company submitted a report of booster recovery schemes to the Marshall Space Flight Center. One of these schemes warranted further study to verify that a booster could be recovered by a system as simple as that proposed. This system was to simply attach a balloon large enough to supply the necessary buoyancy for the S-IB at a fixed altitude of five thousand feet above sea level; the balloon would be inflated when the booster reached its apogee, and its pressure constantly increased through its descending flight to meet the constantly increasing ambient pressure.

2.2.2 Statement of Problem

Recovery of a booster by a balloon supplying a buoyant force presents many problems. Considering a case where a balloon is deployed at the apogee of a spent booster's trajectory involves problems in dynamics, thermodynamics and

aerodynamic heating.

The dynamics define the trajectory which is so important to the aerodynamic heating and also the total pressure history that is seen by the balloon. The thermodynamic problem consists of supplying sufficient gas to the balloon to meet the minimum pressure requirements so that the balloon will remain spherical; the wall temperature of the balloon is affected by the aerodynamic heating and the temperature history of the gas enclosed within the balloon. In either of the areas, i.e., dynamics, the thermodynamics or aerodynamic heating, the solutions should be made simultaneously.

The specific problem was to: define a trend in the wall temperature of a balloon, predict the total amount of pressurizing gas required, and calculate the variable flow rates of the pressurizing gas required to maintain a pressure within the balloon equal to the external total pressure.

The information given to HTL was the weight of the spent SI-B with all the necessary balloon attachments (Ref. 2.2-1), the diameter of the balloon, and a trajectory. It was indicated that a three-mill mylar wall would be used to entrap the hydrogen pressurizing gas. With this information the study was intiated.

2.2.3 Method of Solution

It was necessary first to calculate the aerodynamic

heating on the balloon and its effects on the pressurization system. The theory of Van Driest, (Ref. 2.2-1), was used to calculate the turbulent heat transfer coefficient, with Eckert's reference enthalpy accounting for compressibility as in Ref. 2.2-2.

The heat transfer to the balloon was treated as a thin wall with finite capacitance. Internally, a film coefficient of 9.0 BTU/hr ft^2 °R was used; this is an average coefficient determined by tests in the ullage regime of hydrogen propellant tanks as shown in Ref. 2.2-3 and -4. The heat transfer through the wall was included in the thermo-dynamic analysis of the pressurization system. This analysis assumed that the gas had an infinite thermal conductivity and that the pressurizating gas entered the balloon at a constant temperature. The flow rate into the balloon was such that the static pressure history in the balloon was the same as the dynamic pressure history outside. All thermal properties were temperature dependent.

The pressurizing gas inlet temperature was the pri-mary parameter in this study. It was selected as such because of its appreciable effect on the final gas weight the pressurizing gas flow rate, and the wall temperature. Throughout this study it was assumed that the variation of density in the balloon as caused by the temperature of the gas had negligible effects on the trajectory.

2.2.4 Discussion of Results

Fig. 2.2-1 shows the film coefficient of heat trans-fer as calculated for a flat plate approximately one hundred

feet long. Fig. 2.2-2 shows the recover temperature history for turbulent flow using $(Pr)^{1/3}$, or 0.88. Fig. 2.2-3 is the thin-skin wall temperature at approximately one hundred feet from the stagnation point. It should be emphasized that these values are to be used as trends and not quantitative values of skin temperature. Although Van Driest's theory is for a flat plate with no pressure gradient normal to the flow it is expected that the temperature are representative of at least the direction: the magnitude of the predicted temperatures should be close if they are con- sidered to represent temperatures ninety degrees from the stagnation point. The total incident heat on the balloon is therefore taken as the product of the film coefficient and the difference in recovery and wall temperature, as shown in Fig. 2.2-4 . It can be seen in Fig. 2.2-4 that the direction of heat transfer is dependent upon the pressurizing gas temperature after the vehicle has decelerated to below Mach 1 at 105 seconds. A close analysis of this figure also reveals that the balloon is not in thermal equilibrium with it environment when the 5000-foot altitude is reached. The case of a 500°F pressurizing gas seems to be the closest to thermal equilibrium. With the ex- ception of the 500 and 810°F pressurizing gas inlet con- ditions, it will be necessary to vent gaseous hydrogen as the gas receives heat from the 5000-foot environment. The 500 °R case should require very little gas, if any, and the 810 °R case will require a large amount as the

density of the gas increases due to cooling. The temperature history of gas entrapped in the balloon is shown in Fig. 2.2-5 . The flow rates of pressurizing gas are shown in Fig. 2.2-6 . The total amount of pressurizing gas required up to 650 seconds of flight is shown in Fig. 2.2-7 . Fig. 2.2-8 shows how the total weight (total for 650 second only) varies with pressurizing gas inlet temperature. As the final gas weight decreases the requirements for heating the hydrogen to a higher temperature calls for a bigger heat exchanger. Also, the weight of the plumbing system for carrying the lower density gas increases with increasing gas inlet temperature requirements. This is shown qualitativly in Fig. 2.2-9 .

The flow field would definitely affect the temperature of the wall and gas, but because of restricted time and man-power requirements, free stream properties upstream of the booster were used to calculate heat transfer. The properties were taken from the US Standard Atmosphere, 1962 tables.

2.2.5 Conclusions and Recommendations

By using the available trajectory it can be concluded that temperatures and pressurization requirements are within reason, and preliminary indications are that the balloon concept is workable.

Further study must be made in these areas: A, defining the flow field about the system, B, determining the

pressure distribution about the balloon, C, performing an optimization study to determine the optimum gas inlet temperature, D, studying the effects of temperature gradients in the balloon due to the uneven heat input to the balloon's spherical surface, E, the heat exchanger design, and, F, the source of heat for boiling-off the liquid hydrogen.

A factor that must be given more consideration is the actual shape of the balloon through flight and its effect on the trajectory. Pressure distributions over an' elastic body, which is initially spherical, must be considered so that the proper drag coefficient would be used to accurately determine the trajectory.

2.2.6 References

2.2-1. Van Driest, E. R., "Turbulent Boundary Layer in Compressible Fluids" Journal of the Aeronautical Sciences, March "51, pp. 145-160 and pg. 216.

-2. Eckert, E. R. G., "Engineering Relations for Heat Transfer and Friction in High-Velocity Laminar and Turbulent Boundary-Layer Flow θver Surfaces with Constant Pressure and Temperature", Transactions of the ASME, August '56, pp 1273-83.

-3. "Main Propellant Tank Pressurization System Study and Test Program", Vols. I & III, Lockheed-Georgia Company, ER-5296, December '61.

-4. Datis, Angelo, Usher, L. H., "Final Gas Temperature in Missile Propellant Tanks", Space/Aeronautics August '62, pp 159-63.
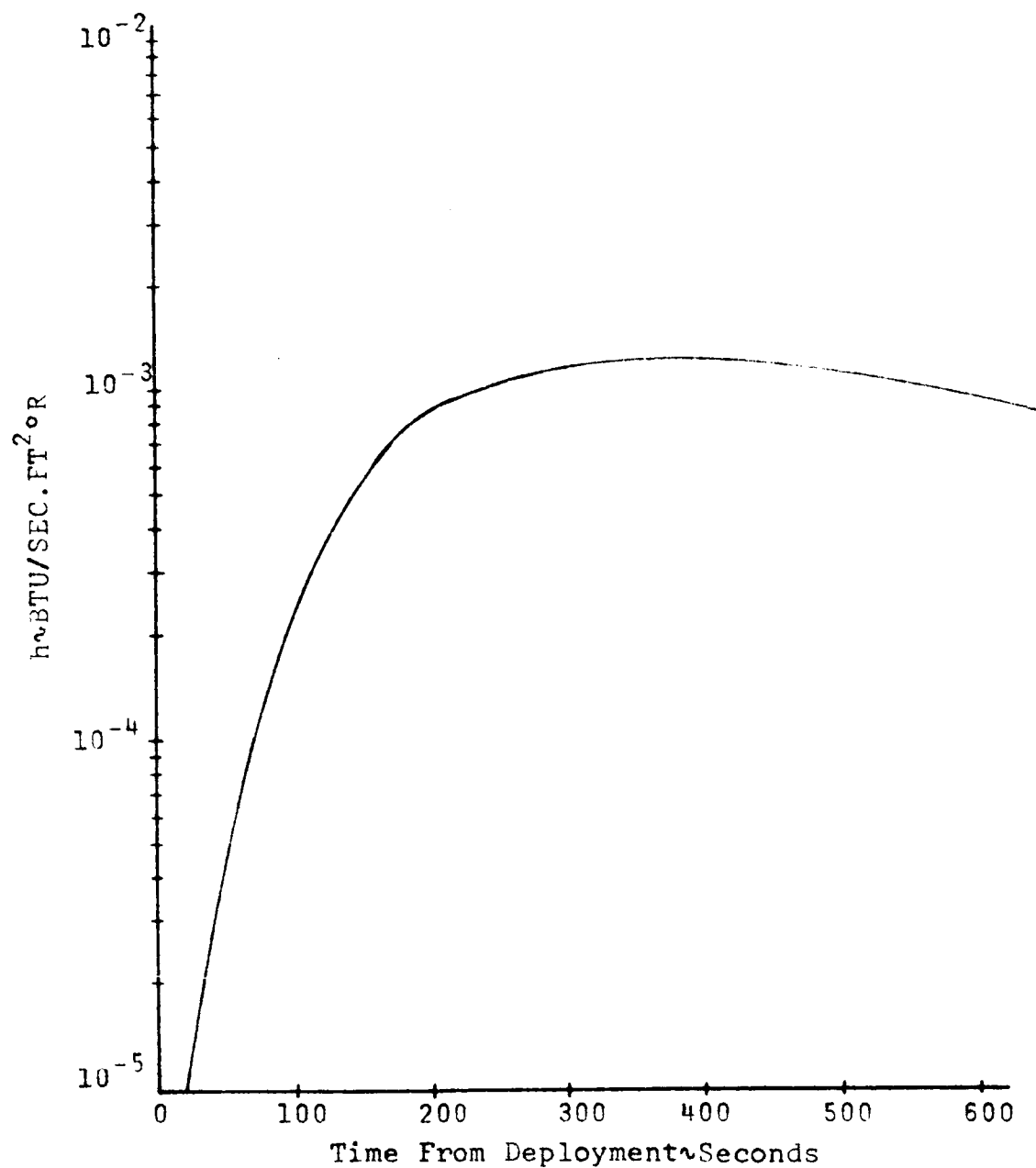
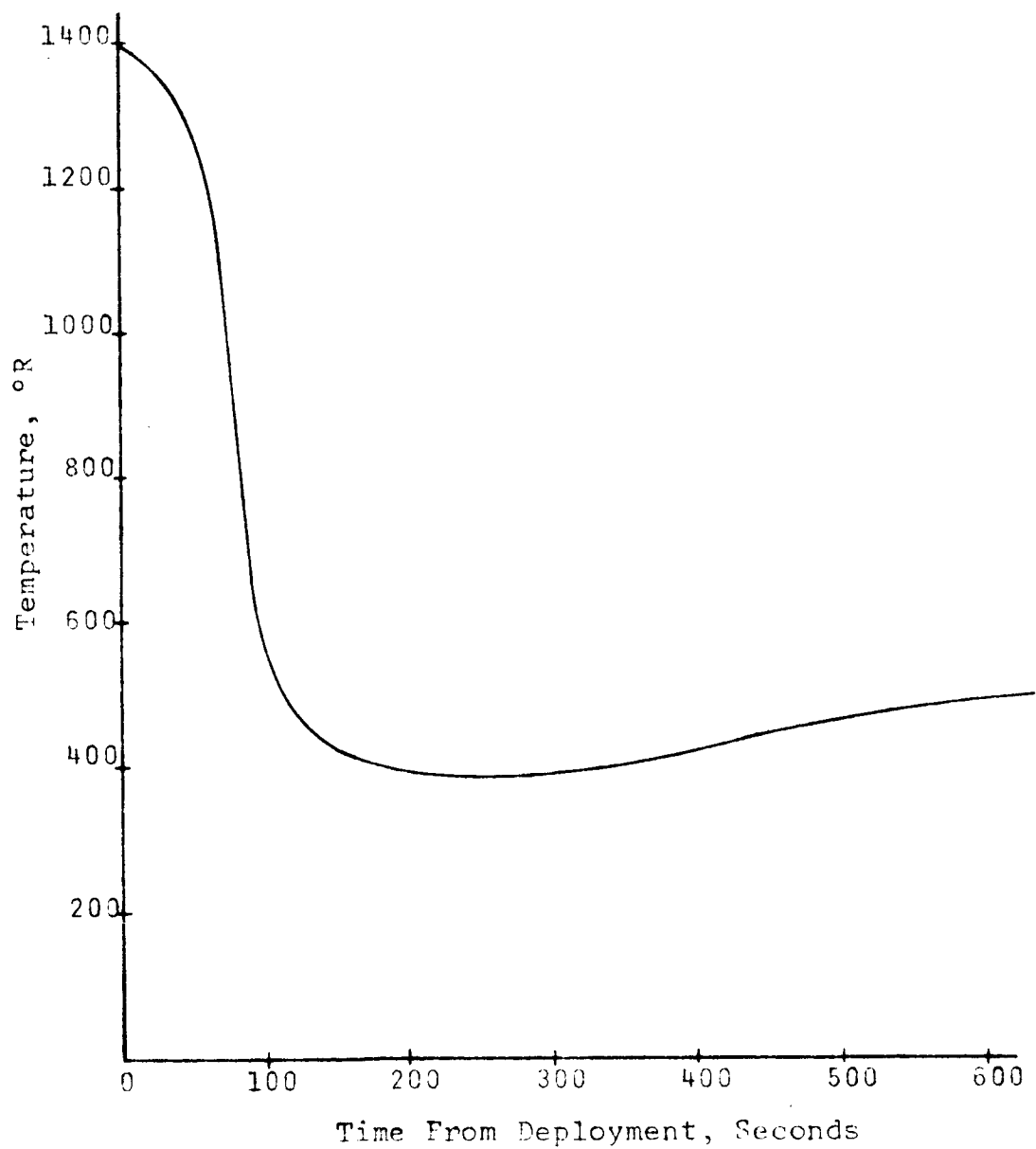FIG. 2.2-1 FLAT PLATE TURBULENT COEFFICIENT OF HEAT TRANSFER
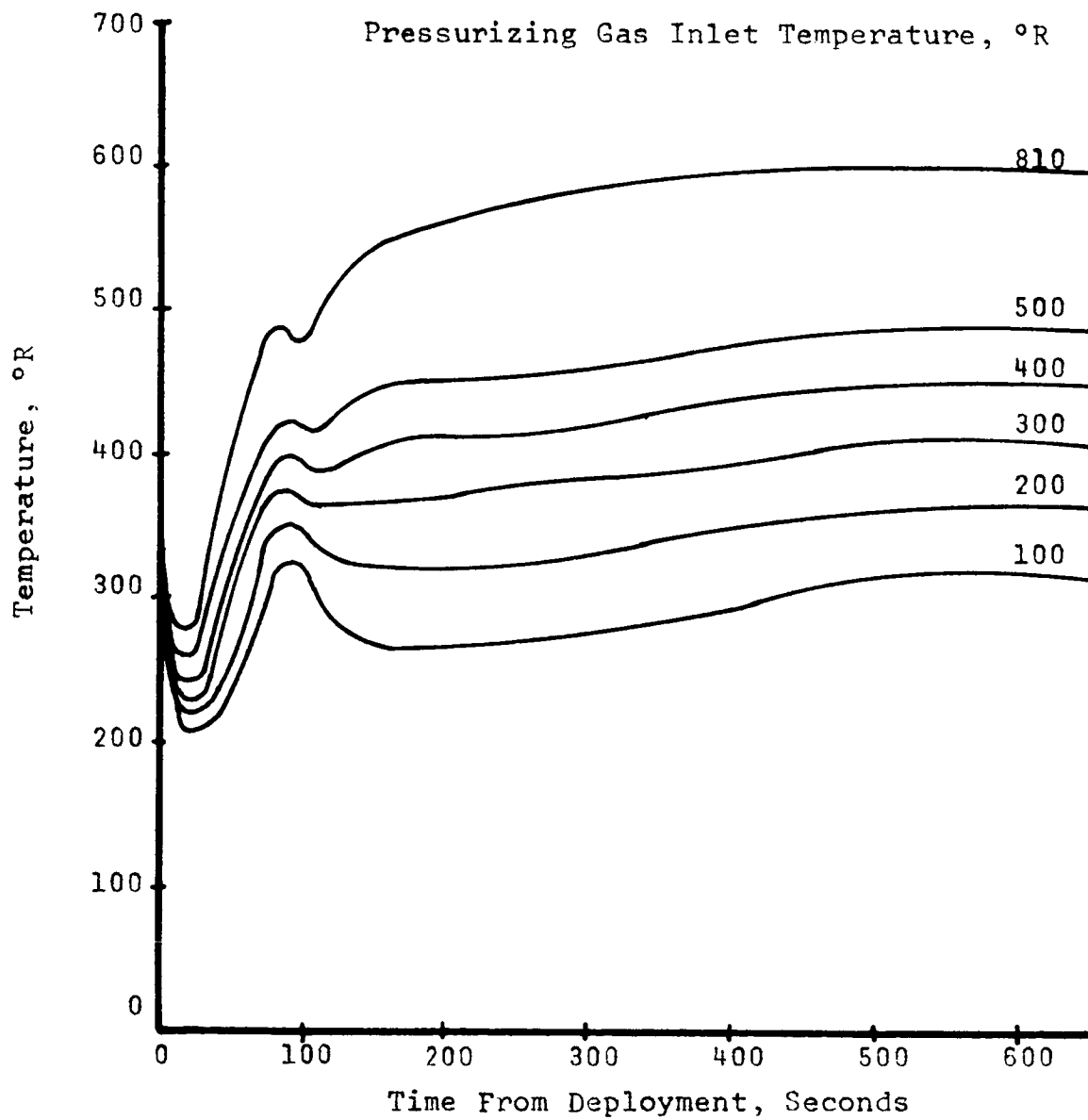
FIG. 2.2-2 RECOVERY TEMPERATURE HISTORY

Pressurizing Gas Inlet Temperature, °R

FIG.   2.2-3   WALL TEMPERATURE HISTORY

FIG. 2.2-4 WALL HEAT FLUX HISTORY

PRESSURIZING GAS INLET TEMPERATURES, °R
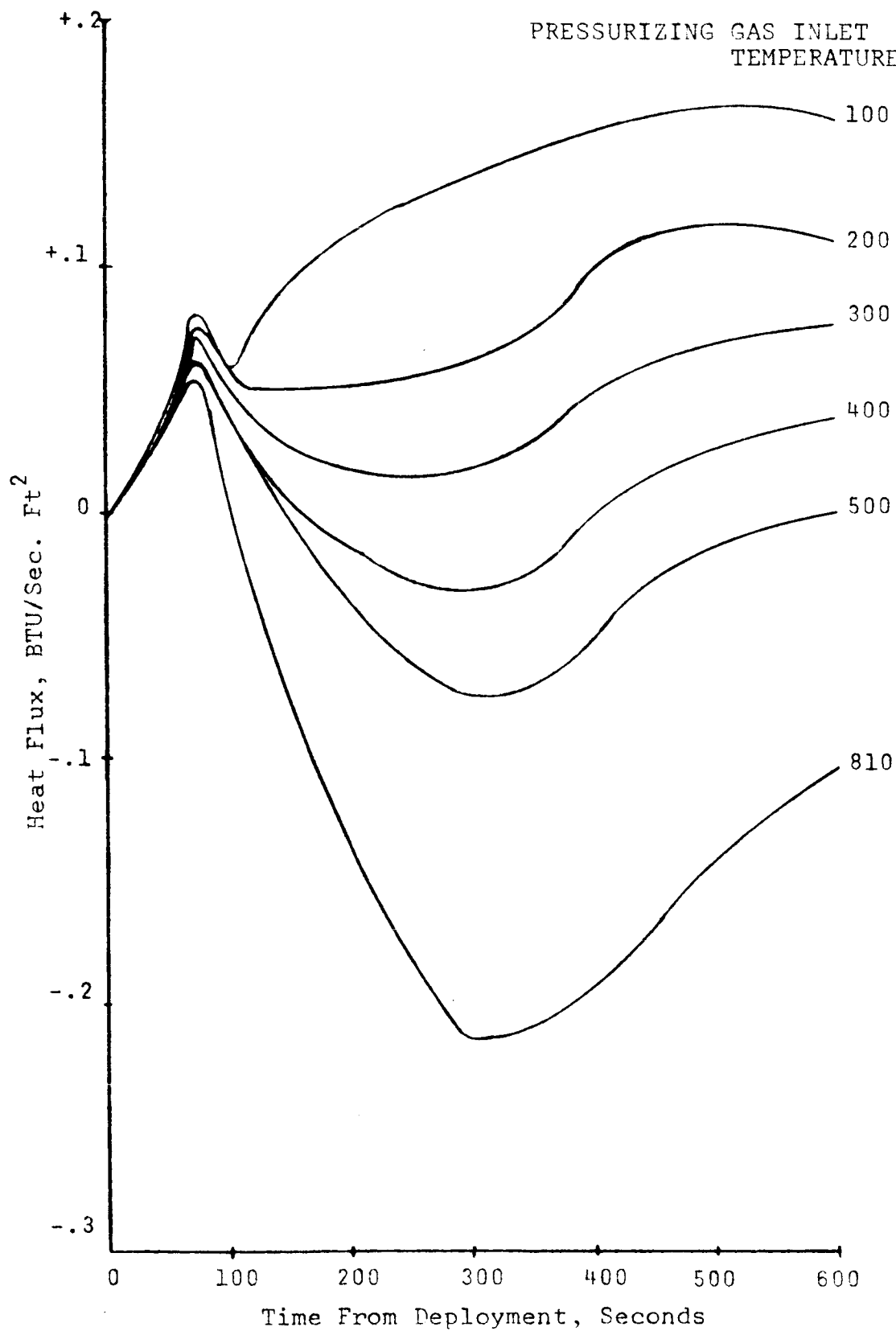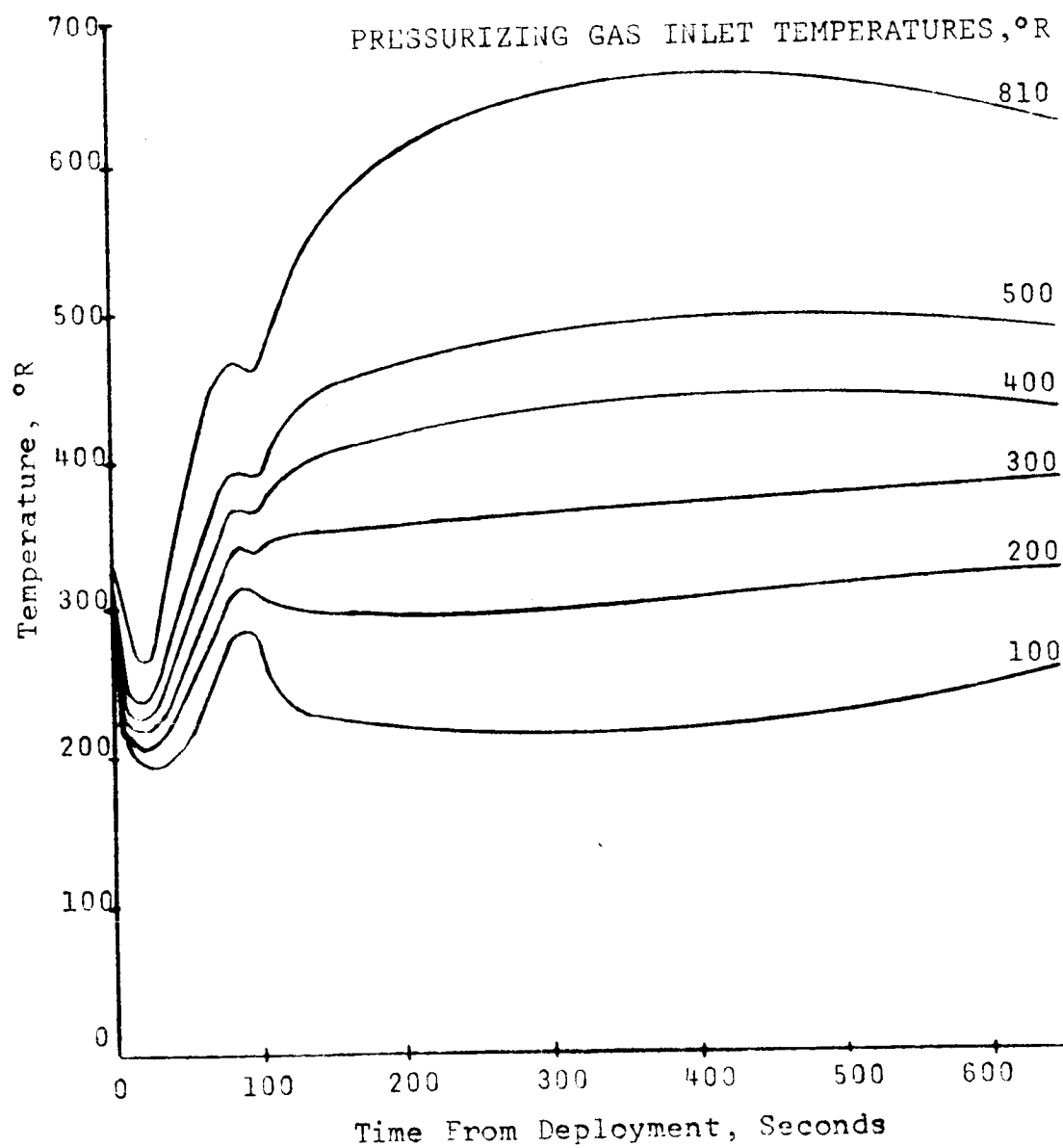
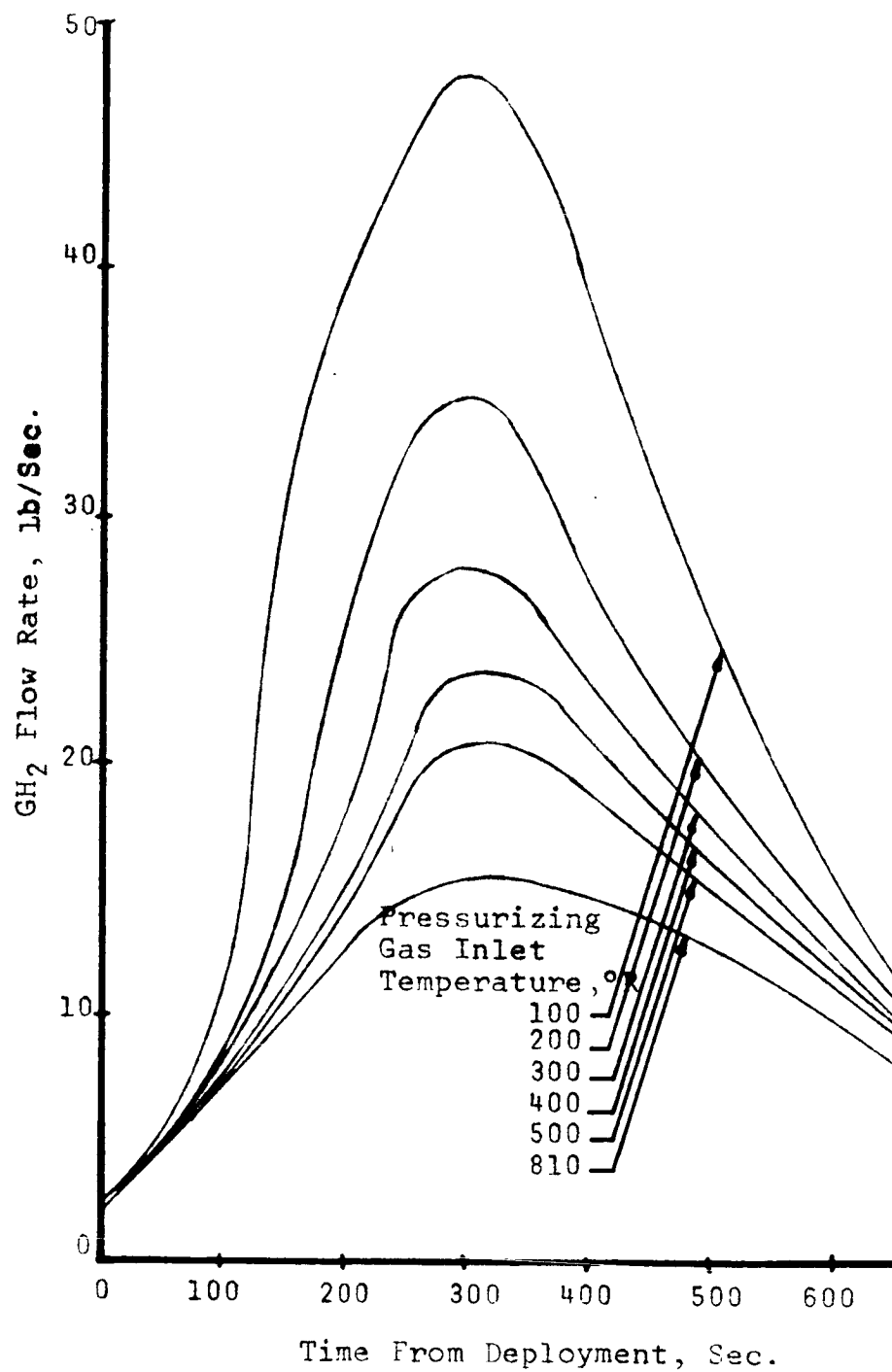FIG. 2.2-5 BALLOON GAS TEMPERATURE HISTORY FOR COMPLETELY MIXED GAS

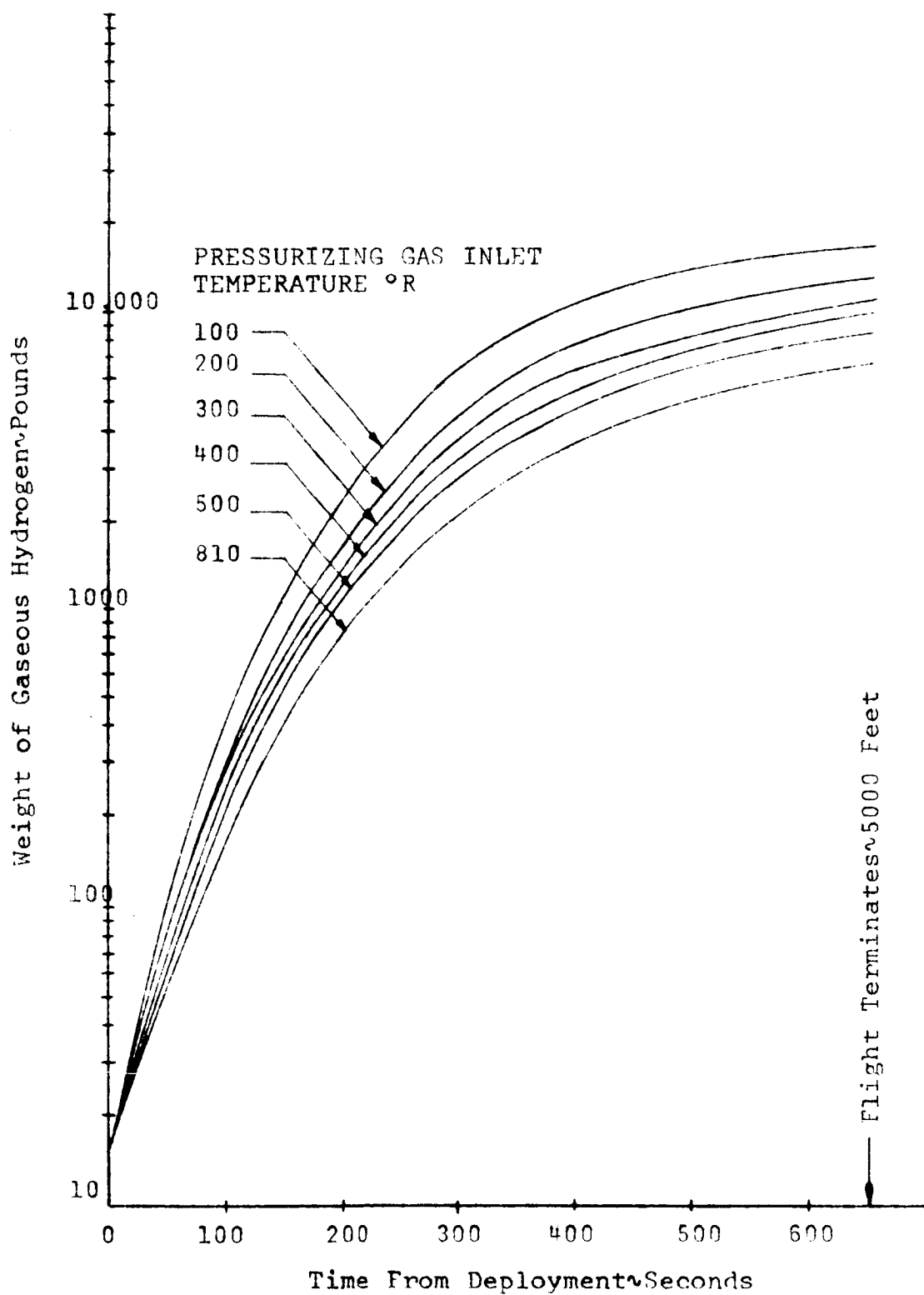FIG. 2.2-6 PRESSURIZING GAS FLOW RATE HISTORY
AT VARIOUS
GAS INLET TEMPERATURES

FIG. 2.2-7 HISTORY OF WEIGHT OF GAS IN BALLOON AT VARIOUS
PRESSURIZING GAS INLET TEMPERATURES
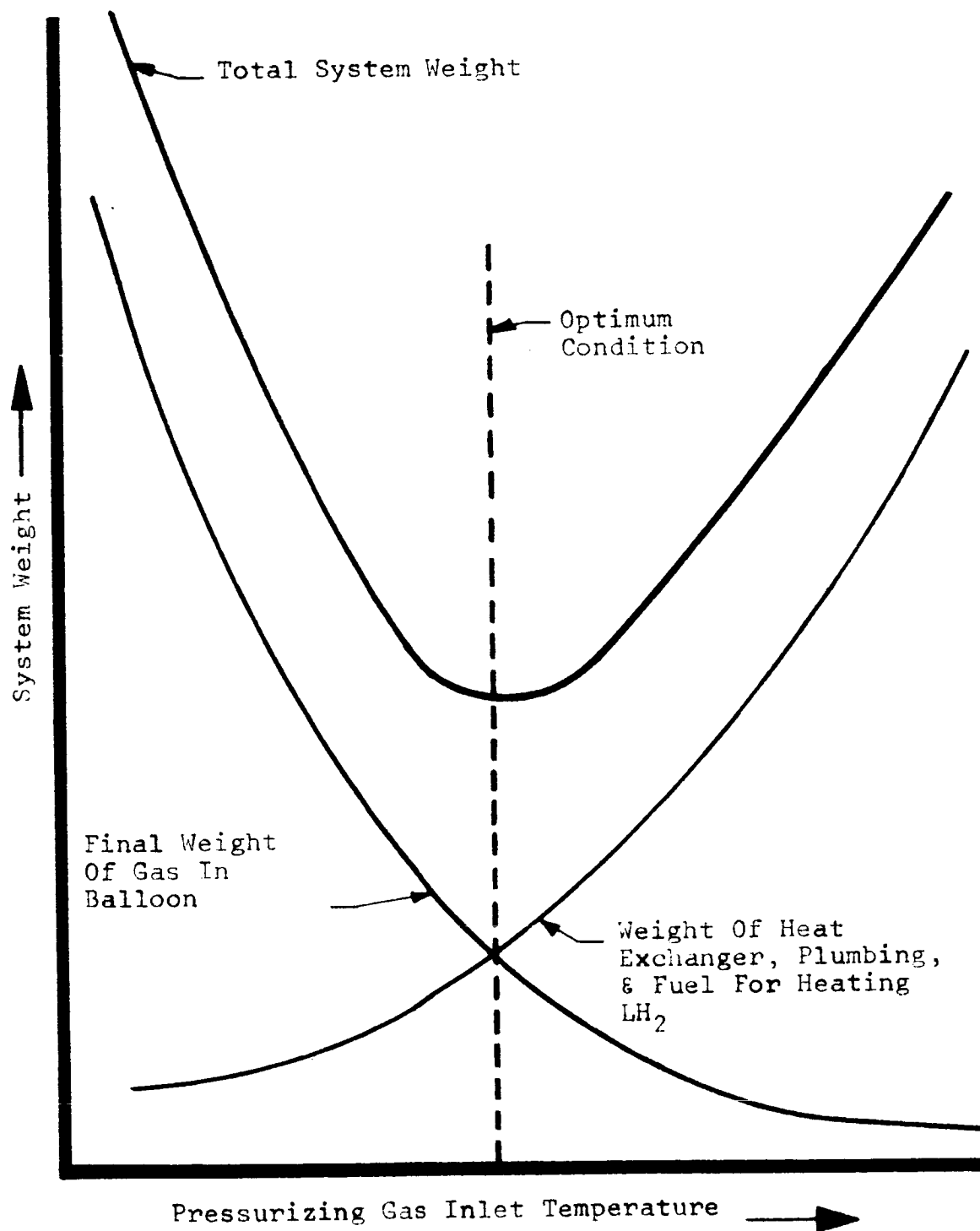
FIG. 2.2-9 DIRECTIONS OF WEIGHT TRADE OFF FOR LH_2 SYSTEM

Time=650 Seconds After Deployment
Altitude-5000 Feet Above Sea Level
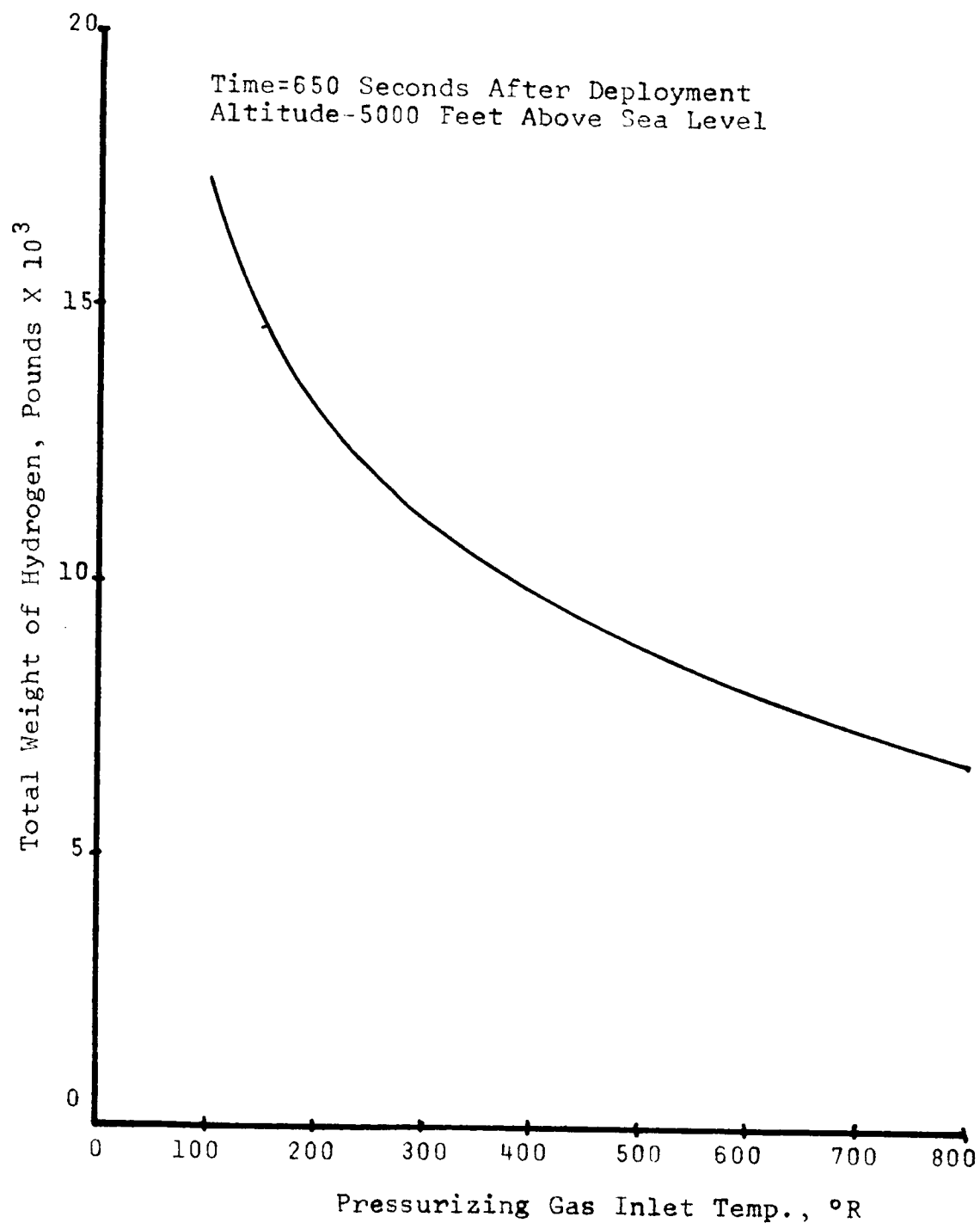
Total Weight of Hydrogen, Pounds X 10^3 (y-axis)

Pressurizing Gas Inlet Temp., °R (x-axis)

FIG. 2.2-8

FINAL GAS WEIGHT IN BALLOON
VS
PRESSURIZING GAS INLET TEMPERATURE

2.3 FEASIBILITY OF TWO-DIMENSIONAL BASE FLOW STUDIES

2.3.1. Introduction

Since the initial proposal of two-dimensional base flow study by HTL (Ref. 2.3-1), several preliminary invest-igations were conducted to further establish the feasibi-lity of such studies. Investigations have been made to determine the possibility of utilizing convenient existing facilities (Ref. 2.3-2), and to estimate boundary layer effects within a typical two-dimensional nozzle (Ref. 2.3-3). Additional studies defining the test objectives, the test methods, and measurement techniques are currently in progress. The literature survey is also being continued.

2.3.2 Objectives of the Proposed Tests

The objectives of the tests were tentatively defined to be the details of the flow associated with mutual two-dimensional jet impingement. Specifically, the following aspects of the flow would be considered.

1. Details of Reverse Flow.

2. Effect of Turbine Exhaust Discharge on Reverse Flow.

3. Measure of the Relaxation Process in the Nozzle.

4. Measure of Kinetics in a "Correctly" Simulated Turbulent Field.

5. Measure of Two-Dimensional Eddy Viscosity.
Although the objectives of the tests listed above as items
3, 4, and 5 are of special importance, improvements in the
present state-of-the-art in measurement techniques and in-
strumentation may be necessitated by such tests. Further
investigation of measurement techniques and instrumentation
required to accomplish these measurements in continuing.
Experimental data on the details of reverse flow are also
lacking and are of utmost importance. A general discussion
of the parameters that influence the reverse flow is pre-
sented with the results of certain cursory analyses that
have been conducted.

If a line of symmetry is drawn through the intersect-
ion of the impinging jets as shown in Fig. 2.3-1, flow re-
sembling a jet impinging upon a flat plate would result.
Utilizing a one-dimensional analysis, the maximum turning
angle for a given Mach number can be obtained. Thus, an
estimate of the relationship between the impinging Mach
numbers, flow angle, and consequent reverse flow is indicat-
ed by Fig. 2.1-2. In the above analysis the effect of the
impinging gas specific heat ratio can also be estimated. As
shown in Fig. 2.3-2, the specific heat ratio has a distinct
effect upon the posibility of reverse flow.

Familiarization studies were made of the work on
base pressure theories by two of the most prominent in-
vestigators, Chapman (laminar wake) and Korst (turbulent
wake). These familiarization studies have revealed that
the presently available methods for predicting base pres-

sure are not entirely adaquate. The methods of estimating the base pressure do not consider the effect of the boundary layer on the mixing region and the subsequent effect on the base pressure. Since reliable predictions, where boundary layer effects are important, cannot be made with the currently available theory, two-dimensional base studies may be desirable. Hopefully, a two-dimensional study of the boundary layer effects could be made. Indications are, from recent two-dimensional nozzle studies conducted at HTL, that the boundary layer can be controlled withint the nozzle. The three known methods by which boundary layer thickness may be controlled are by the use of boundary layer suction, wall cooling techniques and chamber pressure. The potential of the boundary layer suction in control of the boundary layer would have to be determined by experiment. Thus use of nozzle wall cooling techniques has been investigated for laminar flow. Calculations were based upon the methods of Ref. 2.3-4 which were simplified for the two-dimensional case. An estimate of the effect of the wall cooling in comparison to the adiabatic is indicated by Fig. 2.3-3. Another effective method for controlling the boundary layer thickness would be through variation of chamber pressure since the boundary layer thickness is proportional to $l/(Re)^r$. For turbulent flow conditions, the boundary layer thickness was computed for various chamber pressures and presented in graphical form by Fig. 2.3-4. Hence, the boundary layer thickness can be readily controlled by varying chamber pressure.

Previous tests have shown that a shock wave has a definite effect on flow reversal. Particularly, a shock may cause flow reversal in the boundary layer due to the large adverse pressure gradient. Thus, mutual interaction between a shock wave and a boundary layer could lead to a flow pattern different from that which might be anticipated. Further testing would be required to establish the effect of shock interaction on the boundary layer.

2.3.3 Test Facilities Study

Final selection of a test facility has not been made, although several locations are under consideration. The low density chamber at Building 4311 MSFC was considered for the proposed two-dimensional studies due to its convenient location; however, studies have deemed that facility unsuitable. The principal objections to low density tests are:

1. Loss of two-dimensionality in the nozzle due to excessive boundary layer displacement thickness.

2. Nozzle flow may be outside the continuum flow regime.

The estimated boundary layer displacement thickness in a typical two-dimensional flow nozzle is shown in Fig. 2.3-5 for low density conditions. Obviously, the large displacement thickness would be detrimental to the required two-dimensional flow. Also, since it was desired to maintain the nozzle in the continuum flow regime defined by $\frac{\sqrt{Re_x}}{M} \geqslant 100$ it would be necessary to operate at a higher chamber pres-

sure than deemed feasible at the Building 4311 facility.

2.3.4 References

2.3-1. Jones, D. L. and Farmer, R. C., "Proposed Two-dimensional Base Flow Studies Under Existing Contract NAS8-11558," HTL Internal Memorandum, April 21, 1964.

-2. HTL Memo No. 29, "Discussion of Short Duration Flow Facility, " July 4, 1964.

-3. Unpublished HTL Memo, "Discussion of Feasibility of Using the Low Density Chamber at Building 4311 MSFC for Two-Dimensional Base Flow Studies."

-4. Durand, J. A. and Potter, I. C., "Calculation of Thickness of Laminar Boundary Layers in Axisymmetric Nozzles with Low-Density, Hypersonic Flow," AEDC-TN-61-146, Dec. 1961.

Jet
Plume

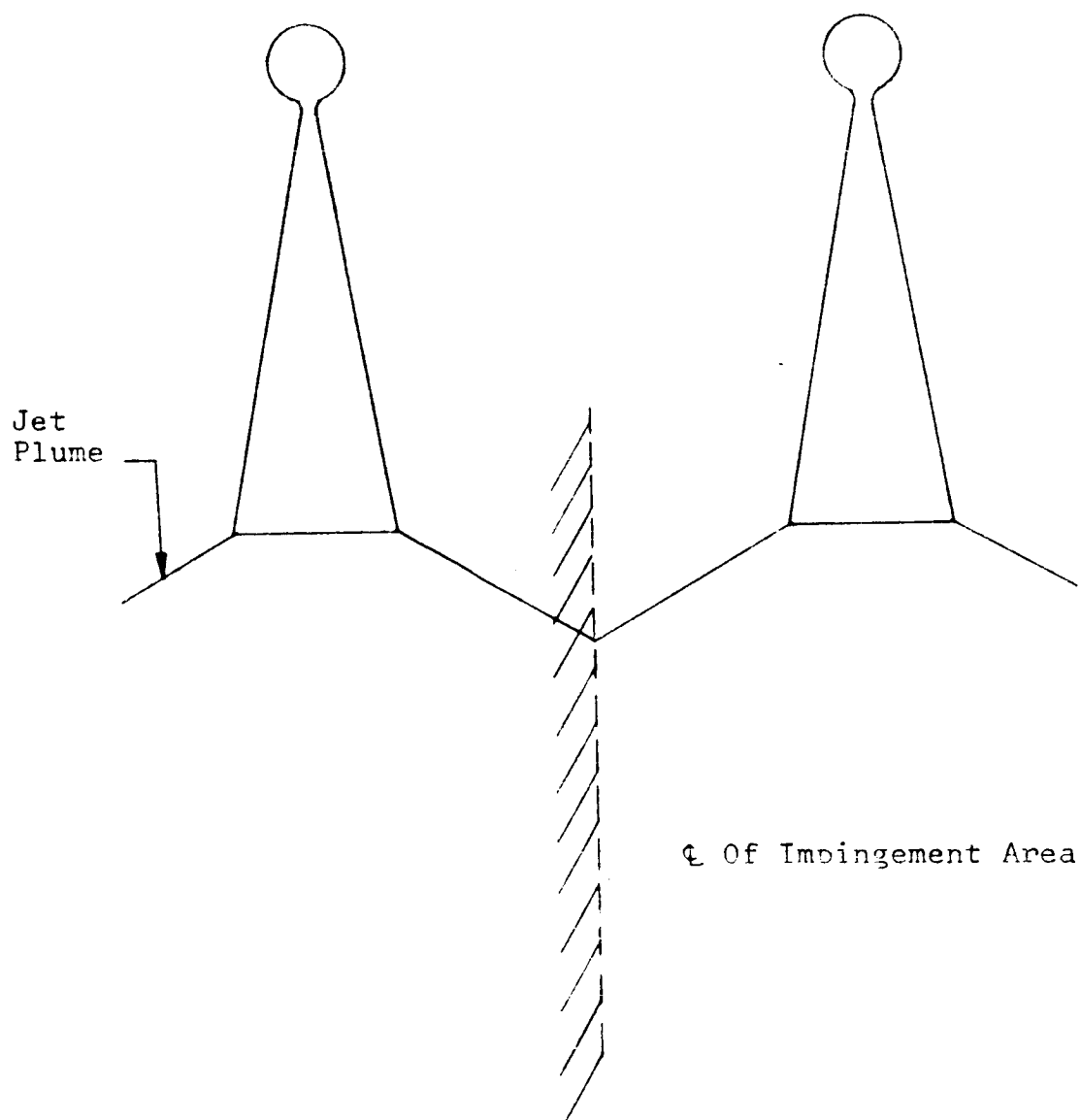$\bar{\text{C}}$ Of Impingement Area

FIG. 2.3-1 APPROXIMATE ANALYTICAL MODEL FOR DETERMINING
REVERSE FLOW OF THE SUPERSONIC STREAM
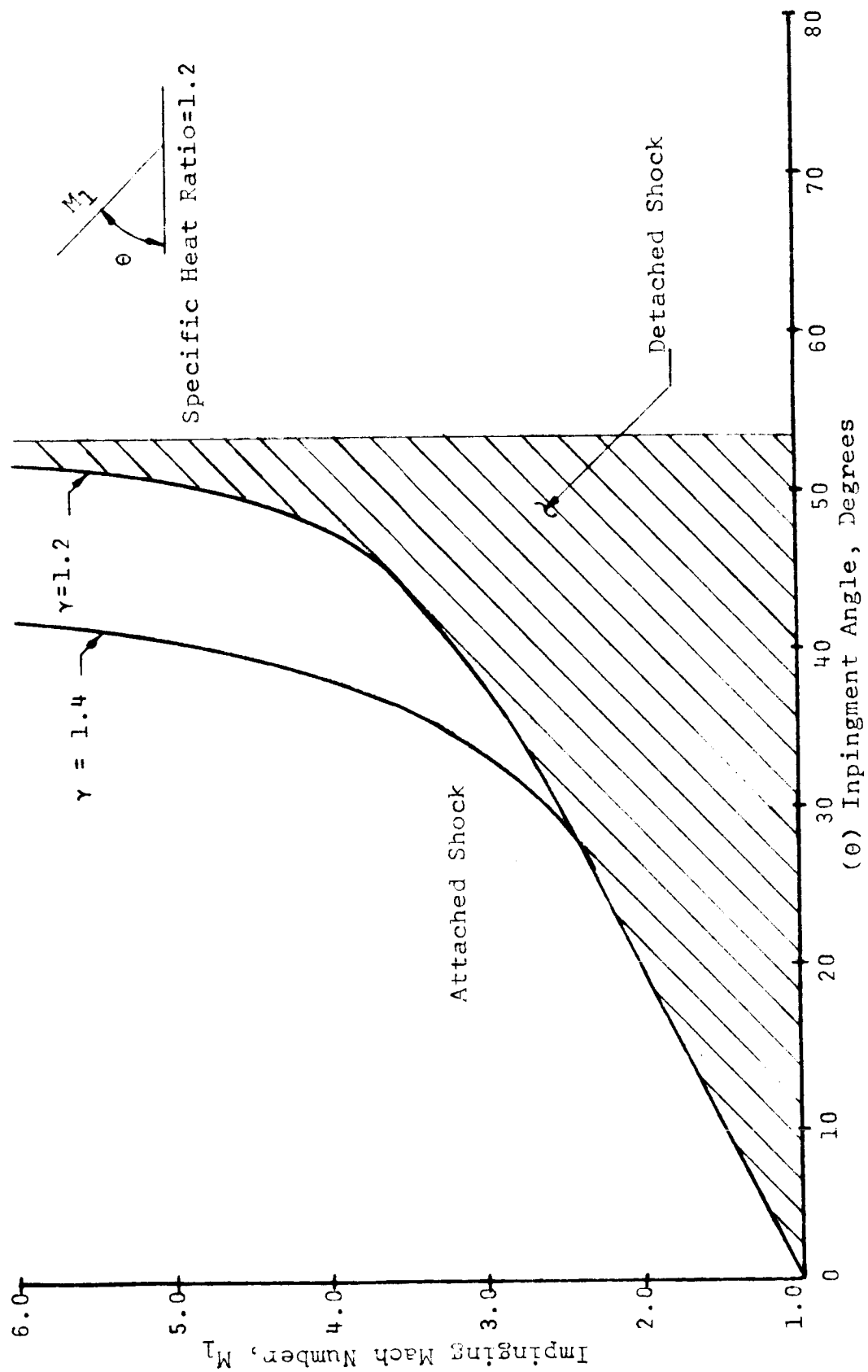
FIG. 2.3-2 MAXIMUM TURNING ANGLE FOR A GIVEN INITIAL MACH NUMBER WITH γ=1.2
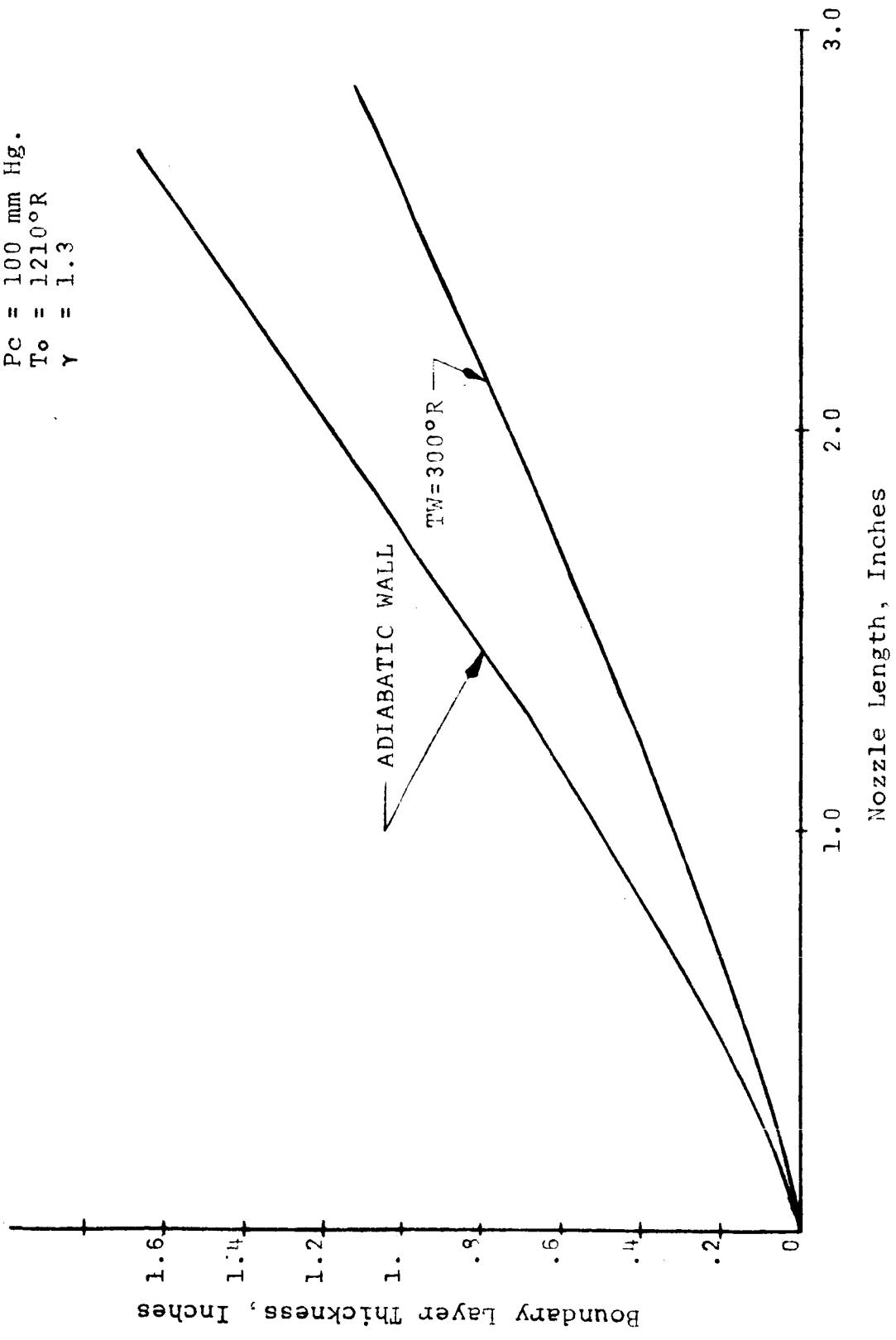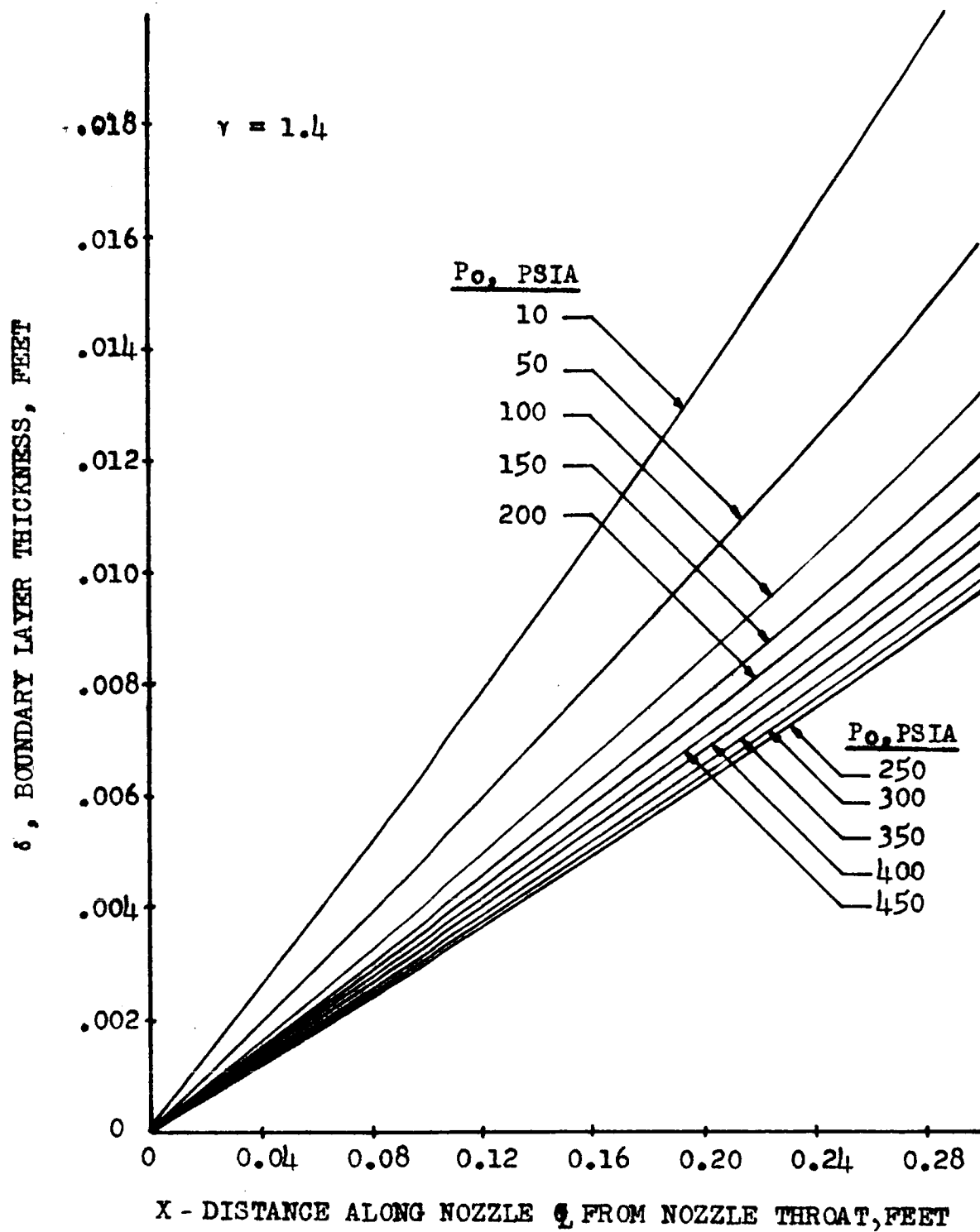
FIG. 2.3-3 ESTIMATED EFFECT OF NOZZLE COOLING ON BOUNDARY LAYER THICKNESS

Fig. 2.3-4 BOUNDARY LAYTER THICKNESS AS A FUNCTION OF
DISTANCE ALONG NOZZLE ℄ AND CHAMBER PRESSURE
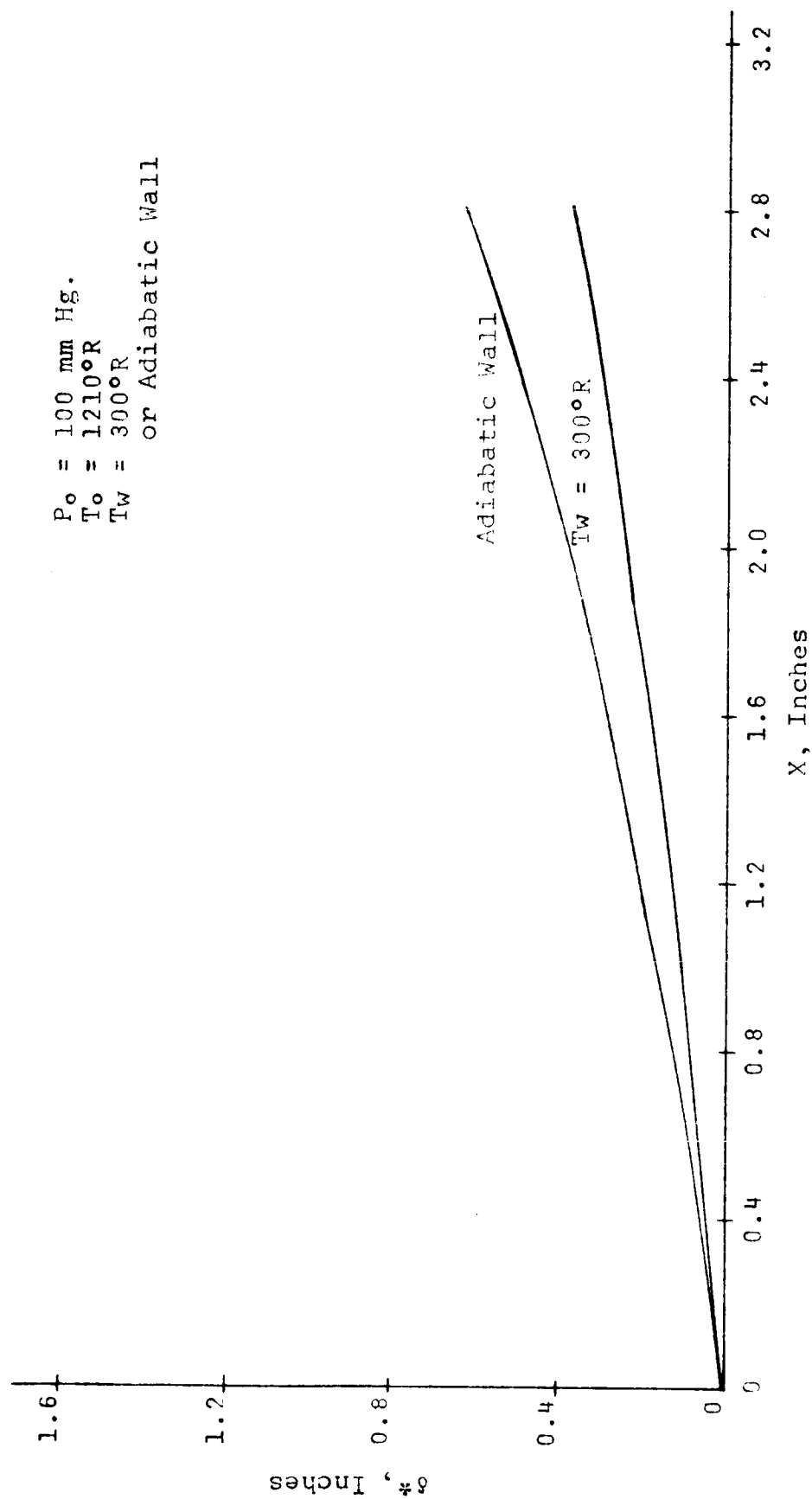FOR TURBULENT FLOW

$P_o = 100$ mm Hg.
$T_o = 1210°R$
$T_w = 300°R$ or Adiabatic Wall

Adiabatic Wall

$T_w = 300°R$

X, Inches

δ^*, Inches

FIG. 2.3-5 BOUNDARY LAYER DISPLACEMENT THICKNESS

2.4   STUDY OF EFFECT OF TWO-DIMENSIONAL PROTUBERANCES ON AERODYNAMIC HEATING

2.4.1   Introduction

When surface irregularities occur in supersonic flow, it is known that the heat transfer coefficients are generally higher than those on a flat surface. The purpose of this study was to develop working equations that could quickly estimate heat transfer coefficients in the vicinity of two-dimensional protuberances in the supersonic regime. A literature survey on the subject was conducted and failed to yield an analytical approach for calculating heat transfer coefficients, but Bertrams's work (Ref. 2.4-1) in the hypersonic range clearly showed that an empirical equation could be written to define heat transfer coefficients.

2.4.2   Analysis

Dimensional analysis was applied to the test data of Burbank (Ref. 2.4-2). The experiments were conducted in the Unitary Plan Wind Tunnel at Langley Research Center (Ref. 2.4-2). This variable pressure, continuous-flow tunnel has an asymmetrical sliding-block nozzle that permits variation in the test section Mach number from 2.30 to 4.65. The free stream Mach numbers in these tests were 2.65, 3.51,

and 4.44. The range of Reynolds number per foot was 1.3 x 10^6 to 4.7 x 10^6. The boundary layer thickness varied during testing from 0.7 to 6 inches. The 6 inch boundary layer normally exists at the wall of the test section of the tunnel. The smaller boundary layers, 0.7 and 1.5 inches, were achieved by inserting a flat plate in the test section and then fixing the protuberance at the wetted length of flat plate required to give the desired boundary layer thickness at the protuberance. A boundary layer trip was placed near the leading edge of the flat plate to force tubulence in the boundary layer. This system is shown in Fig. 2.4-1 , and is explained in detail in Ref. 2.4-2 . The configuration of the protuberances tested are shown in Fig. 2.4-2 .. The basic protuberance was the 1 x 2 and 2 x 4-inch stringer. Effects of the leading edge of the protuberance were investigated by adding to the front of the stringer a 30-degree wedge and 1/4-round cylinder as shown in Fig. 2.4-2 . These three basic geometries were used throughout the testing with the only change being in the size of the protuberance.

In the data analysis of Ref. 2.4-2 , heat transfer coefficients could be defined by the parameters such as Reynolds number, Mach number, boundary layer thickness and geometry of the protuberances; therefore, the problem was defined as having the four independent variables shown as

follows:

$$h/h_o = (Re, M, y/\delta, L/y)$$

Assuming a product solution of the above parameters would result in an equation of the form:

$$h/h_o = \phi \, Re^\alpha \, M^\beta \left(y/\delta\right)^\gamma \left(L/y\right)^\zeta.$$

The exponent α, β, γ and ζ as well as the constant ϕ, were evaluated based on the experimental data of Ref. 2.4-2 . The above equation can be rewritten as

$$\ln\left(h/h_o\right) = \ln\phi + \alpha \ln Re + \beta \ln M \\ + \gamma \ln\left(y/\delta\right) + \zeta \ln\left(L/y\right).$$

The partial derivative of equation (2.4-3) with respect to each of the variables, holding all other parameters constant, allowed each exponent to be evaluated separately, such as

$$\left(\frac{\partial \ln\left(h/h_o\right)}{\partial \ln M}\right)_{\left(Re, \, y/\delta, \, L/y\right)} = \beta$$

where β can be easily determined by extracting the slope of the curve obtained by plotting h/h_o versus M on log log paper as shown in Fig. 2.4-17 . The same operation was performed for each of the other variables. However, in

determining the value of ϕ, it was found that ϕ was a strong function of the ratio δ/y.

2.4.3 Results

The analysis using the above mentioned method and variables resulted in four emperical equations. Equations were derived to define the heat transfer coefficient in each of the three regimes in the vicinity of a protuberance; the regimes are upstream, immediately behind the protuberance in the highly tubulent regime, and downstream of the protuberance behind the point of boundary layer reattachment. The following equations are presented as the results of this study.

Heat transfer coefficients in the upstream regime can be calculated by

$$\frac{h}{h_o} = 66.0\left(1 - 0.091\ \frac{\delta}{y}\right)\left[\frac{M^3}{Re\left(\frac{L}{y} + \frac{\cot\theta}{2}\right)\left(\frac{y}{\delta}\right)^2}\right]^{1/4} \qquad (2.4-5)$$

where h = Local heat transfer coefficient

$\quad$ ho = Local, hot plate, heat transfer coefficient

$\quad$ L = Distance from protuberance

$\quad$ M = Mach number

$\quad$ Re = Local Reynolds number

$\quad$ Y = Height of protuberance

$\quad$ δ = Boundary layer thickness

$\quad$ θ = Angle of leading edge of protuberance

This equation can be applied to a two-dimensional protuberance with $\frac{\delta}{y} < 4$. For $\frac{\delta}{y} > 4$ the following empirical

equation is recommended.

$$h/h_0 =$$

$$100 \left[\frac{m^{0.75}}{Re^{(0.25-0.02\,y/\delta)} \left(\frac{L}{y} + \frac{\alpha + \theta}{2}\right)^{0.2} exp\left(0.7\,y/\delta\right)} \right] \quad (2.4\text{-}6)$$

Heat transfer behind the protuberance is defined by two equations which depend on the distance downstream of the trailing edge. At ratios L/y $\geq$ 2 the following equation is used:

$$h/h_0 = 1.0 + 0.025 \left[R_e\, M^2 \left(y/L\right)^2 \left(\delta/y\right) \right]^{1/8}. \quad (2.4\text{-}7)$$

This equation, therefore, defines the heat transfer after boundary layer reattachment which occurs at $L/y \approx 2$. This equation holds only for a vertical edge. It should be noted that the angle of leading edge does not effect the heat transfer behind the protuberance.

In the area immediately behind the protuberance in the highly turbulent regime, the equation defining the heat transfer is

$$h/h_0 = 0.25 \left(\frac{L}{y}\right)^2 \left[1.0 + 0.021 \left(R_e\, M^2 \frac{\delta}{y} \right)^{1/5} \right]. \quad (2.4\text{-}8)$$

This equation applies only when $L/y < 2$ and when the trailing edge is vertical to the flat surface.

Since most of the test data are for the upstream regime, it was necessary, for clarity, to present this data

in Fig. 2.4-3, -4 and -5 for Mach numbers 2.65, 3.51
and 4.44, respectively. The accuracy of the correlation
appears to be good at Mach numbers 2.65 and 3.51; however,
at Mach number 4.44 the inaccuracies of the test data (Ref.
2.4-2) take effect and consequently a poorer correlation
is shown. Fig. 2.4-6 to -16 shows the overall picture
of the protuberance, test data, and the correlation of all
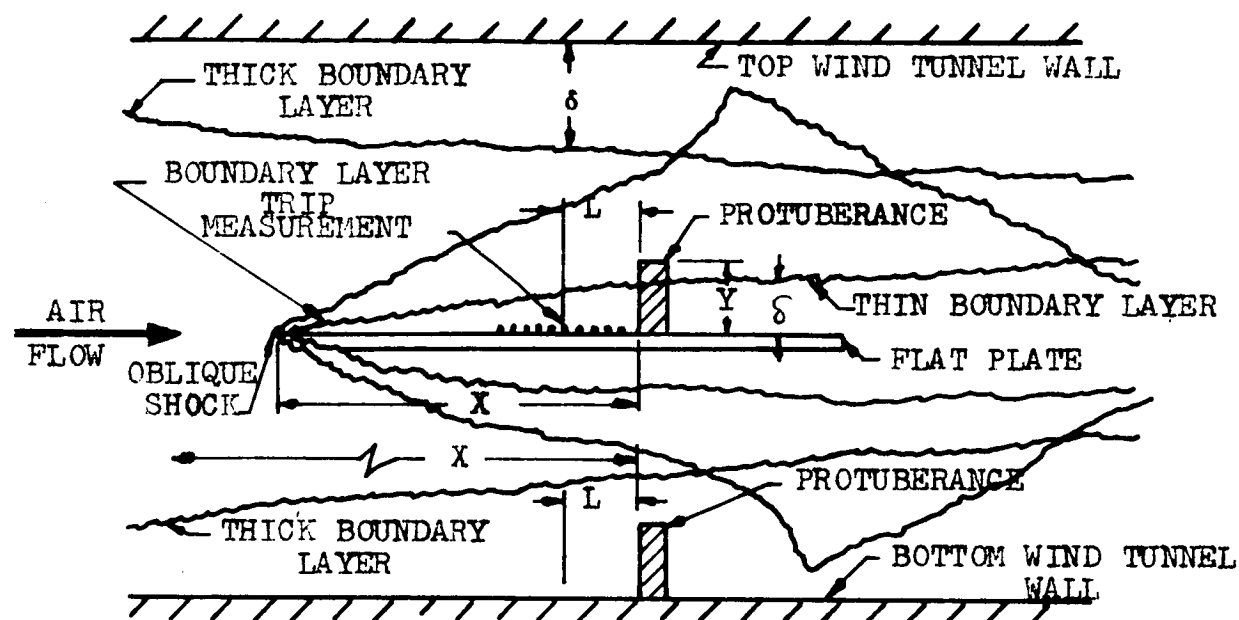equations in their respective regimes.

2.4.4 Conclusion

Throughout the analysis of the test data the critical
parameters appeared to be Mach number and the ratio $\frac{y}{\delta}$ and
L/y. Reynolds number showed small effects on the final
result. The above equation should be limited to the range
of the test data (Ref. 2.4-2). Corrected stream properties
behind the oblique shock must be used in all calculations.
Extrapolation of the equations should be handled with caution
especially when the ratio Y/δ and L/Y are concerned. Equations
1 and 2 were applied to preliminary, unpublished test data
having numerically similar parameters as presented herein
with the exception of Mach number which was 5.2; the agree-
ment was within ± 10 percent in all cases. Extrapolation
into high Mach number is not suggested because of the real
gas effects in the hypersonic regime.

2.4.5 Reference

2.4-1. Bertram, and Wiggs, "Effect of Surface Distortions

on the Heat Transfer to a Wing at Hypersonic Speed",
NASA Langley Research Center, Hampton, Va. AIAA
Jour. $\underline{1}$, June, 1963.

-2. Burbank, Newlander, and Collins, "Heat-Transfer and
Pressure Measurements on a Flat-Plate Surface and
Heat-Transfer Measurements on Attached Protuberances
in a Supersonic Tubulent Boundary Layer at Mach Numbers
of 2.65, 3.51 and 4.44". National Aeronautics and
Space Administration, NASA TN D-1372, December, 1962.

THICK BOUNDARY LAYER

TOP WIND TUNNEL WALL

δ

BOUNDARY LAYER
TRIP
MEASUREMENT

L

PROTUBERANCE

AIR
FLOW

THIN BOUNDARY LAYER

Y δ

OBLIQUE
SHOCK

FLAT PLATE

X

X

L

THICK BOUNDARY
LAYER

PROTUBERANCE

BOTTOM WIND TUNNEL
WALL

SIDE VIEW

SIDE WIND TUNNEL
WALL

MEASUREMENT

THICK BOUNDARY
LAYER

X

AIR
FLOW

PROTUBERANCE

L

THICK BOUNDARY LAYER

SIDE WIND TUNNEL WALL
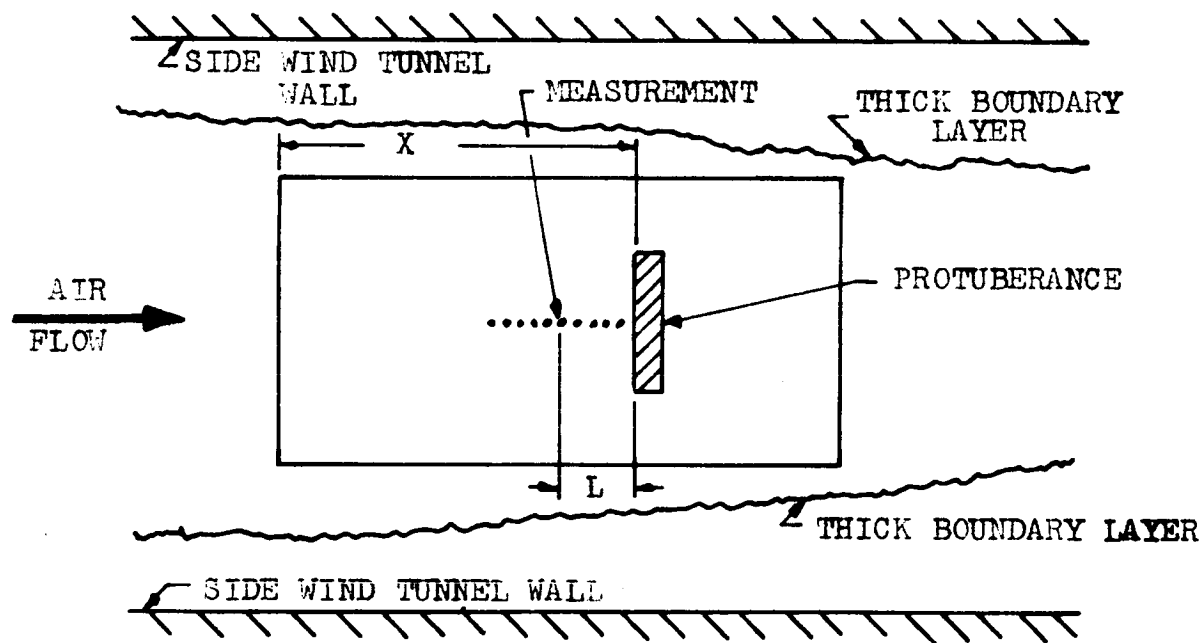
TOP VIEW

FIG. 2.4-1   WIND TUNNEL TEST SECTION

Flow of Air
in all cases

$Y=4"$

$\theta=90°$

2 X 4 STRINGER

$Y=2"$

$\theta=90°$

1 X 2 STRINGER

$\theta=45°$

Y

1/4-ROUND CYLINDER

$\theta=30°$

Y

30° WEDGE
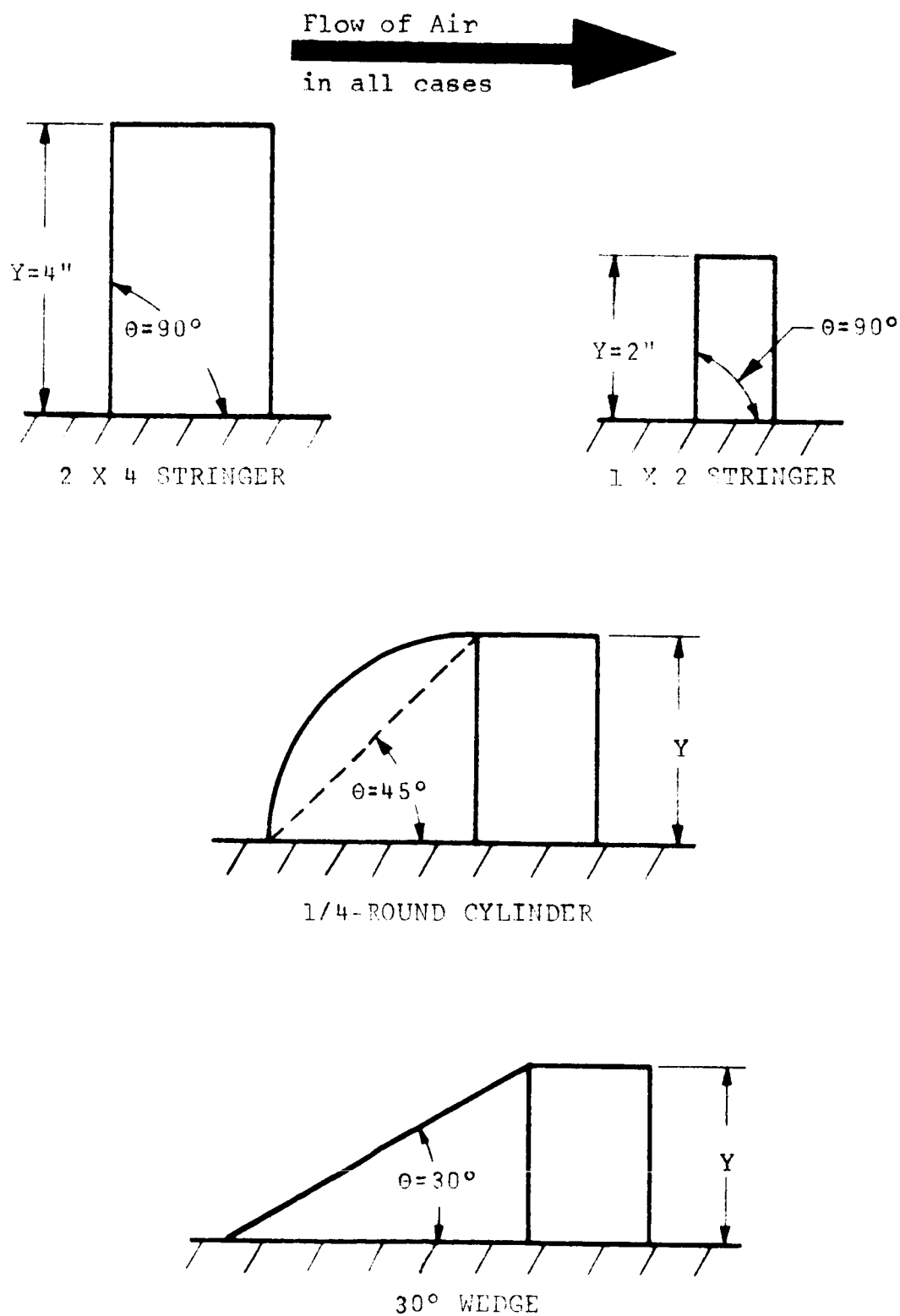
FIG. 2.4-2 TYPES OF PROTUBERANCES

ANALYTICAL
M = 2.65
TEST DATA
○ RECTANGULAR
STIFFENER
△ STIFFENER WITH
30° WEDGE
□ STIFFENER WITH 1/4
ROUND CYLINDER

$$\left(1.10 - 0.10 \frac{\delta}{\gamma}\right)^4 \left[\frac{M^3}{R_e \left(\frac{L}{\gamma} + \frac{Cot\,\theta}{2}\right)\left(\frac{\gamma}{\delta}\right)^2}\right]$$

h/h_o
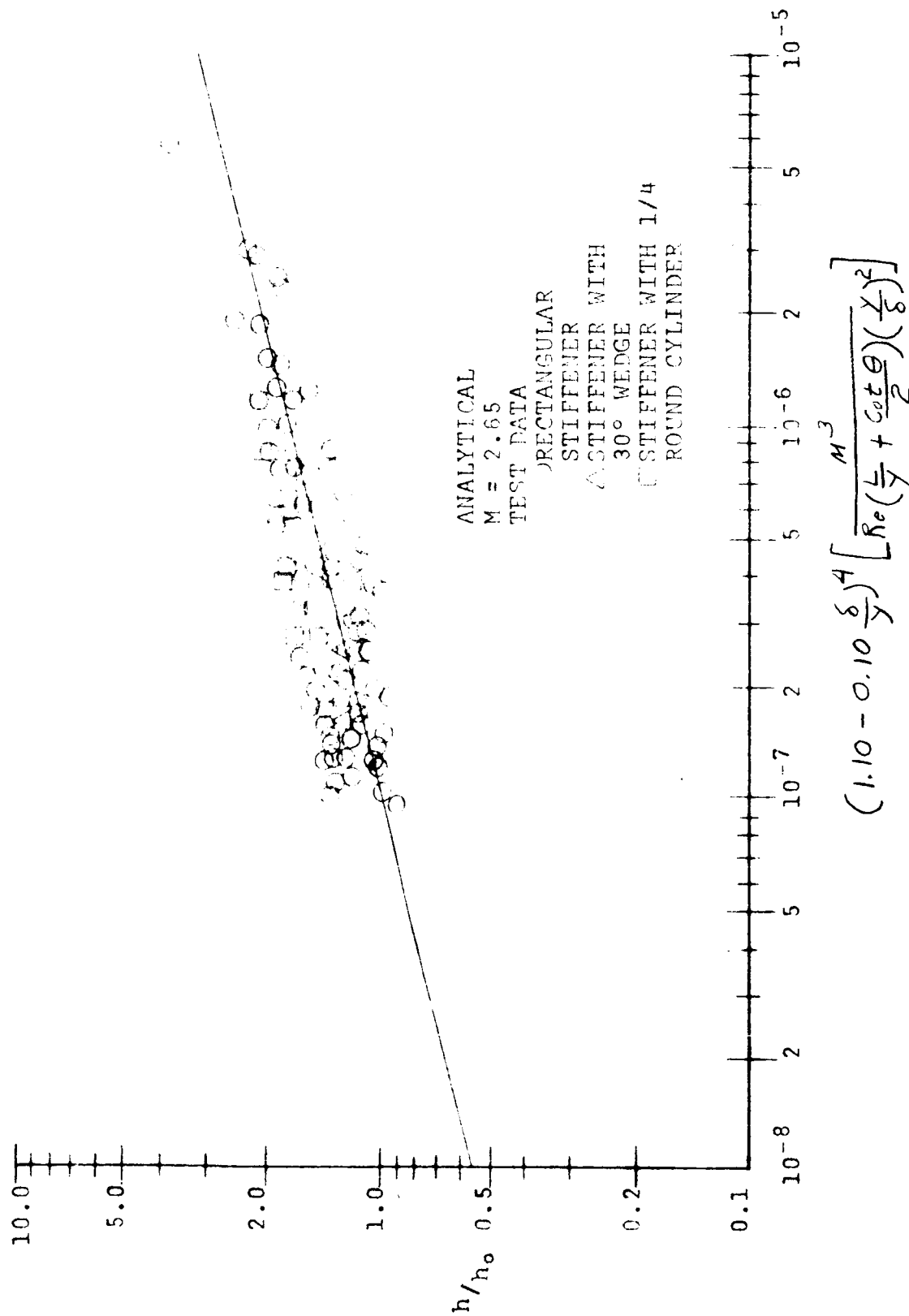
FIG. 2.4-3 CORRELATION OF EXPERIMENTAL DATA AT MACH 2.65

ANALYTICAL
M=3.51
TEST DATA

◯ RECTANGULAR STIFFENER
△ STIFFENER WITH 30° WEDGE
▢ STIFFENER WITH 1/4 ROUND CYLINDER

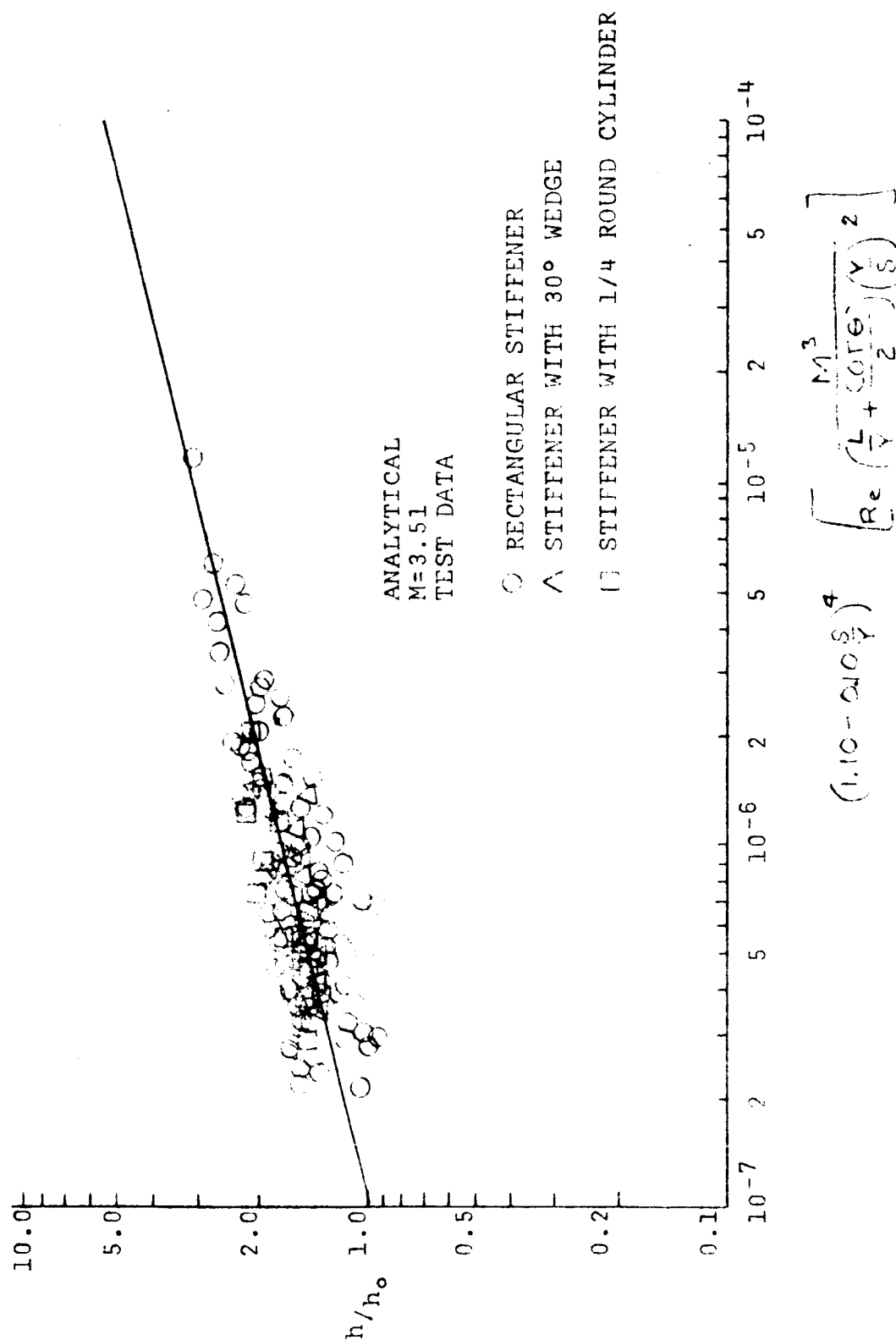$$\left(1.10 - 2.10 \frac{v}{S}\right)^4 \sqrt{R_e \left(\frac{L}{v} + \frac{\cot\theta}{2}\right)\left(\frac{v}{S}\right)^2 \left[\frac{M^3}{}\right]}$$

FIG. 2.4-4 CORRELATION OF EXPERIMENTAL DATA AT MACH 3.51
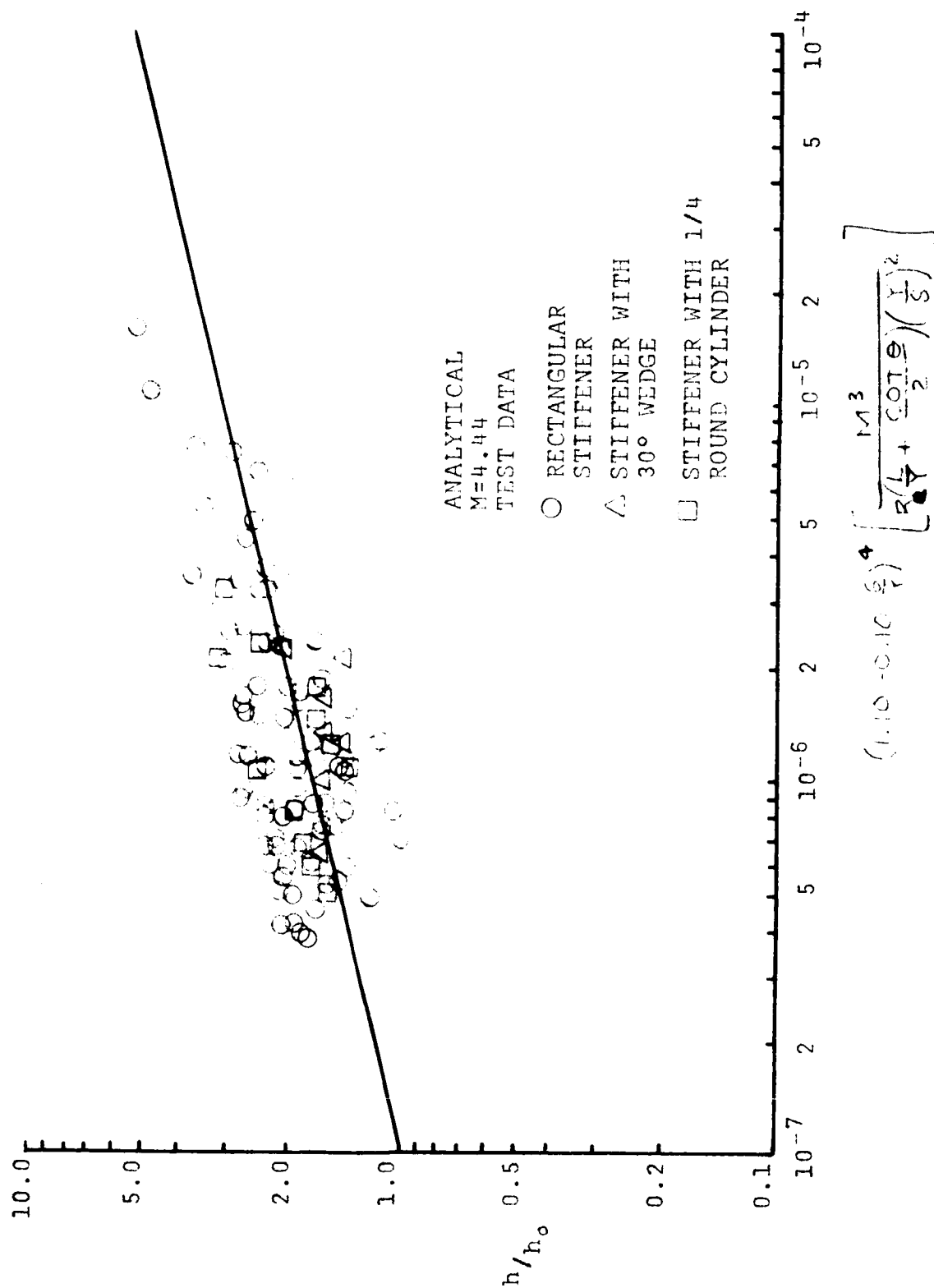
FIG. 2.4-5 CORRELATION OF EXPERIMENTAL DATA AT MACH 4.44

CONFIGURATION: 1X2 Flange
M=2.65   δ=6.0 INCHES

$Re_x \times 10^{-6}$ FT	ANALYTICAL	TEST DATA
1.29	—··—	△
2.57	——	O

FLOW OF AIR →

h/h₀

L , INCHES

— X=39.1 FEET —

FIG. 2.4-6   COMPARISON OF EMPIRICAL EQUATION TO EXPERIMENTAL DATA AT MACH 2.65

CONFIGURATION: 1X2 FLANGE
M=3.51 δ=1.5 INCHES

Re/Ft X10⁻⁶ ANALYTICAL	TEST DATA
4.01	△
2.82	○
1.61	□

FLOW OF AIR

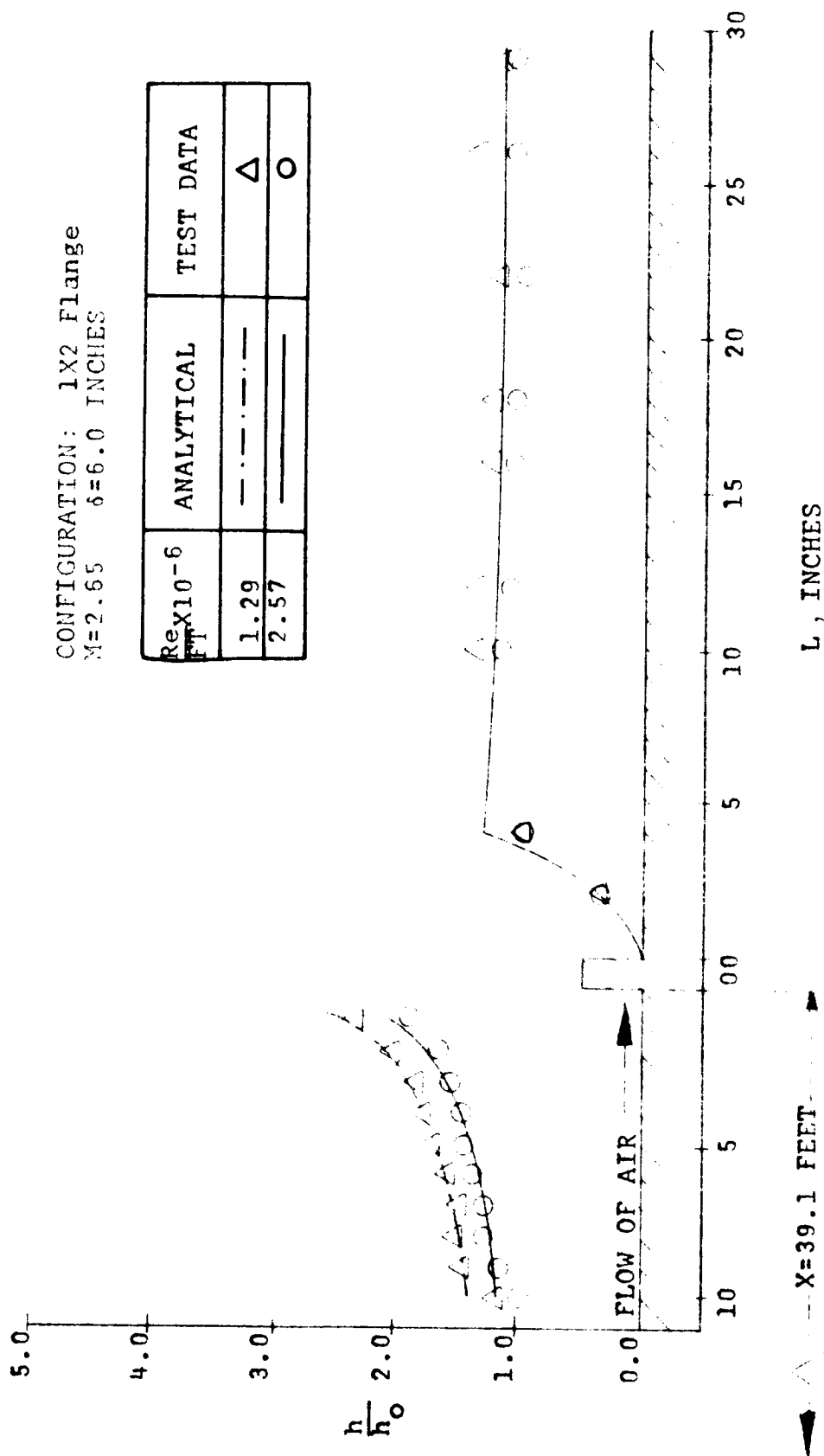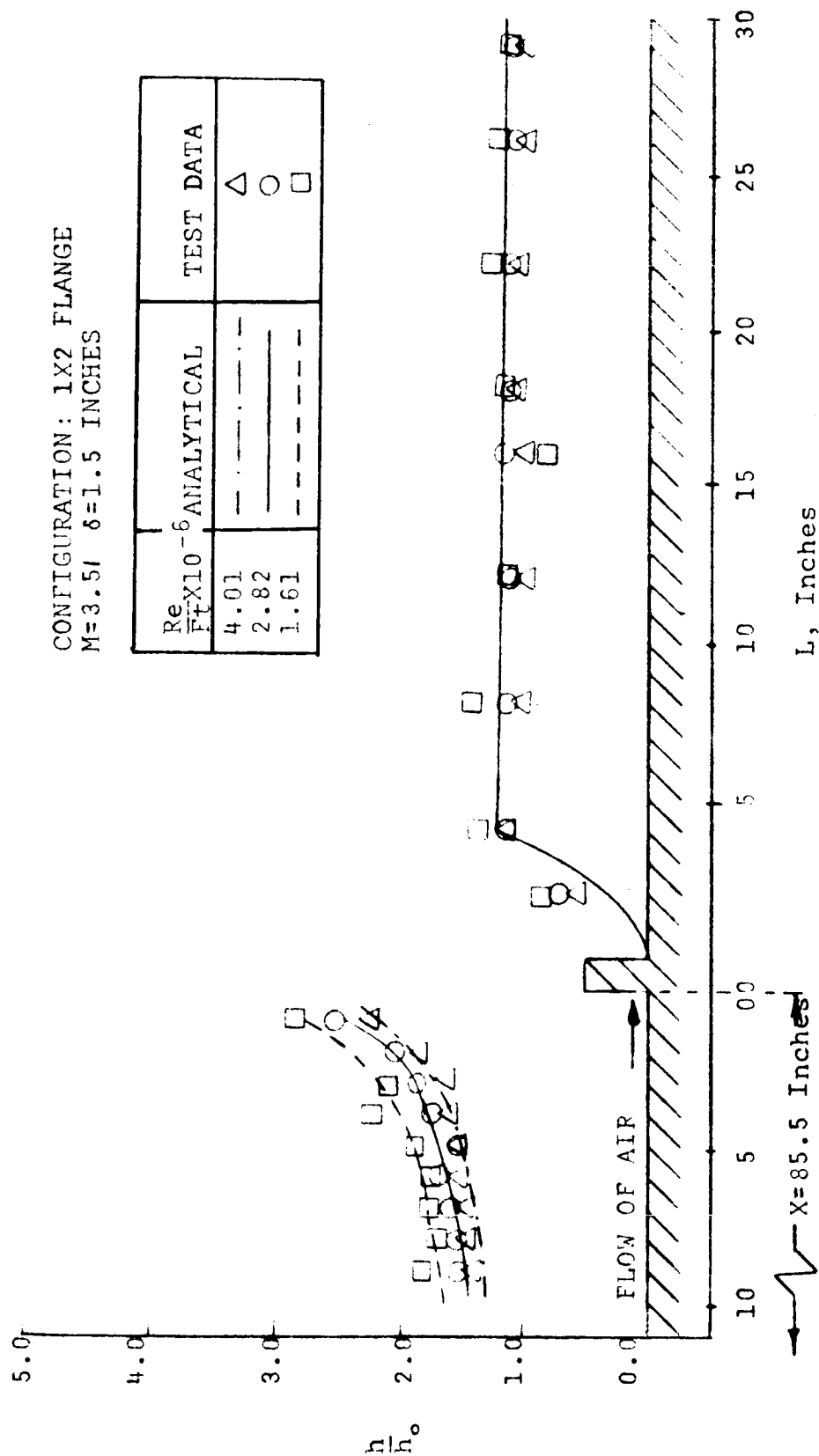X=85.5 Inches

L, Inches

h/h₀

FIG. 2.4-7 COMPARISON OF EMPIRICAL EQUATION TO EXPERIMENTAL DATA AT MACH 3.51

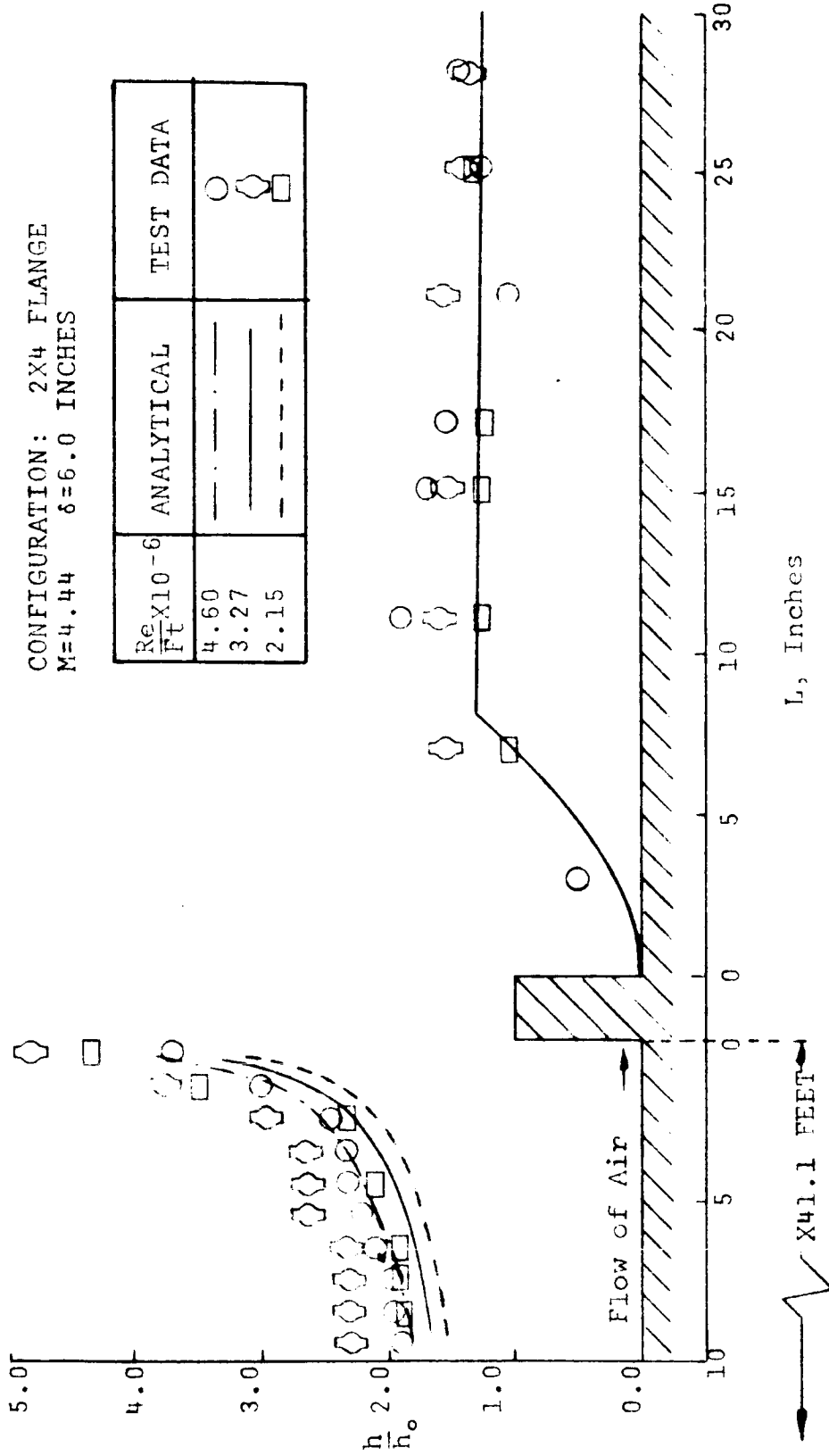FIG. 2.4-8 COMPARISON OF EMPIRICAL EQUATION TO EXPERIMENTAL DATA AT MACH 4.44

CONFIGURATION: 1X2 FLANGE
M=2.65 δ =0.7 INCHES

$\frac{Re}{FT}X10^{-6}$	ANALYTICAL	TEST DATA
3.98	— · —	$\triangle$
2.55	——	$\bigcirc$
1.29	— —	$\square$

FLOW OF AIR

X 25.5 INCHES

L , INCHES

$\frac{h}{h_o}$

FIG. 2.4-9 COMPARISON OF EMPIRICAL EQUATION TO EXPERIMENTAL DATA AT MACH 2.65

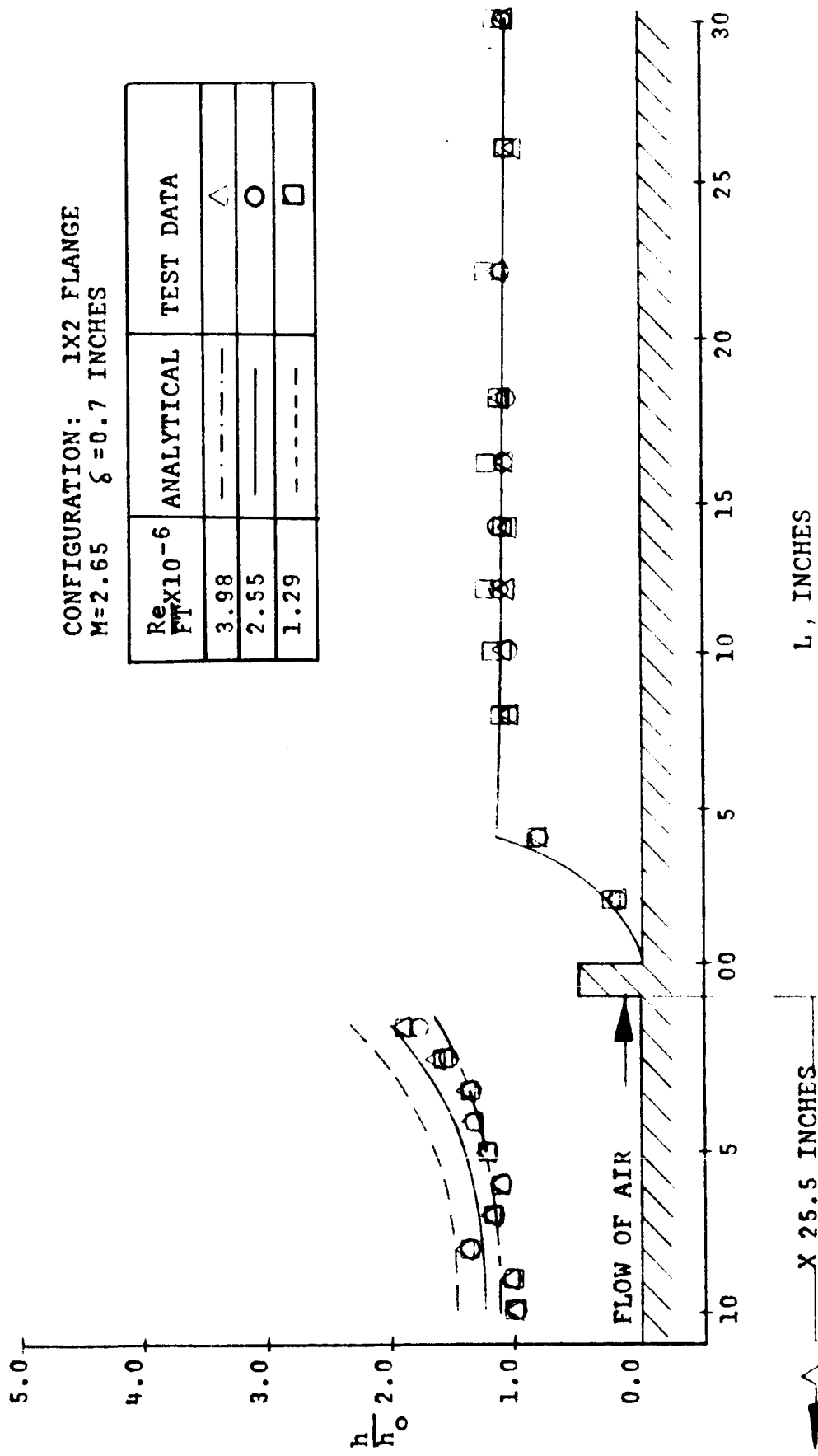FIG. 2.4-10 COMPARISON OF EMPRICAL EQUATION TO EXPERIMENTAL DATA AT MACH 2.65

FIG. 2.4-11 COMPARISON OF EMPIRICAL EQUATION TO EXPERIMENTAL DATA AT MACH 2.65

CONFIGURATION: 1X2 FLANGE
M=3.51 δ=0.7 INCHES

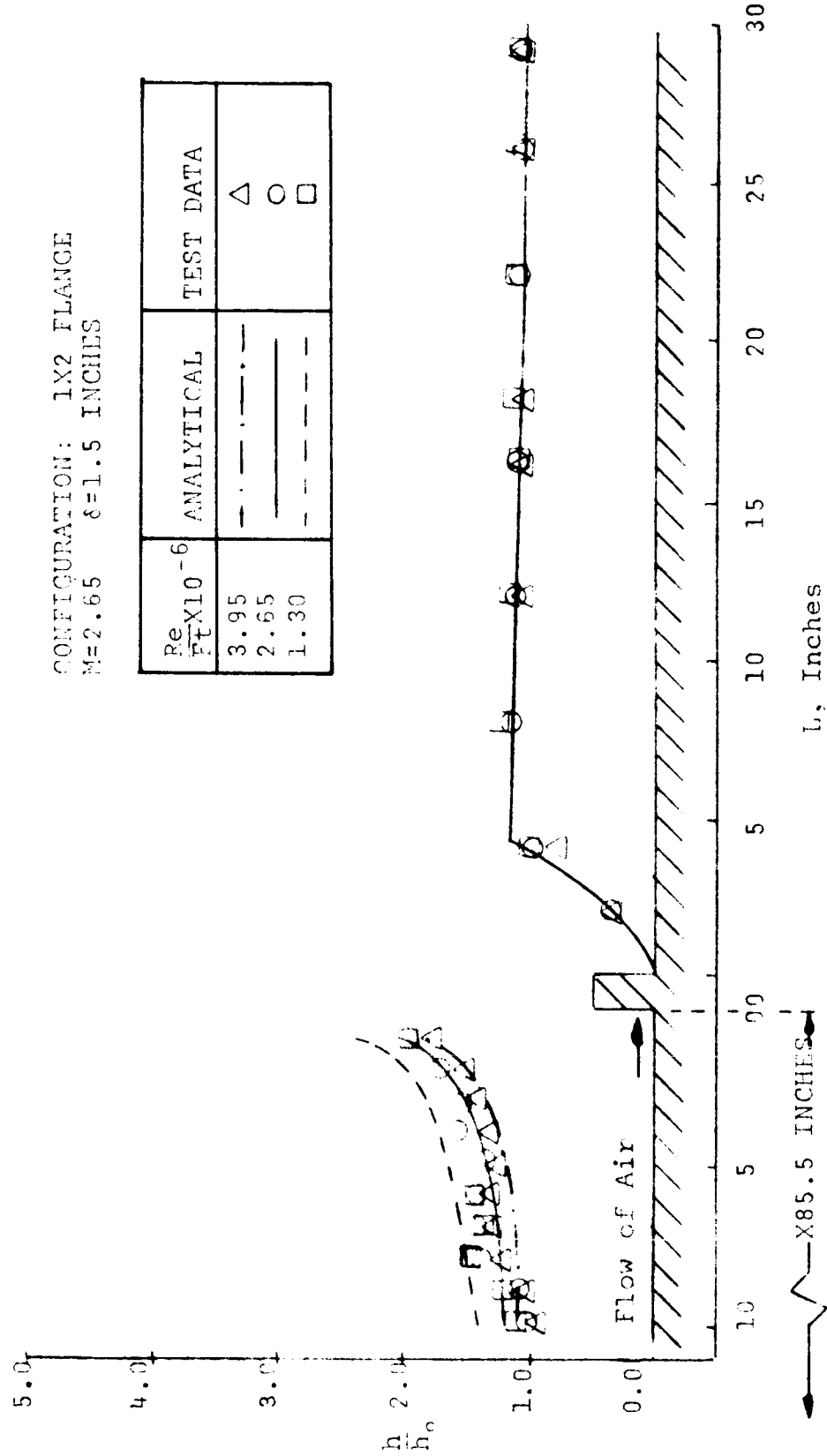| $\frac{Re}{Ft}$X10^{-6}	ANALYTICAL	TEST DATA
3.98	—·—·—	△
2.80	———	○
1.64	— — —	□
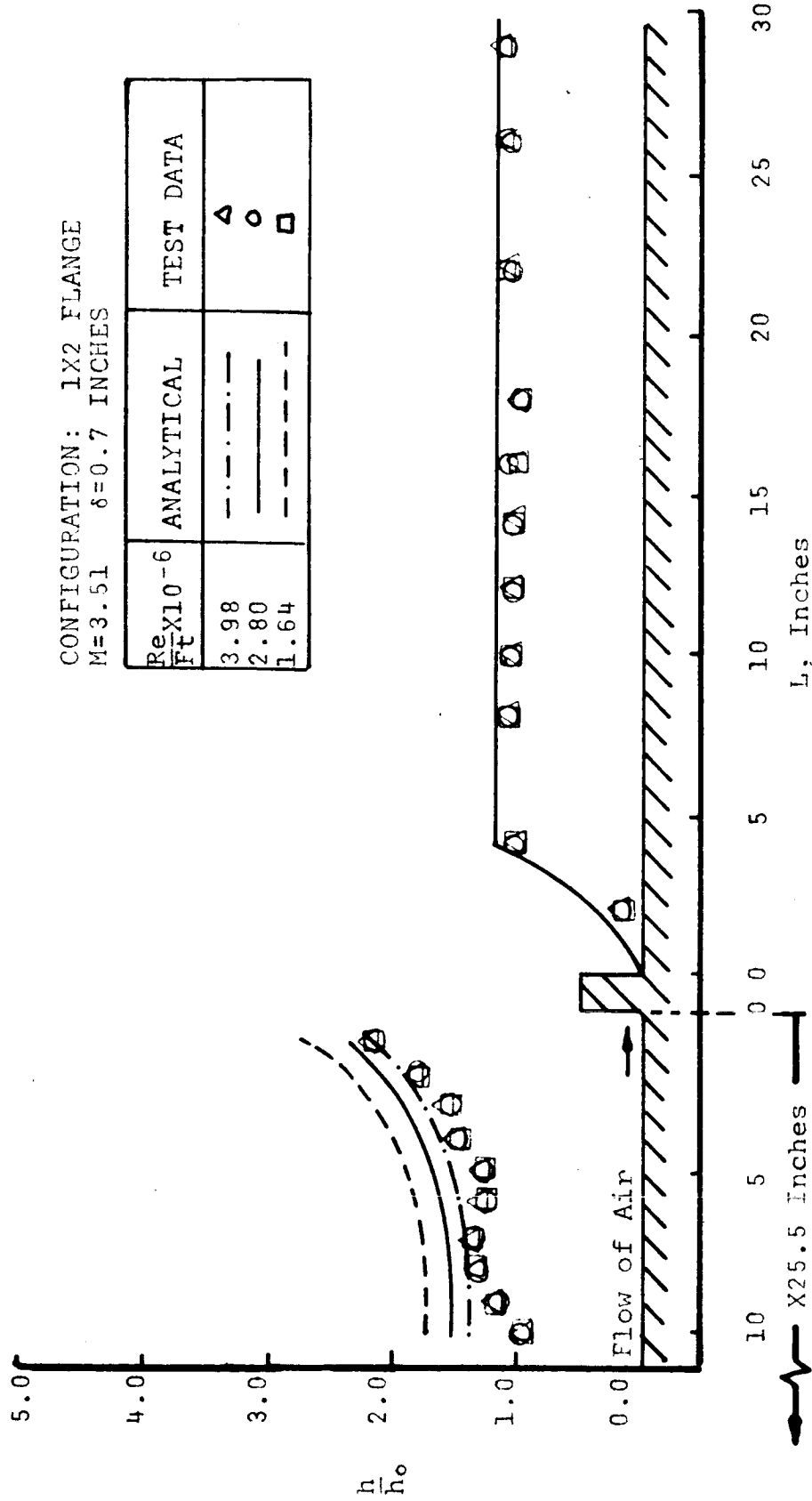
FIG. 2.4-12   COMPARISON OF EMPIRICAL EQUATION TO EXPERIMENTAL DATA AT MACH 3.51
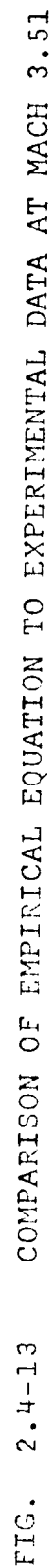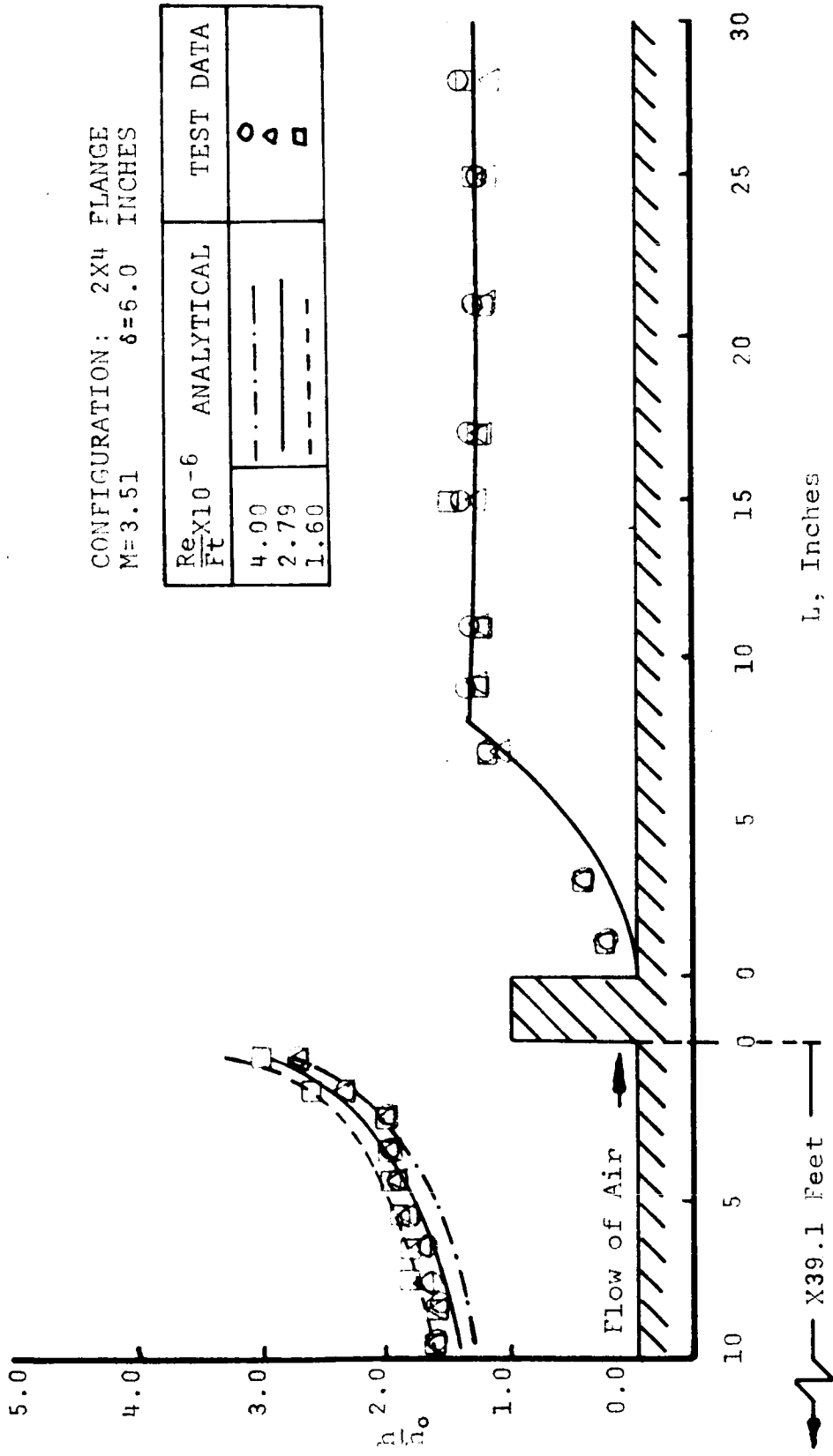
CONFIGURATION: 1X2 FLANGE
M=3.51   δ=6.0 INCHES

$Re \times 10^{-6}$ ft	ANALYTICAL	TEST DATA
2.77	—·—·—	◁
1.59	———	○

$\dfrac{h}{h_o}$
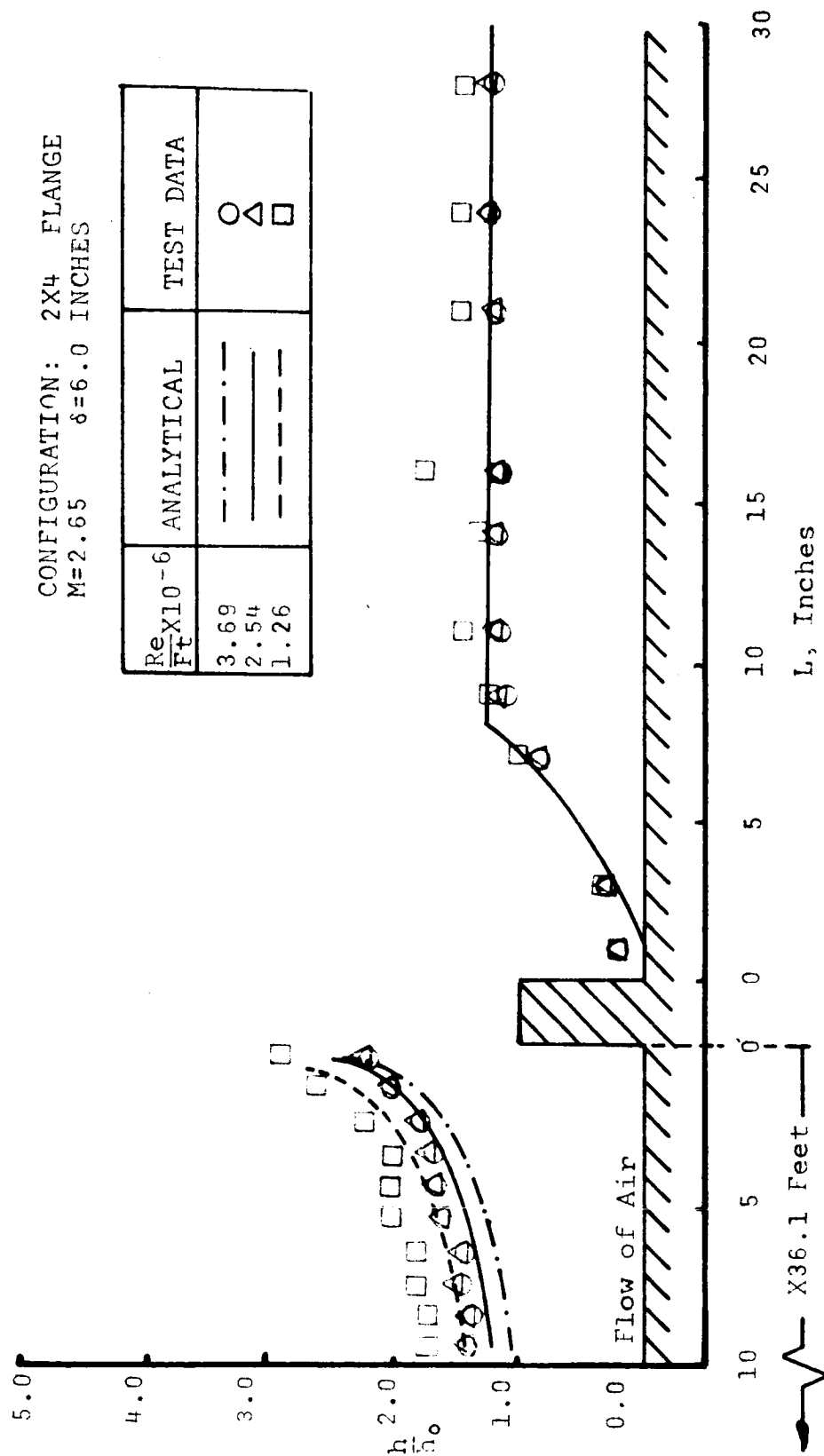
Flow of Air

L, Inches

X39.1 Feet

FIG. 2.4-13   COMPARISON OF EMPIRICAL EQUATION TO EXPERIMENTAL DATA AT MACH 3.51

FIG. 2.4-14   COMPARISON OF EMPIRICAL EQUATION TO EXPERIMENTAL DATA AT MACH 3.51

CONFIGURATION: 1X2 FLANGE
M=4.44 δ=0.7 INCHES

$\frac{Re}{Ft} \times 10^{-6}$	ANALYTICAL	TEST DATA
4.39	—·—·—	△
3.15	———	○
2.11	– – –	□

$\frac{h}{h_o}$

L, Inches

Flow of Air →

X=25.5 INCHES
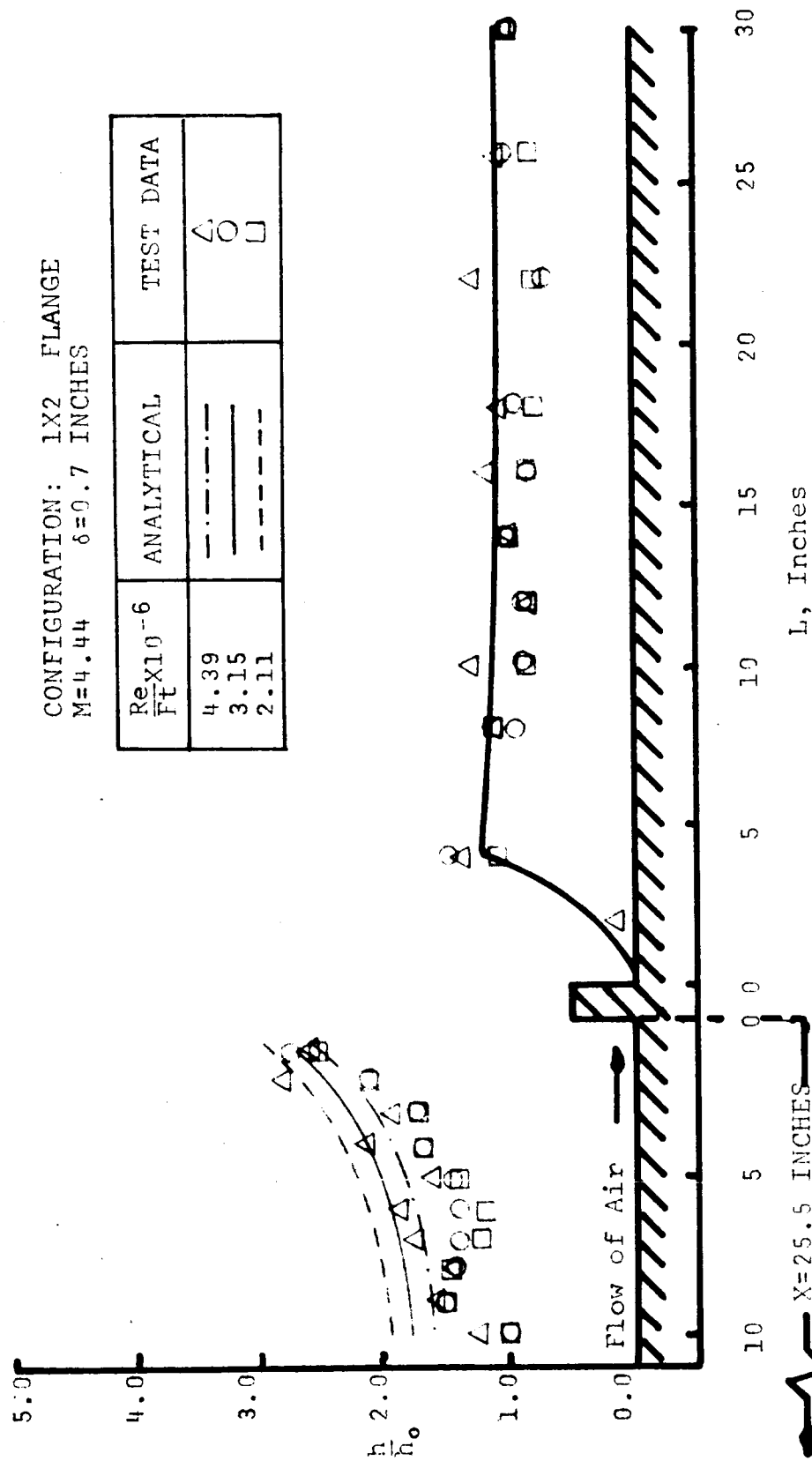
FIG. 2.4-15 COMPARISON OF EMPIRICAL EQUATION TO EXPERIMENTAL DATA AT MACH 4.44

CONFIGURATION: 1X2 FLANGE
M=4.44 δ=1.5 INCHES

$\frac{Re}{Ft}$ X10^{-6}	ANALYTICAL	TEST DATA
4.64	—··—	△
3.24	——	○
2.15	— —	□

L~INCHES

FLOW OF AIR

X85.5 INCHES

$\frac{h}{h_o}$
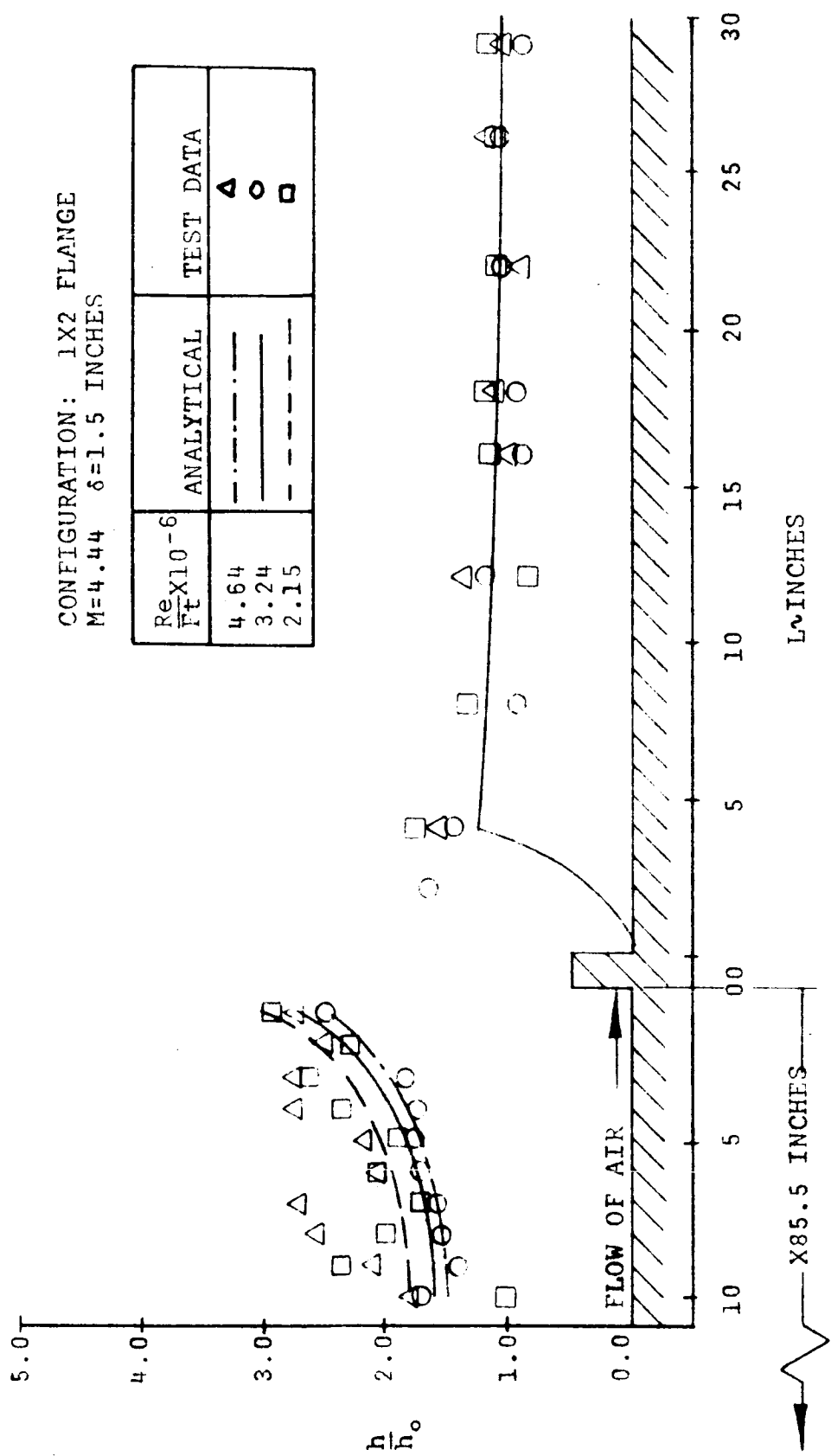
FIG. 2.4-16 COMPARISON OF EMPIRICAL EQUATION TO EXPERIMENTAL DATA AT MACH 4.44

FIG. 2.4-17   LOCAL MACH NUMBER
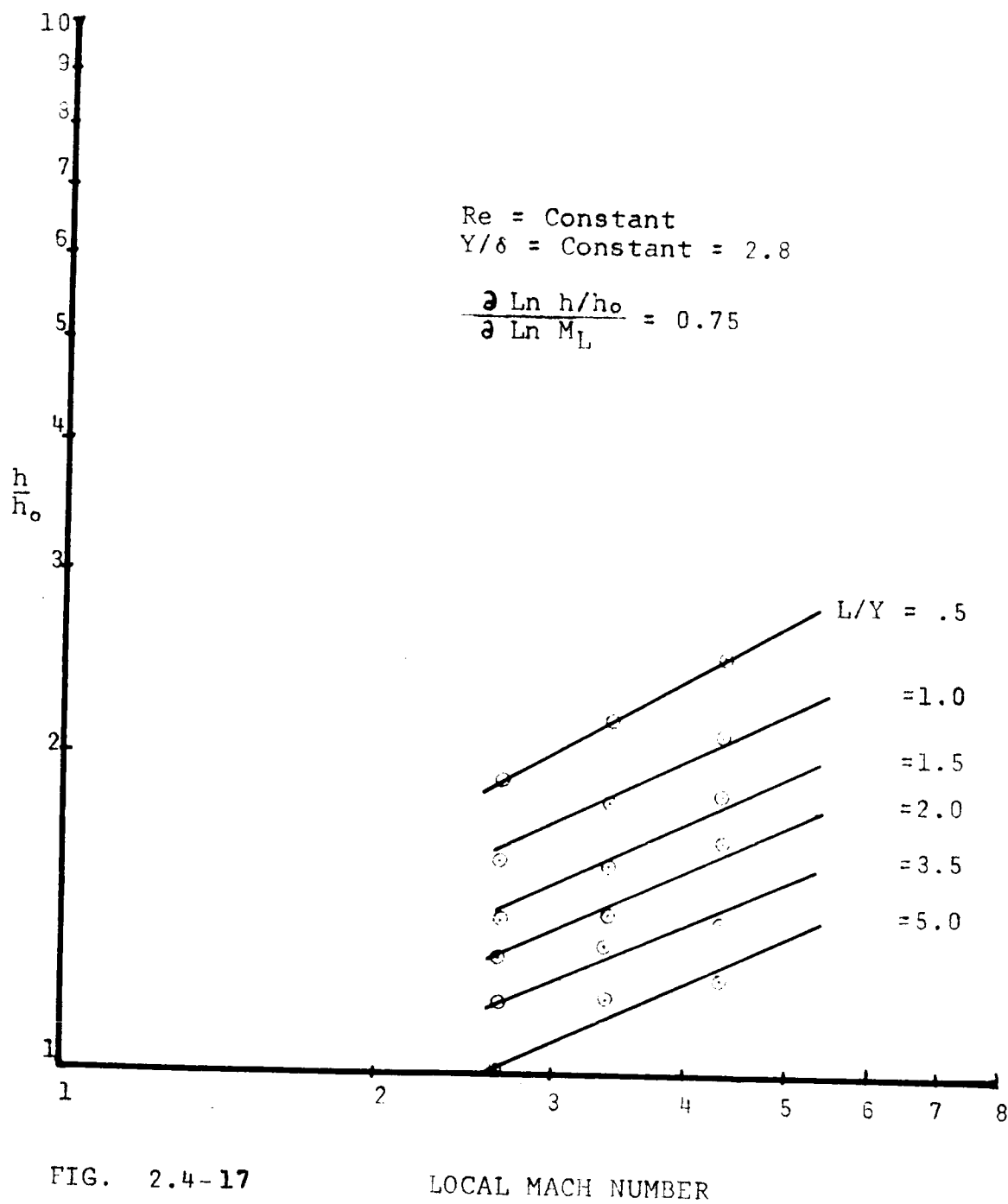
2.5 EFFECT OF VARIOUS DYNAMIC AND THERMODYNAMIC PERTURBATIONS ON AERODYNAMIC HEATING

2.5.1 Introduction

In the design of space vehicle boosters the effect of aerodynamic heating must be considered as part of the design criteria. Defining the design criteria, however, can be a difficult problem when variations during flight can drastically affect these criteria. The perturbations (variations) in atmospheric conditions and vehicle dynamics through flight will affect the aerodynamic heating rate. It is the purpose of this work to include the most probable perturbations into the theory of aerodynamic heating and determine the effects of these perturbations on design predictions.

2.5.2 Method of Approach

The method of approach was to first select the suitable equations to calculate the external film coefficient. Van Driest's equation was selected for this analysis and has been converted to working formulas in Ref. 2.5-1 .

The main differences of the present analysis from Ref. 2.5-1 result from converting the equations from English System to Metric System with a different equation for thermal conductivity. The Sutherland's constant and

equation of thermal conductivity were obtained from Ref. 2.5-2.

The working formulas can be summarized as **follows**:

1. $T_r = T_\infty' \left[1 + \frac{(V_\alpha'/\cos \alpha')^2}{1433\ T_\infty'} \right]$

2. $T^* = T_\infty' + 0.5 \left[T_{woa} - T_\infty' \right] + 0.22 \left[T_r - T_\infty' \right]$

3. $\mu^* = 1.458 \times 10^{-6} \left[\frac{(T^*)^{3/2}}{T^* + 110.4} \right]$

4. $\rho^* = \rho_\infty' \left(\frac{T'}{T^*} \right)$

5. $Re^* = \rho^* \frac{(V_\infty'/\cos \alpha')\ x}{\mu^*}$

6. $K^* = 6.325 \times 10^{-7} \left[\frac{(T^*)^{3/2}}{T^* + 245.4 \times 10^{-(12/T^*)}} \right]$

7. $h_{woa} = 0.165 \left(\frac{K^*}{x} \right) \left[\frac{Re^*}{(\log_{10} Re^*)^{2.584}} \right]$

8. $T_{woa} = \dfrac{h_{woa} T_r - \epsilon (1.355 \times 10^{-3}) \left(\frac{T_{woa}}{100} \right)^4}{h_{woa}}$

where

$$T_\infty^{\,\prime} = T_\infty + \Delta T_\infty$$

$$\rho_\infty^{\,\prime} = \rho_\infty + \Delta \rho_\infty$$

$$V_\infty^{\,\prime} = V_\infty + \Delta V_\infty$$

$$\alpha^{\,\prime} = \alpha + \Delta \alpha$$

and the symbols are as follows:

Expression	Quantity	Units
α	Angle of attack	Degree
ϵ	Emissivity	Dimensionless
θ	Time	Second
ρ_∞	Density of air	Kg/M^3
ρ^*	Reference density of air	Kg/M^3
Δ	Deviation from normal or standard condition	Dimensionless
μ^*	Reference viscosity	Kg/M. sec
A	Altitude	M
$f(\theta)$	Function of time	Dimensionless
h_{woa}	Outside film coefficient base on radiation equilibrium wall temperature	$\dfrac{K\text{-}Cal}{M^2 \ sec \ {}^\circ K}$
K^*	Reference thermal conductivity of air	$\dfrac{K\text{-}Cal}{M \ sec \ {}^\circ K}$
Re^*	Reference Reynolds number	Dimensionless
T_∞	Ambient temperature	${}^\circ K$

T_r	Recovery temperature	°K
$T_{w o \alpha}$	Radiation equilibrium temperature	°K
T^*	Reference temperature	°K
V_∞	Velocity of Vehicle	M/sec
X	Distance from vehicle nose to representative point on external surface.	M

Calculations in this analysis were performed on an IBM 7090 computer. The inputs are:

1. $T_\infty \ f(A)$

2. $\rho_\infty \ f(A)$

3. $V_\infty \ f(\theta)$

4. $A \ f(\theta)$

5. $\alpha \ f(\theta)$

6. $\Delta T_\infty \ f(A)$

7. $\Delta \rho_\infty \ f(A)$

8. $\Delta V_\infty \ f(\theta)$

9. $\Delta \alpha \ f(\theta)$

10. ϵ

11. X

12. θ_o

13. $\Delta \theta$

14. θ_{end}

where:

   f (A) = Function of altitude

   f (θ) = Function of time.

2.5.3 Discussion of Results

Data (Ref. 2.5-3) from Patrick AFB, Florida were taken as atmospheric conditions. Sixty-five combinations of perturbations were analysed. Because of limited time only a few of the results are shown in (Fig. 2.5-1). This figure shows the histories of ratio of perturbation-heating-to-normal (no perturbation)-heating. In the analysis, radiation equilibrium was assumed to exist at the surface.

2.5.4 Conclusions

From this preliminary work it appears that velocity and density perturbations greatly influence the aerodynamic heating rate. The temperature and a $\pm$ four degree angle-of-attack perturbations showed small effect on the final results.

2.5.5 References

2.5-1. "Main Propellant Tank Pressurization System Study and Test Program, Volume IV by Lockheed-Georgia Company, A Division of Lockheed Aircraft Corporation, Marietta, Georgia, 1961.

   -2. U. S. Standard Atmosphere, 1962.

   -3. A Reference Atmosphere for Patrick AFB, Florida, NASA TN-D-595, by Orvel E. Smith, 1961.
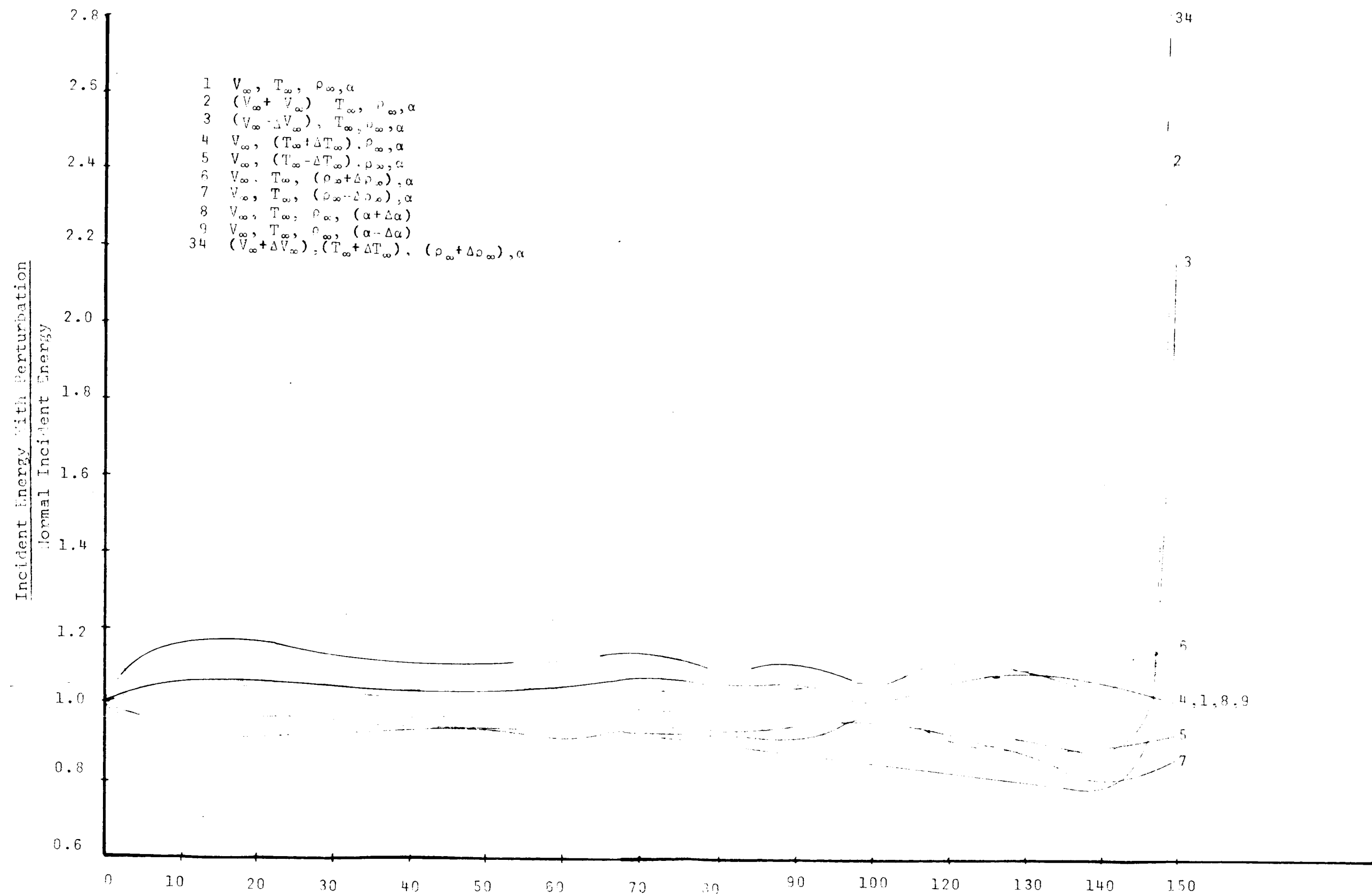
Incident Energy With Perturbation / Normal Incident Energy

2.8

2.6

2.4

2.2

2.0

1.8

1.6

1.4

1.2

1.0

0.8

0.6

1   V_∞, T_∞, ρ_∞, α
2   $(V_\infty + \Delta V_\infty)$, T_∞, ρ_∞, α
3   $(V_\infty - \Delta V_\infty)$, T_∞, ρ_∞, α
4   V_∞, $(T_\infty + \Delta T_\infty)$, ρ_∞, α
5   V_∞, $(T_\infty - \Delta T_\infty)$, ρ_∞, α
6   V_∞, T_∞, $(\rho_\infty + \Delta\rho_\infty)$, α
7   V_∞, T_∞, $(\rho_\infty - \Delta\rho_\infty)$, α
8   V_∞, T_∞, ρ_∞, $(\alpha + \Delta\alpha)$
9   V_∞, T_∞, ρ_∞, $(\alpha - \Delta\alpha)$
34 $(V_\infty + \Delta V_\infty)$, $(T_\infty + \Delta T_\infty)$, $(\rho_\infty + \Delta\rho_\infty)$, α

34

2

3

6

4,1,8,9

5

7

0   10   20   30   40   50   60   70   80   90   100   120   130   140   150

TIME - SEC

FIG. 2.5-1

2.6   HEAT FLUX MEASUREMENTS ON SATURN S-IV VEHICLE

2.6.1   Evaluation of S-IV Slug-Type Heat Flux Transducer With Air Gap

Several laboratories of the Marshall Space Flight Center (MSFC) expressed considerable concern over the slug type heat flux transducer proposed for use on the base of the SATURN S-IV vehicle. The reason for concern was the unknown error in the slug temperature due to the air gap surrounding the slug. Consequently, MSFC requested Heat Technology Laboratory (HTL) to fabricate, evaluate, and calibrate a prototype of the proposed transducer.   Fig. 2.6-1 shows the proposed transducer as it was fabricated and also as it was mounted in the heat shield of the S-IV vehicle. Calibration was performed using radiation of known intensity supplied by a quartz-lamp bank. The calibration constant, K, in the equation

$$ q = K \left(\frac{\alpha\, T_s}{\alpha\, t} \right)_i \qquad (2.6\text{-}1) $$

was determined from the initial slopes of temperature-time test data. The average value of K was found to be 0.606 BTU/ft^2°F, with a maximum variation of 5%. In an attempt to approximate sensor losses, it was assumed that **these** losses were proportional to the slug temperature rise;

mathematically this is

$$q = K\left(\frac{dT_s}{dt}\right) + \theta(T_s - T_{si}) \qquad (2.6-2)$$

where:

q = Incident heat flux $\qquad$ BTU/ft^{2}sec

K = Calorimeter thermal capacitance constant $\qquad$ BTU/°F-ft^2

$\frac{dTs}{dt}$ = Rate of change of slug temperature $\qquad$ $\frac{°F}{sec.}$

θ = Conduction loss coefficient $\qquad$ Sec^{-1}

(Ts-Tsi) = Slug temperature rise $\qquad$ °F

The loss coefficient, θ, was calculated by substituting test data into the above equation.

In solving for the calibration constant the derivative as well as the temperature must be taken from test data and substituted in the above equation. Since the largest error in data reduction occurs when a slope is graphically determined, the temperature histories were curve fitted and differentiated by a digital computer to minimize errors. It was found that the accuracy of the derivative from the curve fit was always greater than the accuracy of a graphical approximation of the same derivative. The curve fitted results were then used to derive Fig. 2.6-2 by solving equation(2.6-2). Fig. 2.6-2 clearly shows that the loss coefficient for this transducer is not constant; consequently, the loss coefficient cor-

rection technique is unsuitable for this instrument.

Since the loss coefficient method proved to be inadequate for calibration, efforts were directed toward another widely used method for calibrating heat flux transducers. Fig. 2.6-3 is a plot taken from calibration data from which the heat flux may be approximated if the slope and the sensor temperature are known. However, in determining the heat flux at high slug temperature, a large interpolation error is possible. For the lack of any better method of presenting calibration data, the use of these curves is cautiously suggested.

Fig. 2.6-4 emphasizes the poor degree of sensor isolation by analyzing the transducer with (a) no losses, (b) radiation loss only, and (c) conduction and radiation losses. The upper curve (no losses) is the slope in the equation where no conduction or radiation losses are considered. To determine the losses due to radiation the non-linear differential equation

$$\frac{dT_s}{dt} + \frac{\sigma T_s^4}{\rho c_p \delta} = 0 \qquad (2.6-3)$$

where:

c_p	Specific heat	BTU/lb °F
δ	Slug thickness	ft
θ	Loss coefficient	Sec^{-1}
σ	Stefan-Boltzmann Constant	BTU/ft^{2}sec °R^4

was solved to yield

$$\tanh^{-1}\frac{T_s}{\sqrt[4]{q/\sigma}} + \tan^{-1}\frac{T_s}{\sqrt[4]{q/\sigma}} = 2t\sqrt[4]{\frac{q^3\sigma}{\rho c_p \delta}} + C \quad (2.6-4)$$

having the boundary condition T=540 °R at t=0. The center
curve in **Fig.** 2.6-4 (radiation losses only) is a plot of
equation(2.6-3**)**. The experimental data is plotted as the
lower curve. The degree of conduction loss is evident when
comparing the radiation loss curve to the experimental data.

Up to this point, the transducer has been subjected
to a radiant heat flux only. MSFC personnel estimated that
75-80% of the total heat flux would be convective. Since
convective calibrations are generally not feasible, radiant
calibrations must be used and are accepted, provided the
transducer does not depart significantly from one dimen-
sional heat transfer theory.

In the case of an "air-gap" heat flux transducer,
the sides of the slug are exposed to convective heating,
thus making the effective area for heat transfer higher
than with the radiant calibration. To approximate the
increase in effective area exposed to heat transfer in
addition to surface discontinuity effects, two of the
proposed transducers were constructed as identically as
possible but with the "air-gap" of one filled with a teflon
insulator. The difference in temperature histories of the
two transducers upon exposure to a radiant heat source

were negligible indicating that radiation interchange between the guard ring and slug is a second-order effect and conduction losses are nearly identical.

In order to qualitatively simulate convection, the output of two electric heat guns was directed into a mixing chamber and exhausted parallel to a flat plate in which the transducers were mounted as shown in Fig. 2.6-8. The air temperature from this apparatus after a 90-second warm up period was 580-600 °F and the air velocity was estimated to be 20 fps. The air-temperature profile across the opening was measured and found to be equal at the mounting points of the transducers with a temperature increase of 20°F in the center; no attempt was made to measure the velocity profile.

Initial slopes were used to compute convective heating rates to eliminate the effect of the different rates of heat loss from the two sensors. Below is a tabulation of heating rates for four typical runs. The heat flux averages approximately 70% greater for the "air-gap" transducer. Note that changing the position of the transducers effects the "air-gap" design more than the insulated modification possibly due to an irregular velocity profile. The range of calculated film coefficients for the data below is about 0.8×10^{-2} to 1.6×10^{-2} BTU/ft^{2}sec °F.

INITIAL CONVECTIVE HEATING RATE, BTU/ft^{2}sec

Position	Air Gap	Insulated	q_{ag}/q_I
Left	8.58	4.09	2.10
Left	7.35	4.05	1.81
Right	5.22	3.88	1.34
Right	5.65	3.80	1.49

Avg. q_{ag}/q_I = 1.69

Test results dictate the following conclusions:

(1) No satisfactory calibration method was found.

(2) The experimental performance of the transducer differed considerably from the theoretical due mainly to conduction losses.

(3) An average increase in measured heat flux of about 70% was evidently caused by the air-gap.

2.6.2 Calibration of S-IV Slug-Type Heat Flux Transducer

A slug type heat flux transducer S/N 00030, mounted in a 9 inch square piece of heat shield material was calibrated as received at HTL, i.e.: the gap between the slug and ring was filled and the sensor blackened.

The instrument was mounted in the HTL radiant furnace which consists of a bank of 15 quartz-tube tungsten-filament lamps. The effective heating area of the lamp bank was seven-inches square. A pre-calibrated water cooled Gardon Gage (membrane) type transducer was mounted in the furnace floor, with the reference transducer and the instrument to be calibrated mounted on lines of symmetry with respect to the furnace center lines. Since the heat shield material was dark and appeared to be a good absorber of infrared radiation, the entire furnace floor was blackened. This

was done to eliminate heat flux peaks in the furnace due to reflections from the previously all white furnace floor.

The power to the furnace was controlled by a variable auto transformer. The S-I\ transducer was covered with an opaque shutter while the heat flux was continuously monitored by the water cooled transducer. When the desired level of heat flux was obtained, the furnace was run for two minutes to allow for stabilization and then the shutter was removed from over the S-Iv transducer.

The time versus temperature traces are shown in Fig. 2.6-6 and the slope $\left(\frac{dT}{dt}\right)$ versus heat flux is shown in Fig. 2.6-7 . The heat fluxes shown are the best average as recorded during any given run. The actual heat flux maximum deviation was approximately $\pm.3$ BTU/ft^2 during a run. As can be seen from Fig. 2.6-f , run number 3 began at 170°F. This was due to insufficient cooling of the instrument prior to starting the run. The slopes shown in Fig. 26-7 were taken from 150°F and up, with the exception of run 3.

2.6.3 Comparison of Slug-Type and Gardon Gauge Type Heat Flux Transducer In-Flight Measurements on SATURN S-IV Vehicle

Slug-type total heat flux transducers were flown on the base of the S-IV-4 and -5. On S-IV-6 the slug-type transducers were replaced by Gardon Gauge type direct

reading total heat flux transducers manufactured by Hy-Cal
Engineering Company. There was a significant difference
in the characteristics of the heat flux rates measured by
the two types of transducers (Fig. 2.6-8 and -9).

Generally, the heat flux calculated from the slug-
type transducer data is characterized by a peak at about
230 seconds followed by a decrease in heat flux to a value
approaching zero at burn out. In comparison, the Gardon
Gauge type transducers show a more constant heat flux.
There is a small peak approximately corresponding to the
peak shown by the slug transducers but of much less mag-
nitude.

Heat Technology Laboratory is studying the charact-
eristics of the S-IV slug type heat flux transducer to
further evalute the possibility of error in the heat flux
indicated by this instrument.

Speculation as to a source of error is that epoxy
insulation used to plug the air gap may have fallen out
during flight as a result of vibration, rarefied atmosphere,
inadequate curing time, or high temperatures. Previous
tests on the slug transducer have indicated that an open
air gap could cause a significant increase in convective
heating of the slug (See Section 2.6.1).

A mathematical simulation of the slug transducer
has been programmed on the IBM 7090 computer. A 15 degree
wedge of the heat flux transducer was divided into nodes
as shown in Fig. 2.6-10 . An electrical analogy is used to

describe properties of thermal capacitance and conductance. Values describing the nodal configuration and thermal properties are fed into the computer. Boundary conditions of heat flux can be predetermined for use as inputs varying with time. The program then calculates the variation of nodal temperature as a function of time.
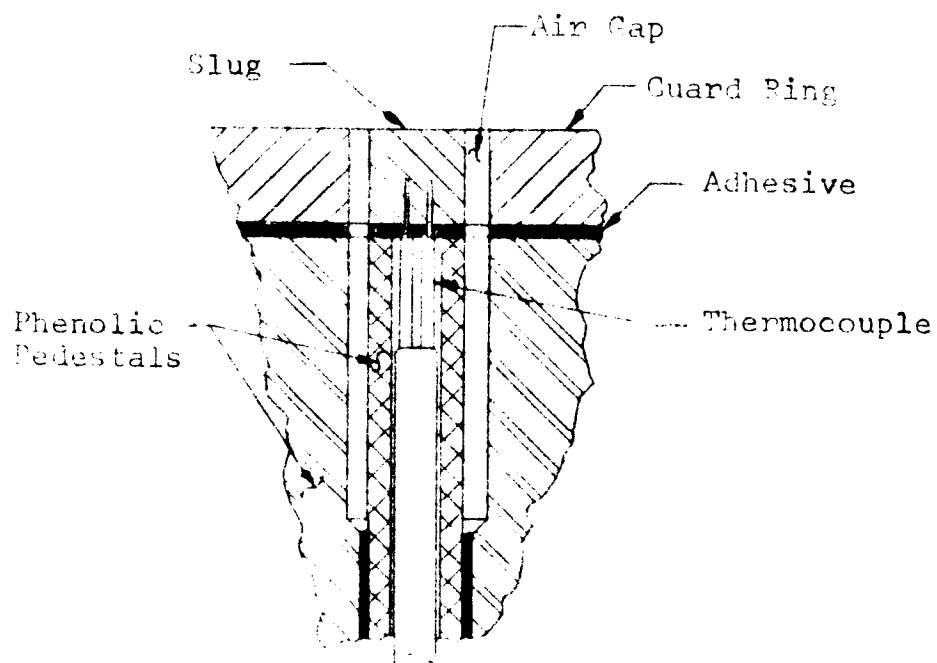
Fig. 2.6-11 shows the time-temperature plots for representative nodes for a constant heat flux of 3 BTU/ft^2-sec on the sensor surface and no conduction losses. This calculation shows a much steeper rate of temperature increase for the calorimeter slug than had been previously determined by experiment (Fig. 2.6-4). This indicates considerable conduction loss and a need for further modification of the mathematical simulation.

Equipment is being assembled to conduct a series of tests on a slug transducer installed in a section of S-IV heat shield material. These tests will include:

1. a. Constant heat flux input tests.

   b. Simulation of heat flux inputs measured in flight.

2. a. Radiative heat flux test

   b. Convective heat flux tests.

3. a. Tests with air gap plugged.

   b. Tests with air gap open.

The constant heat flux tests will indicate the thermal response properties of the transducer and indicate adjustments to be made to the mathematical simulation.

Presumably if there is an error in the heat flux indicated by the slug transducer simulation of this heat flux will cause a detectible variation in test and flight time-temperature plots.

Air Gap

Slug

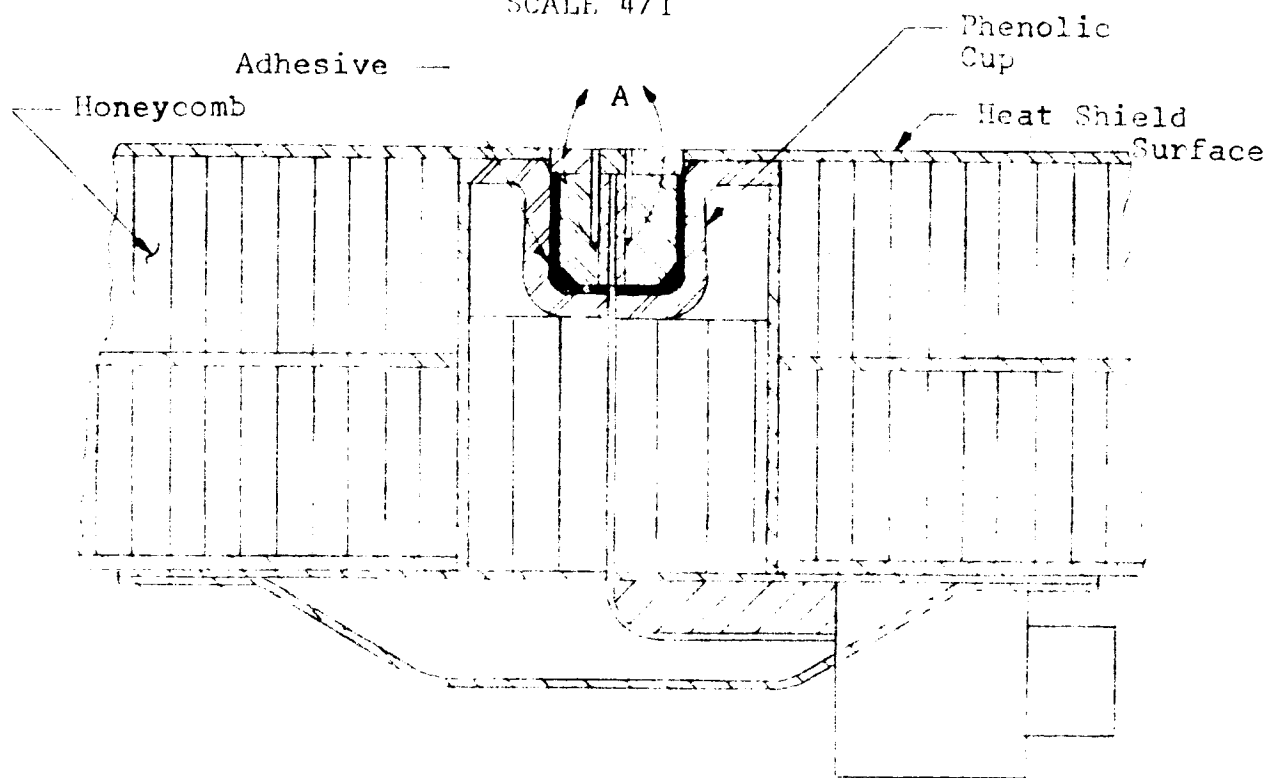Guard Ring

Adhesive

Phenolic
Pedestals

Thermocouple

DETAIL A
SCALE 4/1

Adhesive

Honeycomb

A

Phenolic
Cup

Heat Shield
Surface

FIG. 2.6-1   PROPOSED S-IV SLUG TYPE HEAT FLUX TRANSDUCER
MOUNTED IN HEAT SHIELD

Tslug, °F

$q = 4 \dfrac{BTU}{Ft^2 - Sec}$

$q = 2 \dfrac{BTU}{Ft^2 - Sec}$

Loss Coefficient, Θ, 1/Sec
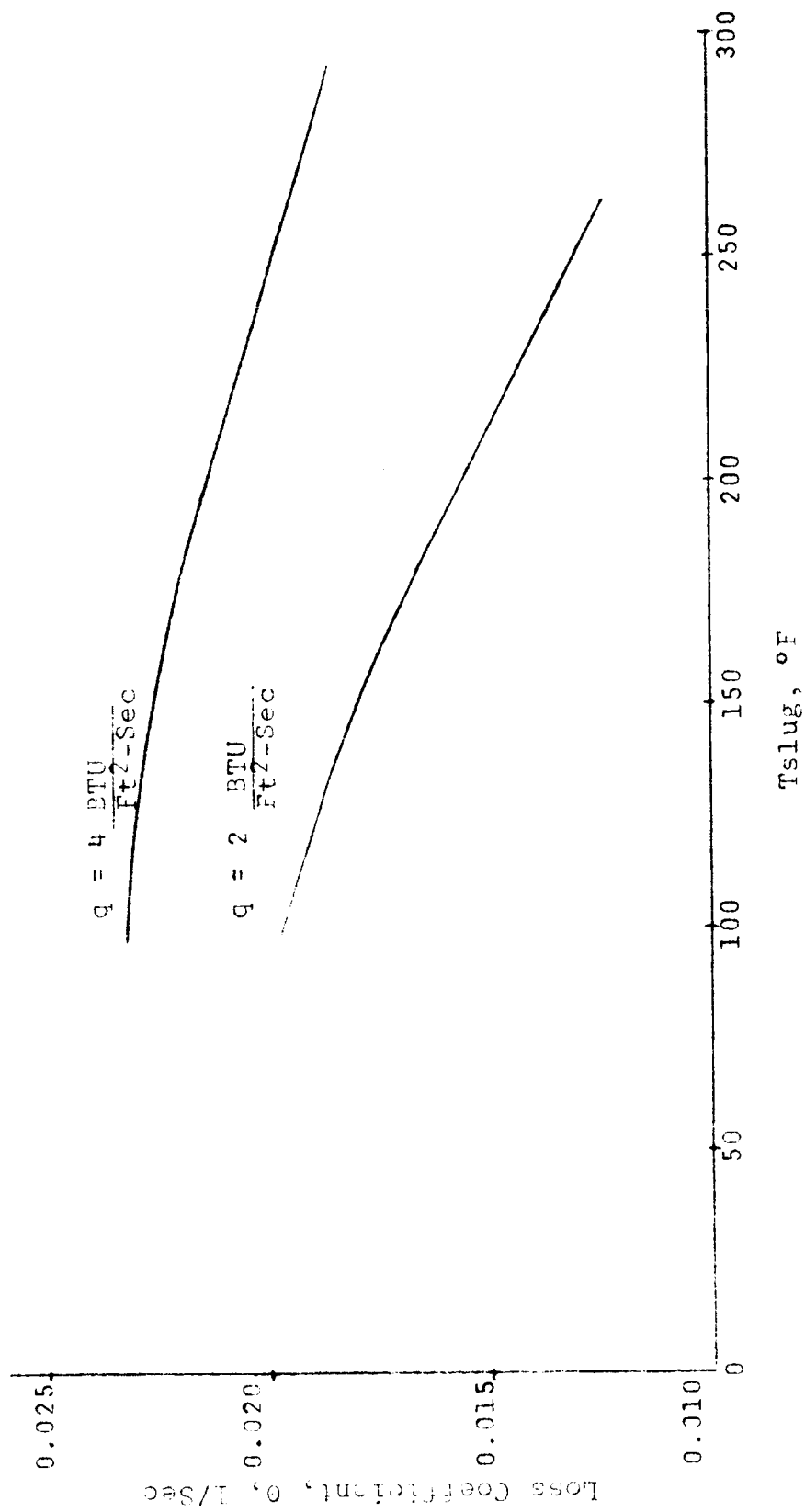
FIG. 2.6-2   LOSS COEFFICIENT, Θ, AS FUNCTION OF SLUG TEMPERATURE
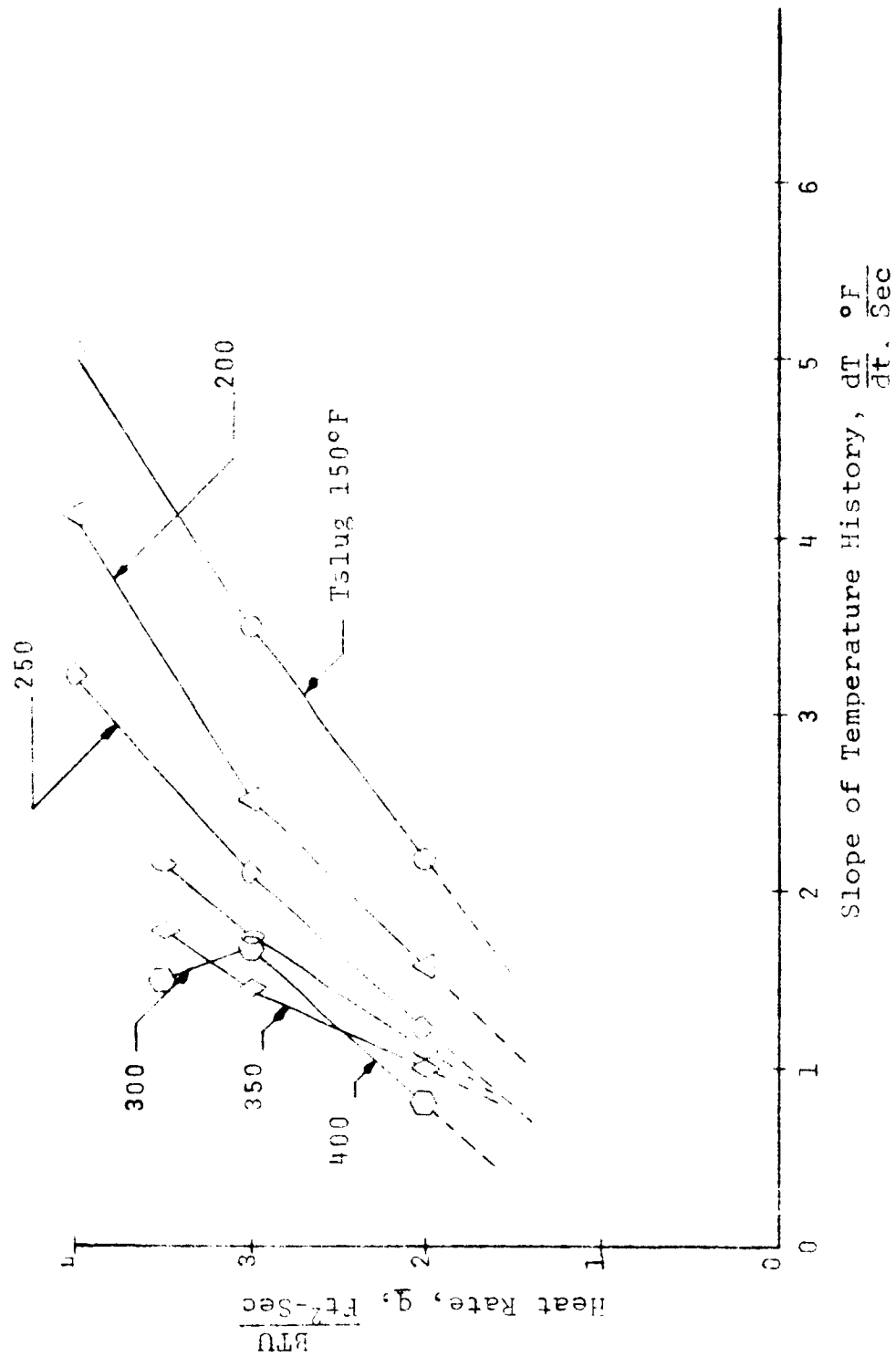
FIG. 2.6-3 S-IV HEAT FLUX TRANSDUCER CALIBRATION DATA

Radiation Losses Only

Experimental

No Losses

Conduction Losses

Radiation Heating Rate, $q_r = 3.0 \dfrac{BTU}{Ft^2\text{-}Sec}$

Time, Seconds
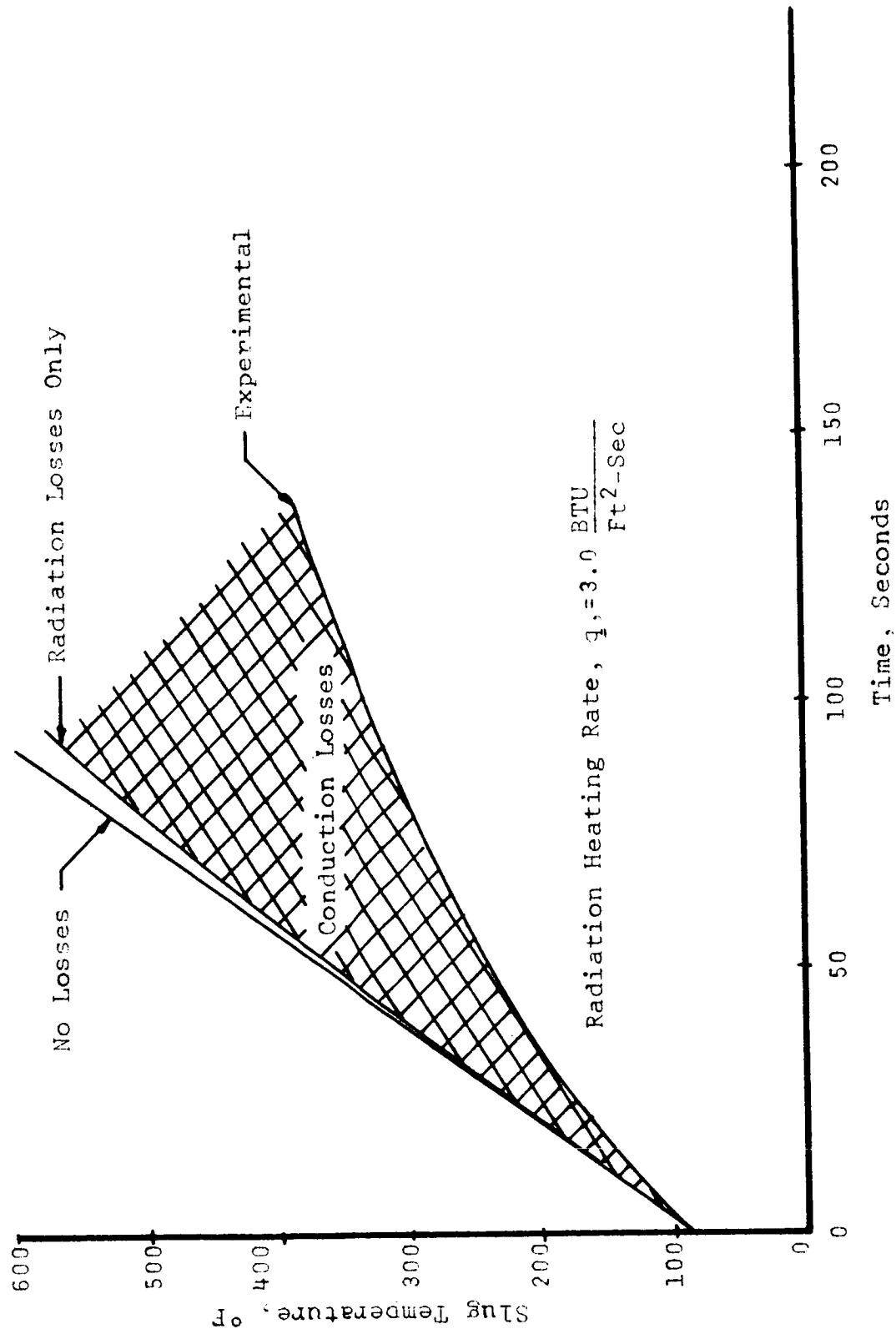
Slug Temperature, °F

FIG. 2.6-4 THEORETICAL AND EXPERIMENTAL SLUG TEMPERATURE HISTORIES

Hot
Air →

Mixing Chamber

Hot
Air ←

Heat Flux Transducers

Top View

NOT TO SCALE

Mixing Chamber

Gas Flow ←

Side View
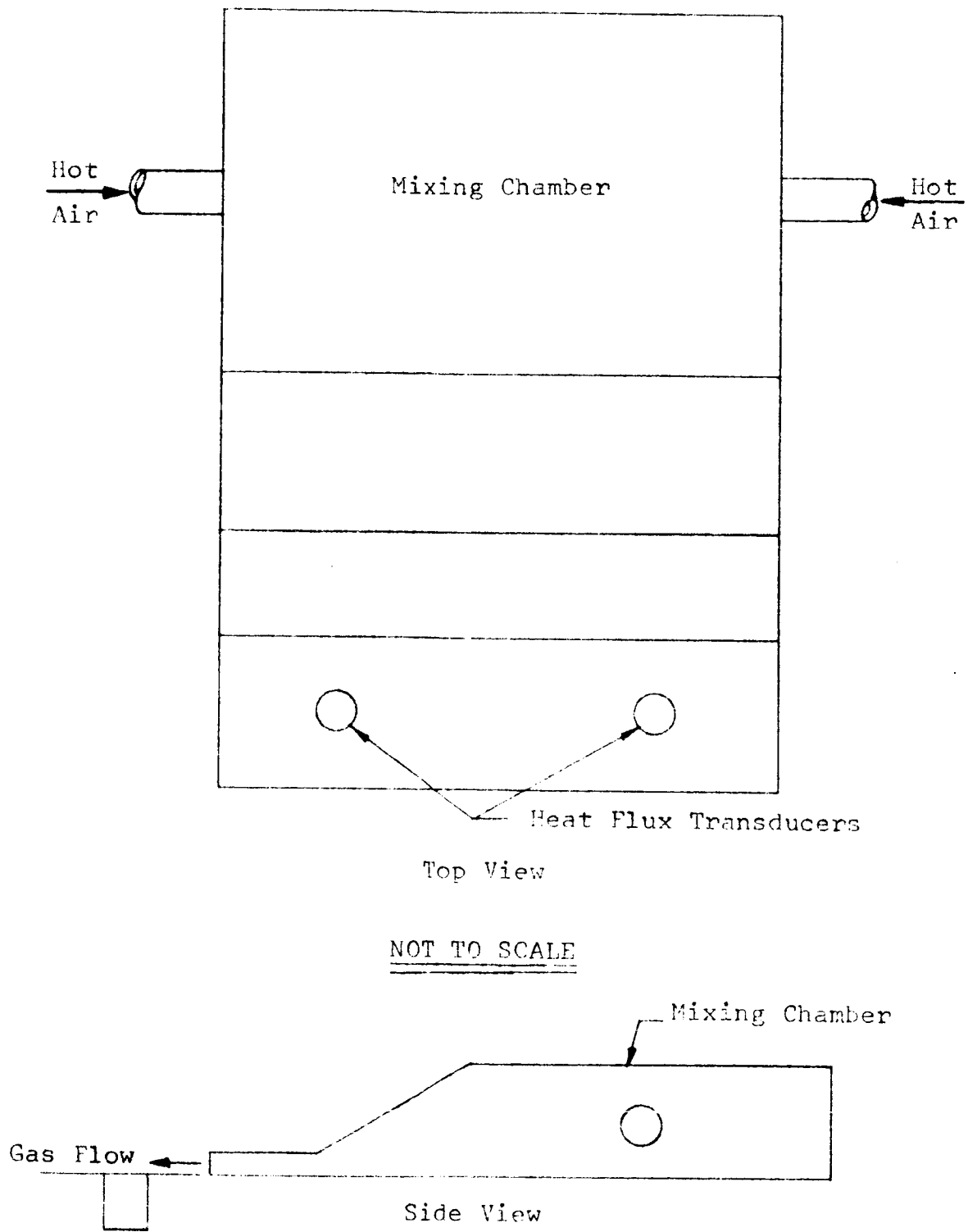
FIG. 2.6-5 CONVECTIVE SIMULATOR

S-IV SLUG HEAT FLUX TRANSDUCER
Calibrated at HTL 2/13-64

#1 Q/A = .75 BTU/Ft2-Sec
#2 Q/A = 1.5 BTU/Ft2-Sec
#3 Q/A = 2.75 BTU/Ft2-Sec
#4 Q/A = 4.0 BTU/Ft2-Sec
#5 Q/A = 5.5 BTU/Ft2-Sec
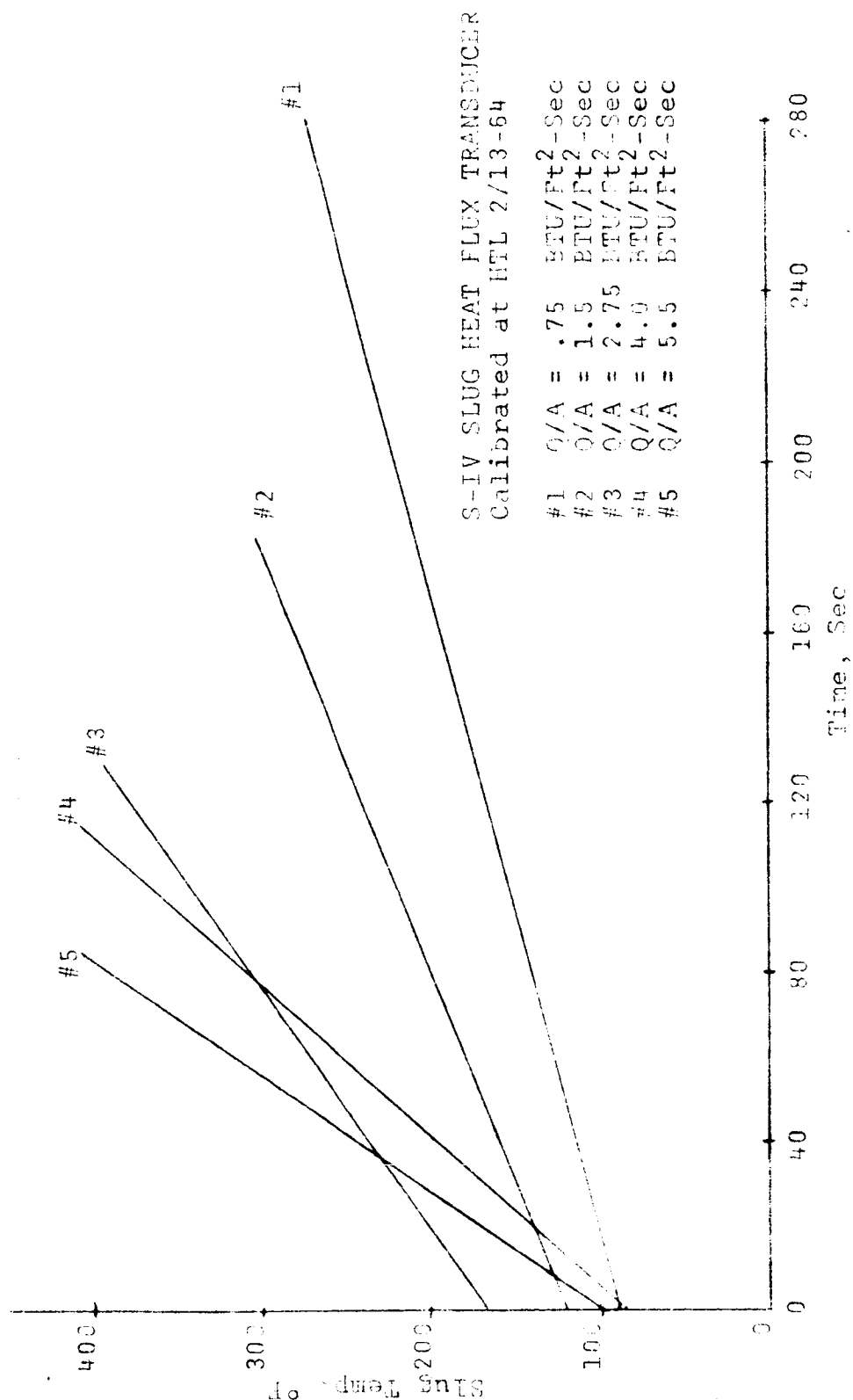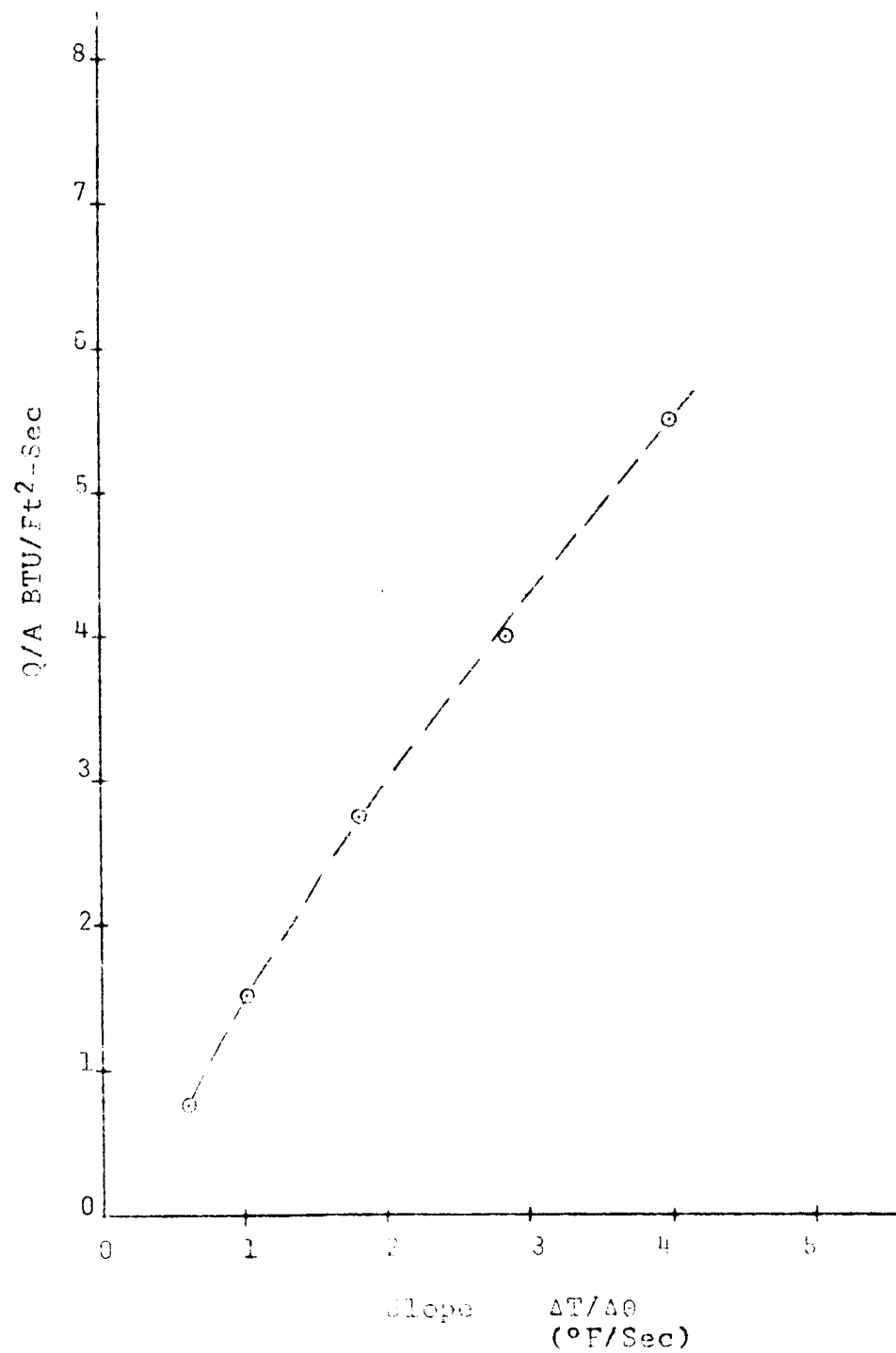
FIG. 2.6-6

FIG. 2.6-7 S-V SLUG HEAT FLUX TRANSDUCER CALIBRATED
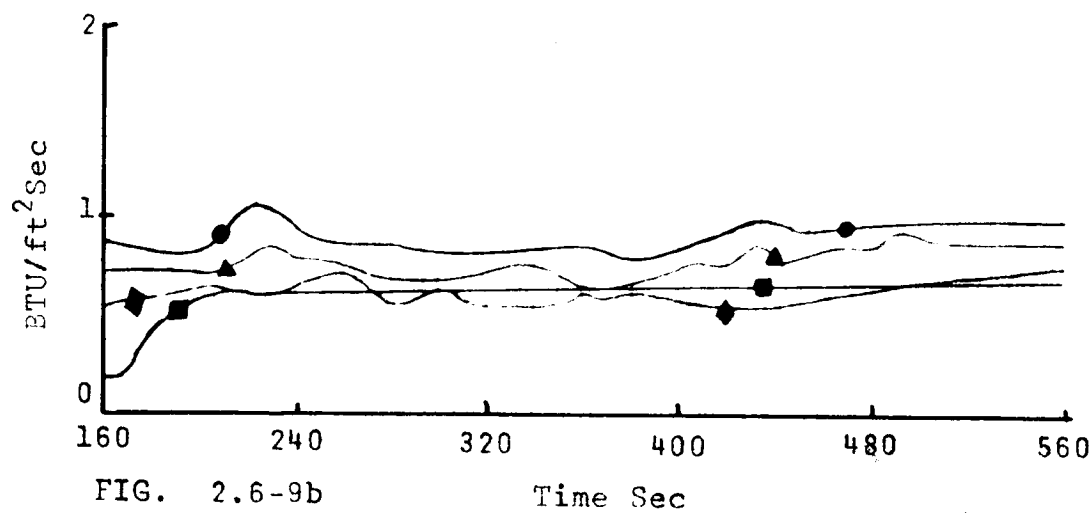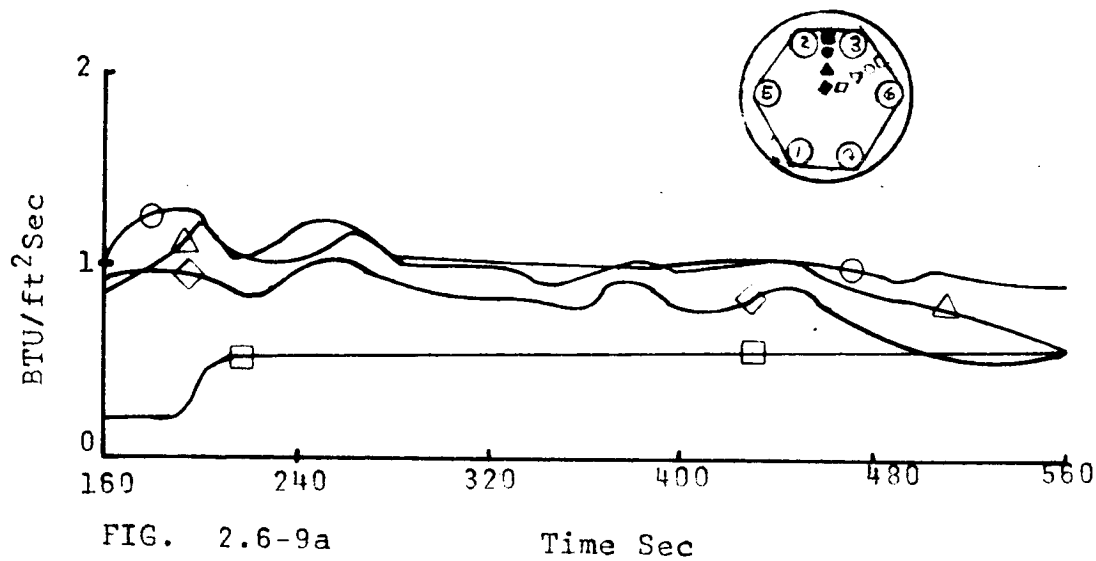AT HTL 2/13/64
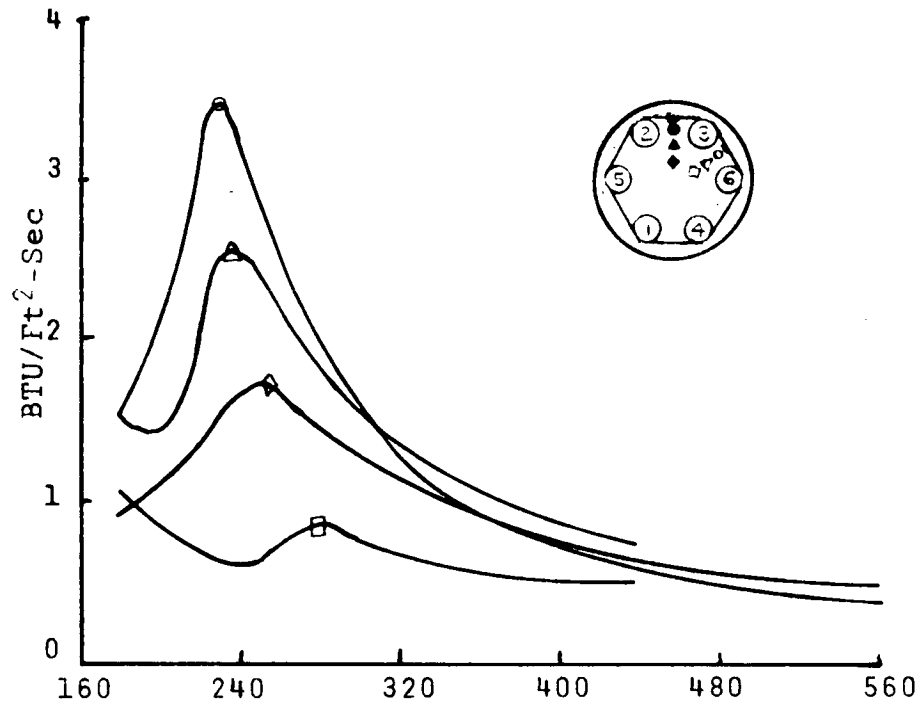
FIG. 2.6-8a   Time Sec
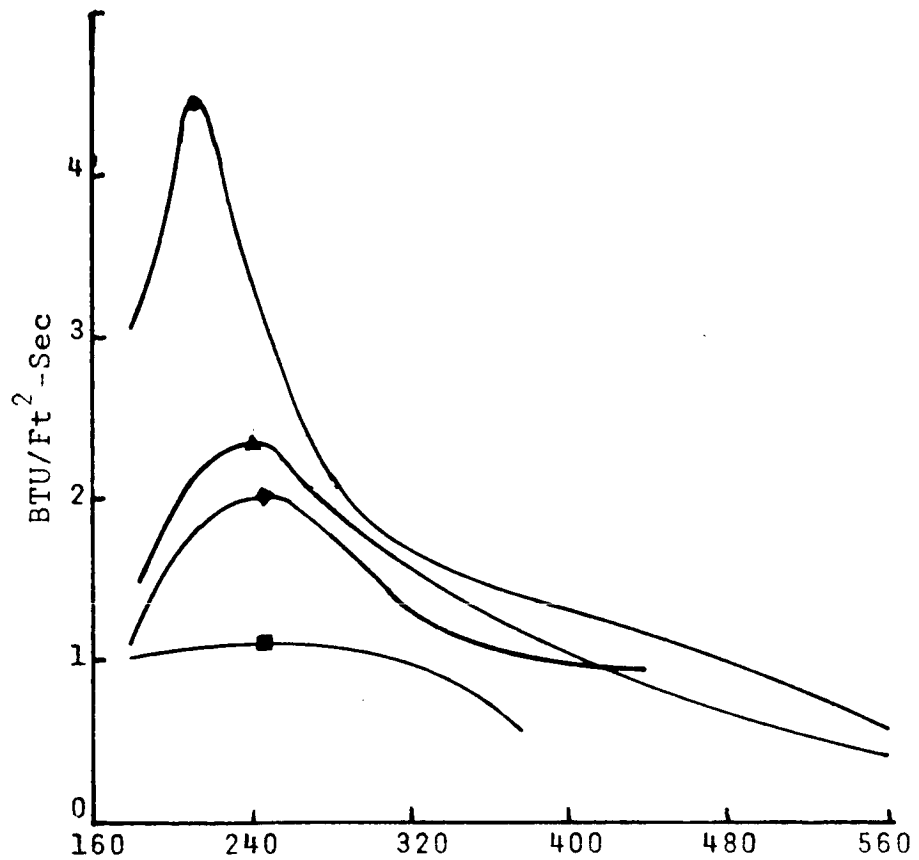
FIG. 2.6-8b   Time Sec

S-IV STAGE BASE HEATING RATES SATURN FLIGHT SA-5
SLUG TYPE HEAT FLUX TRANSDUCER

FIG. 2.6-9a

FIG. 2.6-9b

S-IV STAGE BASE HEATING RATES

SATURN FLIGHT SA-6

GARDON GAUGE TYPE HEAT FLUX TRANSDUCER
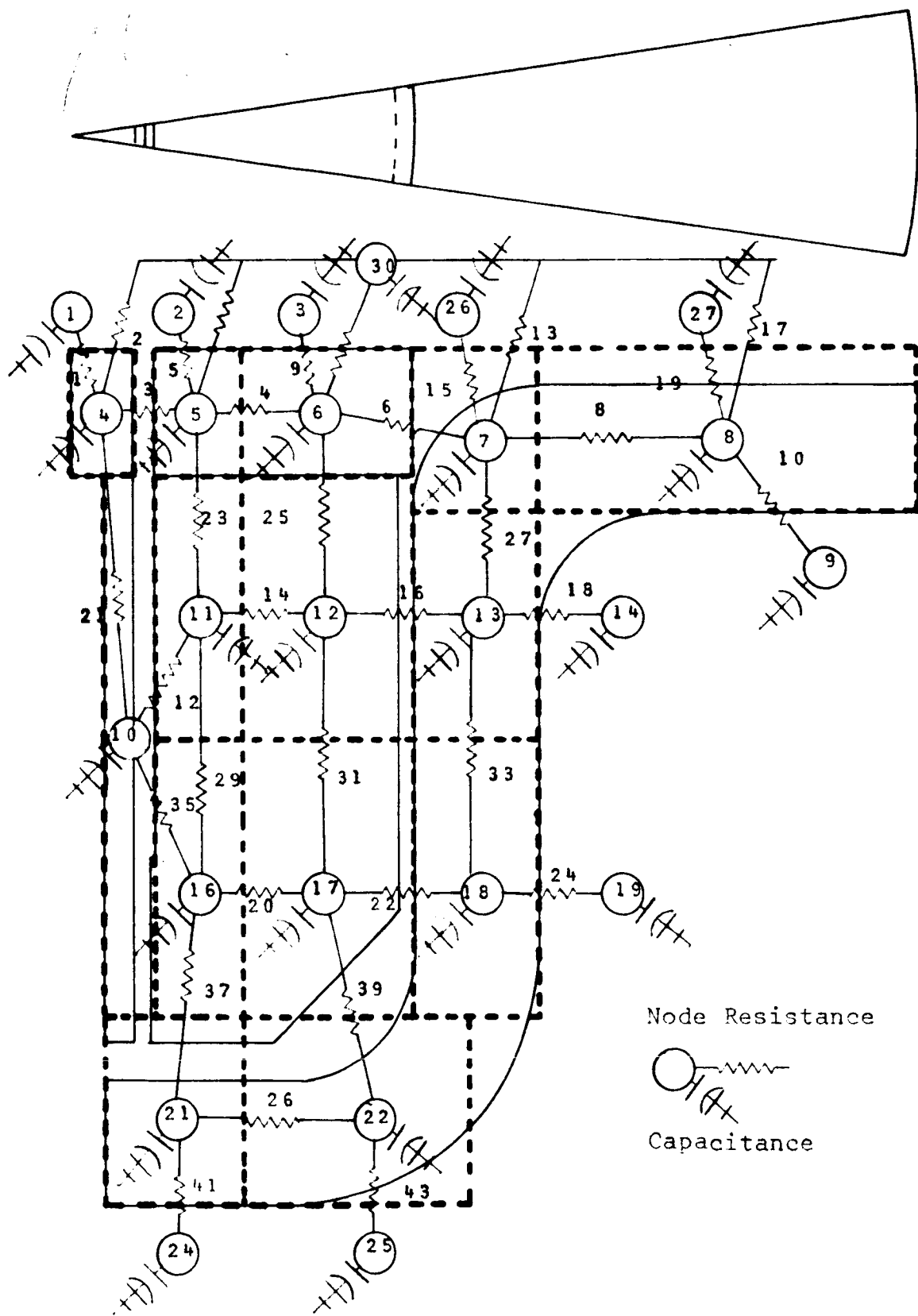
FIG. 2.6-10 NODE SYSTEM AND ELECTRICAL ANALOGY

DOUGLAS CALORIMETER SIMULATION
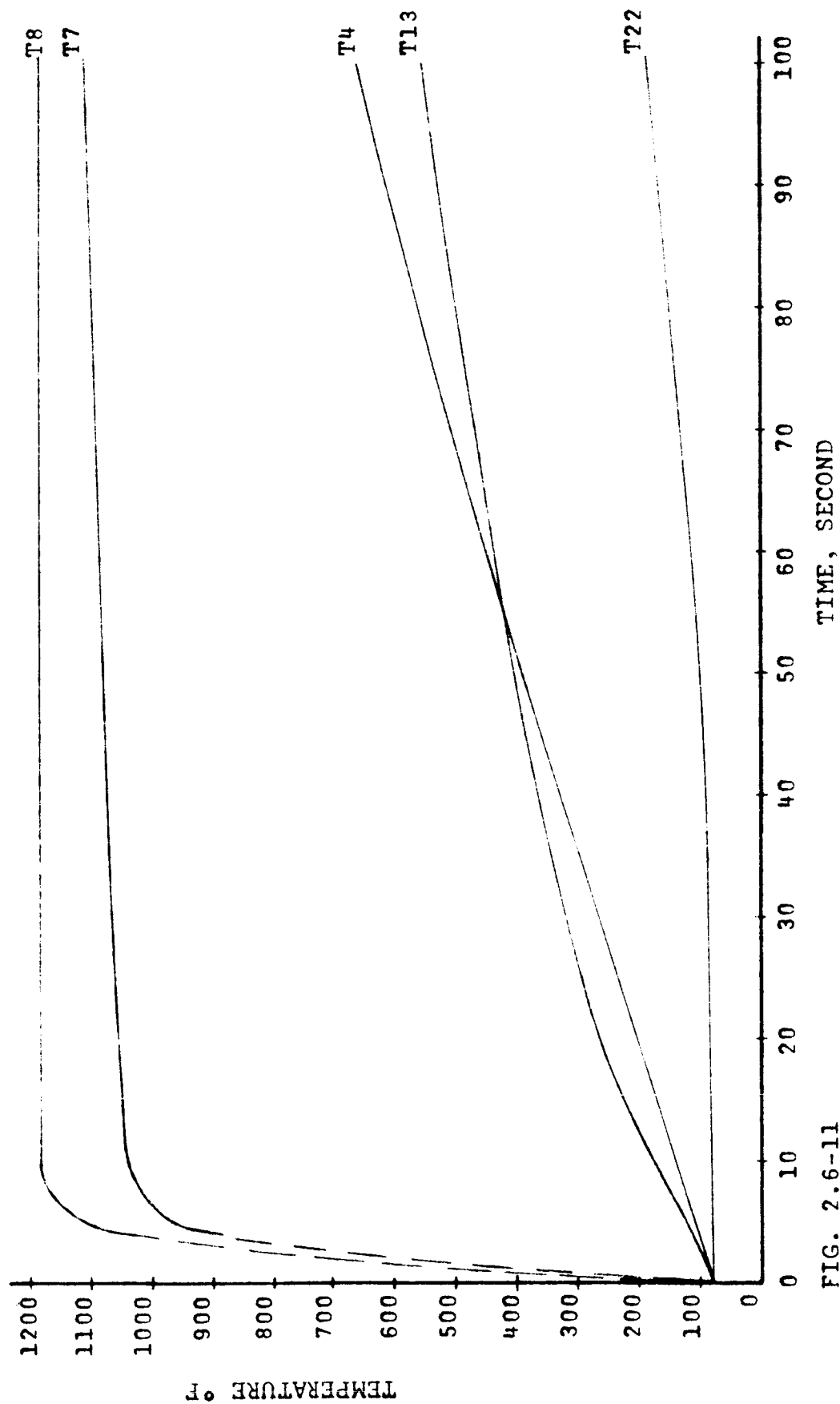3 BTU/ft^2-Sec Input
NODE TEMPERATURES

TEMPERATURE °F

TIME, SECOND

FIG. 2.6-11